Circuit-based Modeling and Inverse Design of Metastructures

by

Luke Jacob Szymanski

A dissertation submitted in partial fulfillment
of the requirements for the degree of
Doctor of Philosophy
(Electrical Engineering)
in the University of Michigan
2022

Doctoral Committee:

Professor Anthony Grbic, Chair
Professor Eric Michielssen
Assistant Professor Bogdan Ioan Popa
Professor Kamal Sarabandi
Assistant Research Scientist Dr. Steve Young

Luke Szymanski

ljszym@umich.edu

ORCID iD: 0000-0002-0408-5537

To my mother and father.

ACKNOWLEDGMENTS

First and foremost, I would like to thank my advisor Prof. Anthony Grbic whose guidance has made this dissertation possible. Tony, I will always be grateful for the opportunity to join your group at the University of Michigan, as well as everything you have taught me about electromagnetics and research. I would also like to thank Dr. Gurkan Gok, who was a great collaborator and mentor during my internship at UTRC.

I would like to acknowledge my committee Prof. Kamal Sarabandi, Prof. Eric Michielssen, Prof. Bogdan Ioan Popa, and Dr. Steve Young for graciously agreeing to serve on my committee and providing valuable feedback that improved my dissertation. Thank you to the professors and research scientists in the RADLAB as well, whose courses and guidance have provided me with the tools to launch my research career. I would like to thank the RADLAB staff who took care of things behind the scenes and enabled me to focus on my research.

I would also like to thank the Grbic research group for being a great set of colleagues and providing valuable feedback along the way. I would especially like to thank Dr. Jordan Budhu who I have enjoyed collaborating with during my final year. Additionally, I would like to thank Zhanni Wu, Cody Scarborough, Faris Alsolamy, Brian Raeker, Frank Salas, Amanda Couch and Nikolaos Chiotellis for their friendship during my tenure at Michigan you all helped Ann Arbor feel more like home. I would also like to thank all the RADLAB students for their friendship and fun conversations that made life in Ann Arbor more entertaining.

Finally, I would like to thank my family whose unconditional love, support and belief in me has allowed me to become the person I am today. Thank you Mom for nurturing a sense of curiosity in me and always being there for me regardless of the mistakes I made. Thank you dad for instilling a strong work ethic in me and helping me get through those difficult teenage years. I would also like to thank my siblings Eric, Jillayne, Chris and Sam for being the best friends I could ever want. Thank you Eric for joining me here at Michigan and Elisha for sacrificing your living room every Saturday to let me hang out with you guys. A special thank you to my wife So Jeong for her support, advice, patience, and love that helped to see me through this process. I cannot wait to join you in Boston and spend the rest of our lives together.

TABLE OF CONTENTS

LIST OF FIGURES

LIST OF TABLES

LIST OF APPENDICES

LIST OF ABBREVIATIONS

PCB printed-circuit board

MIMO multi-input multi-output

KVL Kirchoff's voltage law

KCL Kirchoff's current law

TEM transverse electromagnetic

TE transverse electric

TM transverse magnetic

TL transmission line

TLM transmission line matrix

ABSTRACT

During the past several decades metamaterials and metastructures research has provided a valuable set of tools for designing devices with extreme control over electromagnetic wavefronts. Both metamaterials and metastructures use subwavelength features to control the electromagnetic response, but they require different design methodologies. Metamaterials are composed of subwavelength scatterers with subwavelength spacings that can be characterized using effective material properties. Design methods for metamaterial-based devices typically rely on equivalent material properties that are locally periodic (possess slowly varying subwavelength features) to perform field transformations. Metastructures, on the other hand, share many of the same features as metamaterials, but they do not require the existence of an equivalent effective medium. As such, metastructured devices require design methods that model individual scattering elements and are capable of modeling devices with local aperiodicity and fast variations in subwavelength features. This makes the development of practical and accurate design methods for metastructures a challenging task.

This dissertation presents recent developments in methods for modeling and designing metamaterial devices and metastructures using concepts from microwave network theory. The presented modeling and design approaches build on earlier work in TL, or circuit-based metamaterials, that were used to realize guided-wave negative index metamaterials, hyperbolic metamaterials, and transformation optics designs. In the first part of this work, the range of effective material properties in circuit-based metamaterials is extended to include 2D omega bianisotropic responses. In the second part, an efficient computational inverse design tool is developed that utilizes the large degrees of freedom that metastructures

provide to design multi-input multi-output metastructures. The efficiency of the design procedure is enhanced through the use of a fast forward problem solver and the adjoint variable method. The fast forward problem solver avoids the use of full-wave solutions through the use of reduced-order models and circuit theory. The adjoint variable method enables efficient gradient calculations in the large design variable space that metastructures provide.

The design procedure is then verified experimentally through the realization of a printed-circuit beamformer for a multi-beam antenna system operating at 10 GHz. The multi-beam antenna system produces nine orthogonal radiation patterns that are excited from nine input ports that are impedance match and isolated. Two examples of beamformers are designed. The first design exhibits positive refraction and the second exhibits negative refraction. The measured antenna system fed by the positive refraction beamformer has a minimum return loss of 18.1 dB, a minimum input isolation of 19.2 dB and a radiation efficiency of -2.7 dB at the frequency of operation. The measured antenna system fed by the negative refraction beamformer has a minimum return loss of 11.6 dB, a minimum input isolation of 21.3 dB and a radiation efficiency of -2.8 dB at the frequency of operation.

CHAPTER 1

Introduction

In recent years metamaterials and metastructures have provided engineers and scientists with new tools for designing devices with extreme control over electromagnetic wavefronts, [1–7]. Metamaterials are periodic structures composed of subwavelength scatterers with subwavelength spacings where a one-to-one relationship can be established between the homogenized electromagnetic response and a set of effective material properties, [8]. Metastructures on the other hand share many of the same properties as metamaterials, such as subwavelength features, but they do not require a one-to-one relationship with a set of effective material properties.

In both metamaterial and metastructured devices, their subwavelength features are used to manipulate electromagnetic wave propagation. However, metastructures can be composed of unit cells where there isn't an obvious medium equivalent. This can be advantageous, but it requires different design methodologies that don't rely on equivalent material properties such as transformation optics [9, 10] or gradient-index based designs [11, 12]. One promising alternative is computational inverse design, where optimization routines are paired with forward problem solvers to retrieve the required characteristics of the metastructure to perform field transformations, [13–18].

This thesis presents recent developments in methods for modeling and designing metastructures and metamaterial devices with asymmetric unit cells. The developed metamaterial and metastructure modeling and design approaches build on earlier work in TL, or circuit-based metamaterials, that were used to model negative index media [19], hyperbolic materials [20], anisotropic materials [21, 22], and 1D omega bianisotropic materials [23]. In the first part, the range of effective material properties in circuit-based metamaterials are extended to include 2D omega bianisotropic responses. In the second part, an efficient computational inverse design tool is developed that utilizes all the degrees of freedom that metastructures provide to design MIMO metastructures. The design procedure gains its efficiency through the use of an efficient forward problem solver and the adjoint variable method. The forward problem solver avoids the use of full-wave solutions though the use

of reduced-order models and circuit theory. The forward problem solver is then paired with a gradient-based optimization routine, and due to the large number of design variables that metastructures contain the adjoint variable method is employed to efficiently calculate the gradient.

1.1 Background

1.1.1 Bianisotropic Media

The discussion of reciprocal bianisotropic media in this section is based largely on the presentation of bianisotropic media found in [24]. Throughout this section a harmonic time dependence $e^{j\omega t}$ is assumed and suppressed. The time-harmonic Maxwell equations in point form are,

$$\nabla \times \overline{E} = -j\omega\overline{B} \tag{1.1}$$

$$\nabla \times \overline{H} = j\omega\overline{D} + \overline{J} \tag{1.2}$$

$$\nabla \cdot \overline{D} = \rho \tag{1.3}$$

$$\nabla \cdot \overline{B} = 0 \tag{1.4}$$

Which relate the electric ($\overline{E}$) and magnetic ($\overline{H}$) field intensities at any point in space to the electric ($\overline{D}$) and magnetic ($\overline{B}$) flux densities, current density ($\overline{J}$) and charge density (ρ) at the same point. The electric and magnetic flux densities are also directly related to the field intensities through the constitutive relations, which express how the fields interact with the materials they exist in. The constitutive relations for the most general linear medium can be written as,

$$\overline{D} = \overline{\overline{\varepsilon}} \cdot \overline{E} + \overline{\overline{a}} \cdot \overline{H} \tag{1.5}$$

$$\overline{B} = \overline{\overline{\mu}} \cdot \overline{H} + \overline{\overline{b}} \cdot \overline{E} \tag{1.6}$$

where $\overline{\overline{\varepsilon}}$ is the permittivity, $\overline{\overline{\mu}}$ is the permeability, $\overline{\overline{a}}$ is the magneto-electric coupling, and $\overline{\overline{b}}$ is the electro-magnetic coupling. In materials where $\overline{\overline{a}}$ and $\overline{\overline{b}}$ are both zero the electric flux density depends only on the electric field intensity and the magnetic flux density depends only on the magnetic field intensity. In this scenario, the materials are called isotropic if $\overline{\overline{\varepsilon}} = \varepsilon\overline{\overline{I}}$ and $\overline{\overline{\mu}} = \mu\overline{\overline{I}}$ where $\overline{\overline{I}}$ is the identity operator; otherwise, the medium is referred to as anisotropic. If $\overline{\overline{a}}$ or $\overline{\overline{b}}$ are non-zero then the electric and magnetic flux densities are coupled to both the electric and magnetic field intensities, and in this case the medium is considered

to be bianisotropic.

The bianisotropic constitutive relations (1.6) can represent materials with a wide range electromagnetic responses that are reciprocal or non-reciprocal, passive or active, lossless or lossy. However, the bianisotropic materials discussed in this work are lossless and reciprocal. Enforcing the materials to be reciprocal restricts the material properties to be of the form,

$$\overline{\overline{\varepsilon}} = \overline{\overline{\varepsilon}}^T \tag{1.7}$$

$$\overline{\overline{\mu}} = \overline{\overline{\mu}}^T \tag{1.8}$$

$$\overline{\overline{b}} = -\overline{\overline{a}}^T, \tag{1.9}$$

and $\overline{\overline{a}} = \overline{\overline{b}} = 0$ at zero frequency, so the materials are necessarily dispersive. If the materials are also assumed to be lossless then $\overline{\overline{\varepsilon}}$, $\overline{\overline{\mu}}$ are purely real and $\overline{\overline{a}}$, $\overline{\overline{b}}$ are purely imaginary. This allows for constitutive relations to be re-expressed in terms of a single magneto-electric coefficient that is purely real,

$$\overline{D} = \overline{\overline{\varepsilon}} \cdot \overline{E} + j\overline{\overline{\kappa}} \cdot \overline{H} \tag{1.10}$$

$$\overline{B} = \overline{\overline{\mu}} \cdot \overline{H} - j\overline{\overline{\kappa}}^T \cdot \overline{E} \tag{1.11}$$

This form is useful for exploring the characteristics of the magneto-electric term that lead to different classifications of reciprocal bianisotropic materials. In general, $\overline{\overline{\kappa}}$ can be split into three components,

$$\overline{\overline{\kappa}} = \kappa\overline{\overline{I}} + \overline{\overline{P}} + \overline{\overline{\Omega}} \tag{1.12}$$

where $\overline{\overline{P}}$ is symmetric ($\overline{\overline{P}} = \overline{\overline{P}}^T$) and $\overline{\overline{\Omega}}$ is anti-symmetric ($\overline{\overline{\Omega}} = -\overline{\overline{\Omega}}^T$). Additionally, $\overline{\overline{P}}$ is defined as such that $\mathrm{tr}(\overline{\overline{P}}) = 0$, which means that $\overline{\overline{P}}$ is unitarily equivalent, i.e. equivalent through rotation, to a possibly non-diagonal matrix with all diagonal entries equal to zero. The classification of the different types of reciprocal bianisotropic media based on these coupling terms is shown in Table 1.1.

Of the classifications described in Table 1.1 there has recently been significant interest in two of the material classes: isotropic chiral and omega responses. Isotropic chiral materials have $\kappa \neq 0,\ \overline{\overline{P}} = 0,\ \overline{\overline{\Omega}} = 0$. These materials are referred to as chiral because chiral particles, i.e. particles that lack mirror-symmetry shown in Fig. 1.1a, give rise to a non-zero κ. The non-zero κ in these materials produces a medium that supports elliptically polarized eigenwaves, resulting in a rotation of the polarization state for linearly polarized waves propagating through a chiral medium. Omega materials have $\kappa = 0,\ \overline{\overline{P}} = 0,\ \overline{\overline{\Omega}} \neq 0$ which produces a medium that supports linearly polarized eigenwaves. This means that the

Coupling parameters	Classification
$\kappa \neq 0, \quad \overline{\overline{P}} = 0, \quad \overline{\overline{\Omega}} = 0$	Isotropic Chiral
$\kappa \neq 0, \quad \overline{\overline{P}} \neq 0, \quad \overline{\overline{\Omega}} = 0$	Anisotropic Chiral
$\kappa = 0, \quad \overline{\overline{P}} \neq 0, \quad \overline{\overline{\Omega}} = 0$	Pseudochiral
$\kappa = 0, \quad \overline{\overline{P}} = 0, \quad \overline{\overline{\Omega}} \neq 0$	Omega
$\kappa \neq 0, \quad \overline{\overline{P}} = 0, \quad \overline{\overline{\Omega}} \neq 0$	Chiral Omega
$\kappa = 0, \quad \overline{\overline{P}} \neq 0, \quad \overline{\overline{\Omega}} \neq 0$	Pseudochiral Omega
$\kappa \neq 0, \quad \overline{\overline{P}} \neq 0, \quad \overline{\overline{\Omega}} \neq 0$	General reciprocal bi-anisotropic

Table 1.1: Classification of reciprocal bianisotropic media based on the components of the magneto-electric coupling term shown in (1.12).

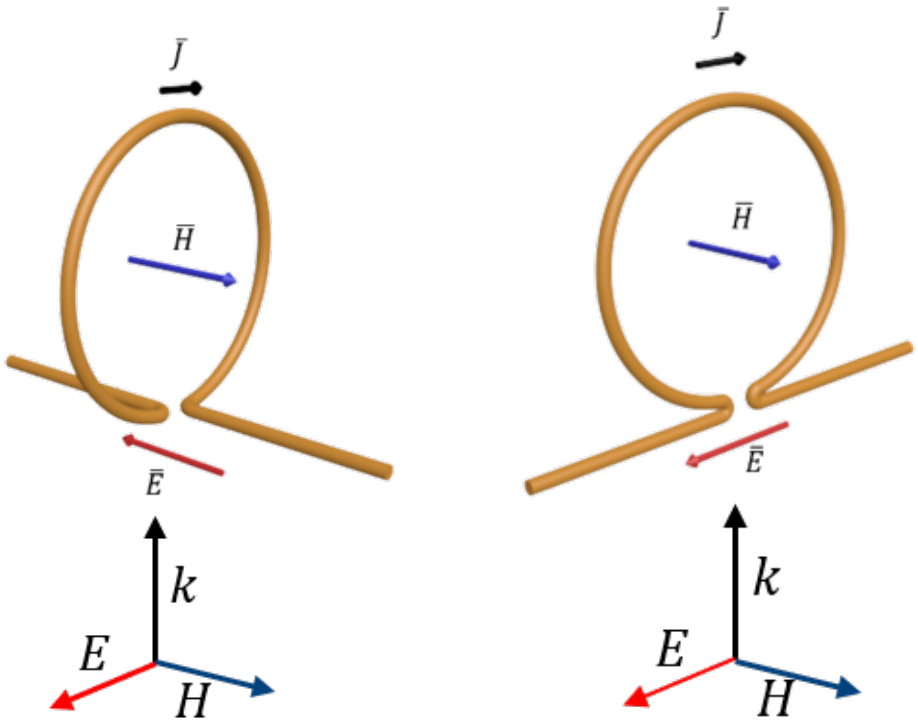

(a) (b)

Figure 1.1: (a) Example of a chiral particle illuminated by a plane wave. The blue arrow indicates the impinging magnetic field and the red arrow indicates the scattered electric field due to the induced current. (b) Example of a omega particle illuminated by a plane wave. The blue arrow indicates the impinging magnetic field and the red arrow indicates the scattered electric field due to the induced current.

polarization state of a linearly polarized wave is conserved in the medium. These materials are referred to as omega since omega shaped particles, i.e. particles that lack directional-symmetry [23, 25–27] shown in Fig. 1.1b, give rise to a non-zero $\overline{\overline{\Omega}}$. The work presented

in this thesis focuses on applications that require conservation of polarization. Therefore, the modeling and synthesis methods found in this thesis focus on structures that exhibit directional asymmetry or omega-type bianisotropic responses.

1.1.2 Circuit-based Modeling of Metamaterials

Since Heaviside introduced the lumped element transmission line model in the late 19th century periodic circuit networks have been used to model electromagnetic wave propagation. The transmission line model represents the transmission line with a periodic network of two-port circuits that have an infinitesimal length. Traditionally, the lumped element unit cells are L-networks with a series inductance and shunt capacitance, shown in Fig. 1.2a. Then by applying Kirchoff's current law (KCL) and Kirchoff's voltage law (KVL) on the unit cell and taking the infinitesimal limit results in the well known Telegrapher's equations,

$$\frac{\partial v(z,t)}{\partial z} = -L' \frac{\partial i(z,t)}{\partial t} \tag{1.13}$$

$$\frac{\partial i(z,t)}{\partial z} = -C' \frac{\partial v(z,t)}{\partial t}. \tag{1.14}$$

Where $v(z,t)$ and $i(z,t)$ represent the voltage and current as a function of position and time within the periodic network, and L' and C' represent per unit length inductance and capacitance, respectively. Assuming time-harmonic fields the wave equations for current and voltage are,

$$\frac{d^2V(z)}{dz^2} - k^2 V(z) = 0 \tag{1.15}$$

$$\frac{d^2I(z)}{dz^2} - k^2 I(z) = 0 \tag{1.16}$$

Which result in the following propagation constant and characteristic impedance for a wave propagating in the periodic network,

$$k = \omega\sqrt{L'C'} \tag{1.17}$$

$$Z_0 = \sqrt{\frac{L'}{C'}}. \tag{1.18}$$

Using field theory, analogous expressions for the Telegrapher's equations, propagation constant, and characteristic impedance can be derived for specific TL geometries that support TEM waves, [28]. In this way a link between wave propagation on a transmission line and

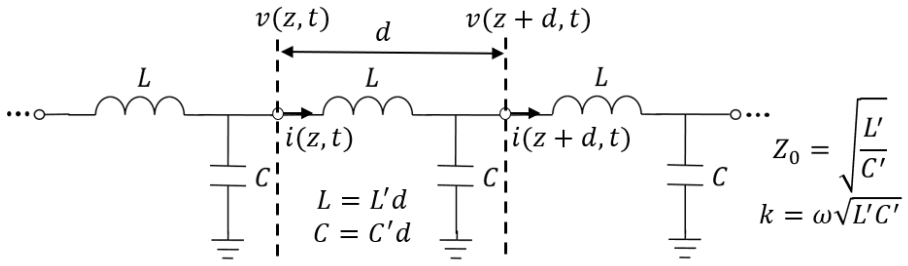

(a)

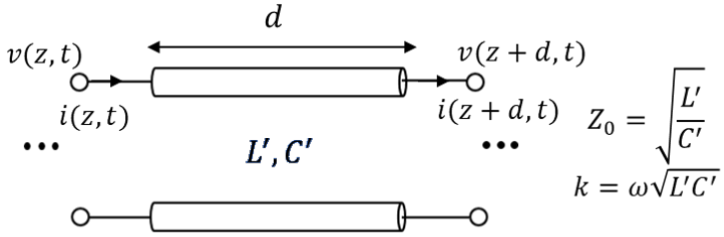

(b)

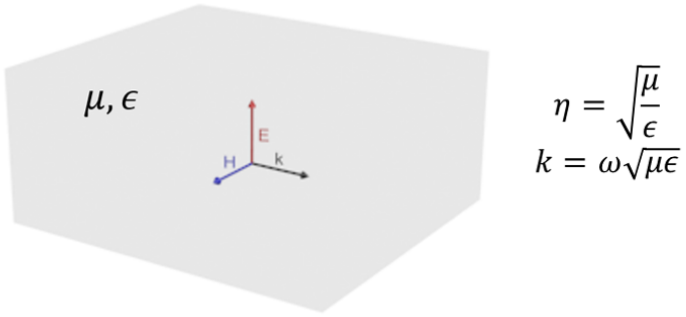

(c)

Figure 1.2: (a) Heaviside's lumped element model of a TL. Where L is the inductance and C is the capacitance of a unit cell, and d represents the length of a single unit cell in the TL model. (b) TL characterized by a per-unit-length inductance (L') and capacitance (C'). (c) A TEM propagating in an isotropic medium characterized by a permittivity ϵ and permeability μ.

propagation in a periodic circuit network is established, see Fig. 1.2b. In a similar manner, a TEM wave propagating in an unbounded medium and a TEM mode on a transmission line can be related to connect unguided waves in continuous media to guided waves on circuit networks. This can be seen by considering an x-polarized TEM wave propagating along the z-direction in an unbounded medium characterized by an isotropic permittivity ϵ

and permeability μ. In this scenario Faraday's and Ampere's laws (1.4) become,

$$\frac{dE_x(z)}{dz} = -j\omega\mu H_y \tag{1.19}$$

$$\frac{dH_y(z)}{dz} = -j\omega\epsilon E_x. \tag{1.20}$$

These can then be solve for the wave equation,

$$\frac{d^2E_x(z)}{dz^2} - k^2E_x(z) = 0 \tag{1.21}$$

$$\frac{d^2H_y(z)}{dz^2} - k^2H_y(z) = 0 \tag{1.22}$$

Which, result in the following propagation constant and wave impedance for the TEM wave,

$$k = \omega\sqrt{\mu\epsilon} \tag{1.23}$$

$$\eta = \sqrt{\frac{\mu}{\epsilon}}. \tag{1.24}$$

By comparing (1.18) and (1.24) a one-to-one relationship can be established to link a wave propagating in a continuous medium to a wave propagating in a transmission line or periodic network. These links provided by the transmission line model inspired artificial transmission lines used in telephonic transmission applications [29]. The model has also been used in numerical electromagnetics forming the basis of the transmission line matrix (TLM) method, [30].

In the early 2000's the introduction of 1-D circuit-based or TL metamaterials renewed interest in circuit analogies of electromagnetic media [19, 31, 32]. This work allowed for the synthesis of a wide range of effective material properties including a negative index using the unit cell shown in Fig. 1.3. This enabled several of the phenomena predicted by Veselago, [33], to be observed [2,31]. Following the introduction of 1-D TL metamaterials, isotropic 2-D TL metamaterials followed [34, 35], allowing for the verification of sub-diffraction imaging using a negative index lens, [5]. Subsequently, it was demonstrated that TL metamaterials can provide anisotropic [36] and tensor material responses, aiding in the realization of a wide range of transformation optics designs [21,22,37]. In [23], 1-D bianisotropic metamaterials with an omega response were introduced using asymmetric 1-D circuit networks. However, a circuit-based equivalent to 2-D bianisotropic metamaterials possessing an omega response had not been developed previously.

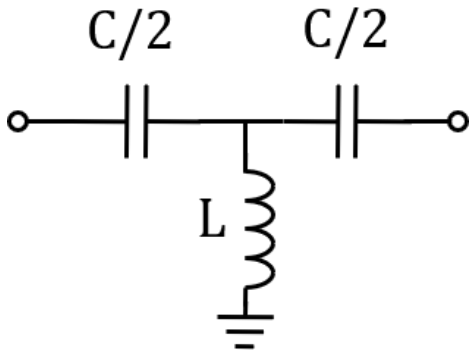

Figure 1.3: Circuit-based unit cell used to model a negative index medium.

1.1.3 Multi-input Multi-output (MIMO) Metastructures

1.1.3.1 MIMO Metastructures and Their Design

Metastructures are often designed to perform a single function such as a polarization transformation [38, 39], refraction [40, 41] or focusing [42–44]. However, there are many applications where it is desirable for a metastructure to be able to perform multiple functions; such as generating multiple phase masks for imaging [4], performing multiple field transformations for antenna beamforming [11, 45–47], or performing mathematical functions [15] or classification tasks [48] for analog computing. Designing metastructures for these applications requires synthesis methods that allow for the multiple functions to be specified and the necessary device characteristics to achieve those functions be determined.

One way that metastructures, capable of performing multiple functions, have been realized is through reconfigurability [49–51]. Reconfigurable metastructures utilize arrays of tunable unit cells that can be tailored to produce different responses. Using tunable unit cells is versatile but also has its drawbacks. They tend to have increased losses, possess finite switching times, and require bias circuitry and control logic. Therefore, for applications that require a finite set of predetermined functions, metastructures composed of static unit cells that are capable of multiple functions, multi-input multi-output (MIMO) metastructures see Fig. 1.4, are an attractive alternative. MIMO metastructures don't require tunability nor control/bias circuitry, and they can be realized using low-loss unit cells. However, efficient methods for designing MIMO metastructures are still needed. One route that is particularly promising for realizing high-performance MIMO metastructures is computational inverse design [11, 13–18, 48, 52–55]. However, there is still significant room for improvements in the development of accelerated forward problem solvers and modeling methods that produce practical devices.

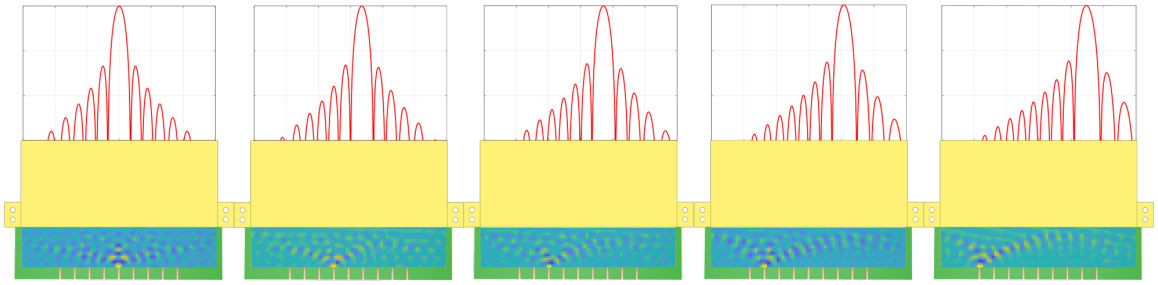

Figure 1.4: Example of a MIMO metastructure can be used to perform multiple field transformations. The metastructure is designed to behave as an antenna beamformer and steers the beam by switching between the input ports.

1.1.3.2 Relationship to MIMO Systems

In high-data throughput communication systems MIMO systems are often used to leverage the carrying capacity, i.e. the degrees of freedom, of a communication channel, [56]. This is often done with spatial multiplexing techniques that allow for multiple signals to exist with in the same space without interfering with each other at the receiver. One way that this can be achieved is by designing antennas that are composed of decoupled elements where the amplitude and phase of each element can be controlled. Then by using signal processing techniques such as, direction of arrival algorithms, the desired and interfering signals can identified and a radiation pattern can be formed that nulls out the interferer and maximizes the received power from the desired signal. Then if there are multiple receivers in the area multiple communication channels can be established in the space allowing for increased data throughput.

MIMO metastructures are similar in that they leverage the large degrees of freedom in metastructures. Leveraging these degrees of freedom allows for the design of metastructures that are capable of multiple field transformations. These types of metastructures could potentially be used in MIMO systems in a manner similar to the antenna discussed above by designing a metastructure that produces orthogonal beams pointed in different directions that are excited using orthogonal (isolated) input field profiles. This results in decoupled radiation patterns that can be used in a manner analogous to the decoupled elements in the previous example of a MIMO system. Using the individual beams produced by the metastructure, directions of arrival could be identified and beam synthesis methods, like the Woodward-Lawson synthesis method, [57], could be used to shape the beam to select a desired signal in a crowded channel.

1.2 Motivation

1.2.1 Omega Bianisotropic Metamaterials

In the design of metamaterial or metasurface devices that operate in transmission, like lenses or antenna beamformers, it is often desirable to maximize the transmitted power and reduce reflections. To achieve zero reflections and maximize the transmitted power the device should impedance match the incident wavefront to the desired transmitted wavefront while also providing the necessary phase transformation to shape the transmitted field. This requires control over the real and imaginary part of input impedance of the metasurface as well as the transmission phase, see Appendix A. This indicates that the device should have a minimum of three degrees of freedom to control the propagation characteristics. Lossless materials with purely electric and magnetic responses only possess two degrees of freedom and support propagating waves with purely real wave impedances and wave numbers. On the other hand, lossless omega bianisotropic media possess complex wave impedances that provide an additional degree of freedom, making them better suited for impedance matching. This property has been exploited in bianisotropic metasurfaces that perform reflectionless field transformations, [6, 7, 39, 58], and wideband impedance matching [59]. These metasurfaces locally conserve the normal power density across their surface, i.e. in a pointwise manner, limiting these metasurfaces to control over transmission phase.

The ability to control the transmission phase enables a wide range of field transformations but many applications require the ability to control that amplitude and phase, such as speckle-free holography [60] or antenna beamforming [11, 45–47]. Precise control over the transmitted amplitude and phase across a metasurface is challenging though because it requires the ability to redistribute power over extremely small distances. However, amplitude control can be achieved using a pair of metasurfaces with an electrically large spacing between them to reshape the power density profile, [60, 61]. The drawback of these designs are that they still require conservation of normal power density across each constitutive metasurface and are electrically large. Another method to achieve discontinuities in normal power density is to convert a propagating wave to a surface wave. This can be achieved with either a reflective metasurface that couples to a surface wave in the same region as the incident wave [62], or a bianiostropic metasurface that locally conserves normal power denisty and couples to a surface wave in the transmitted region [63].

Typically, omega-type metasurfaces like those discussed above are realized with cascaded impedance sheets [39, 64]. Local conservation of normal power density (neglecting transverse coupling) necessitates extremely sub-wavelength spacings between the sheets or metallic walls to isolate neighboring unit cells. However, if transverse coupling is ac-

counted for in the design of metasurfaces, the incident and transmitted power density profiles could be made different. Metasurfaces that utilize transverse coupling could offer greater design freedom and eliminate the need to isolate neighboring unit cells which often leads to designs that are impractical or extremely difficult to manufacture.

In [65], it was established that tangential polarizabilities are sufficient to establish any transmission phase without reflection. However, designs with only tangential polarizabilities can exhibit significantly degraded performance when compared to equivalent realizations utilizing normal polarizabilites. Previously, it was shown that a material with tangential and normal polarizabilities (an inhomogeneous 2-D anisotropic medium) can control phase and power flow to perform field transformations [66]. However, these devices were electrically large because impedance matching and controlling transmission phase is not possible with an anisotropic medium. The complex wave impedance of 2-D omega media could be used to reduce the size of the these devices, providing a route to design electrically thin layers that do not require local conservation of normal power density.

There are two major challenges associated with designing a 2-D omega metamaterial: (a) synthesis of the necessary 2-D omega material parameters and (b) simulating the omega material design. This work aims to address these issues through the development of a circuit-based model for omega media. A circuit model will allow for the materials to be fabricated as 2-D transmission line networks and simulated using commercial circuit solvers.

1.2.2 Inverse Design of MIMO Metastructures

In the early 2000's research in metamaterials, or homogenizable electromagnetic composites with material properties not found in nature, gained interest when Pendry demonstrated the theoretical possibility of a superlens using negative index media [1] and a negative index metamaterial was experimentally realized [67]. This initial work inspired engineers and scientists to pursue alternative methods for synthesizing negative index media to enable the realization of a superlens. Ultimately, resulting in many novel methods for synthesizing metamaterials with arbitrary material properties.

Then in 2006 transformation optics was introduced which demonstrated the full control over electromagnetic waves that metamaterials could provide, [9, 10]. Transformation optics exploits the form invariance of Maxwell's equations to develop mappings between material parameters and coordinate transformations to control electromagnetic wave propagation in a region. However, transformation optics does have some drawbacks. One issue is that it does not provide a meanings limiting the range of material properties necessary

to realize the desired functionality. This often results in highly anisotropic material parameters that can be difficult to manufacture or negative permeabilities and permittivities that are typically dispersive when realized in practice. It also does not provide a way to design MIMO devices or include the possibility of bianisotropic material parameters. Alternative design methods have been proposed to overcome some of these shortcomings that uses computational inverse design, [13, 15, 16, 48, 52].

However, these inverse design methods have their shortcomings. The design methods in [13, 15, 16, 52] rely on full-wave solutions to Maxwell's equations, which can be computationally prohibitive for electrically large devices with complex unit cells. When the unit cells used to realize the pattern structure contain fine features they typically assume local periodicity to characterize them as effective materials [52] or reflectionless phase shifters [48]. Due to spatial dispersion and violations of local periodicity this approach can lead to degraded performance that may require full-wave optimization of the patterned structure to achieve satisfactory performance.

In [48], a method that avoided the use of full-wave solutions during the optimization procedure was provided. There a design method for stacks of metasurfaces with MIMO functionality was introduced. The design method used scalar diffraction theory to propagate fields forward through the stack of metasurfaces and calculate the transmitted fields. However, this method required large spacings between the metasurfaces to validate the paraxial approximation and neglected multiple interactions between the metasurfaces, leading to devices that may be larger than necessary. Chapters 3-4 of this thesis aim to address some of these issues through the use of reduced-order models and a circuit-network solver to solve the forward problem. By solving the forward problem this way, full-wave solutions are avoided during the optimization process but multiple interactions are accounted for between the metastructure's unit cells.

1.3 Thesis Outline

This thesis presents recent developments in methods for modeling and designing metamaterials and metastructures with asymmetric unit cells. The modeling and design approaches described in this thesis build on earlier work in TL, or circuit-based, metamaterials that were used to realize guided-wave metamaterials with a negative index, hyperbolic dispersion relations, and anisotropic material properties for transformation optics designs. Here, similar concepts are used to expand the range of material parameters available in circuit-based metamaterials and enable a computational inverse design procedure for MIMO metastructures.

In the second chapter, a method for modeling 2D omega bianisotropic materials is pursued to aid in the design of compact reflectionless metamaterial devices with amplitude and phase control. Earlier work that utilized omega bianisotropy to perform field transformations neglects transverse coupling between the metasurface's unit cells [6, 62, 63], resulting in devices that lacked the ability to reshape amplitude profiles and were difficult to realize in practice. However, by modeling the device as a metamaterial with transverse coupling practical devices that are compact and possess amplitude and phase control can be realized. Here, an asymmetric unit cell for a 2D periodic circuit network is introduced that is used to extend the achievable range of material properties in 2D circuit-based metamaterials to include omega bianisotropy. The circuit-based metamaterials is then used to design a electrically-thin reflectionless metamaterial slab that controls the normal phase delay and power flow across the slab. Demonstrating that 2D omega bianisotropy can be used to provide impedance matching while controlling the amplitude and phase of a transmitted wavefront.

The third chapter introduces a new design method for metamaterials and metastructures that overcomes some of the limitations and drawbacks associated with transformation optics and other computational inverse design procedures. Transformation optics [9, 10] was the first inverse design method that demonstrated the extent to which metamaterials can be used to control electromagnetic wave propagation. However, the designs produced by transformation optics typically possessed highly anisotropic material parameters as well as negative permeabilities and permittivities that are dispersive when realized in practice. It also does not provide a way to design arbitrary MIMO devices, or include bianisotropic material parameters.

An alternative to transformation optics is to use computational inverse design to retrieve the spatially varying material parameters necessary to produce the desired field transformations. These design procedures have been introduced to address many of the drawbacks of transformation optics, [14–16, 52, 55]. However, these methods often rely on full-wave solutions to Maxwell's equations which can be computationally expensive for electrically-large spatially varying metamaterials and metastructures. As such, they often require an additional step to go from effective material properties to a patterned structure (which often requires additional full-wave optimization) or use very simple unit cells with limited degrees of freedom (resulting in devices that may be larger than necessary). In this chapter these issues are addressed by introducing a circuit-based forward problem solver that enables a computational inverse design procedure for MIMO devices. The forward problem solver uses reduced order models of the patterned structure, which allows for a unit cell with a large number of degrees of freedom to be included and doesn't require an additional

step to pattern the device.

The fourth chapter presents an experimental realization of a multi-beam antenna that uses the computational inverse design procedure developed in the third chapter. The antenna is composed of a 3D printed tapered aperture antenna and a metastructured microstrip beamformer. The beamformer is composed of asymmetric units whose spatially varying characteristics are determined using the computational inverse design procedure in Chapter 3. The multi-beam antenna system is then experimentally characterized and shown to be in good agreement with the predicted performance. Providing verification that the design procedure can be used to realize practical devices with arbitrary control over the amplitude and phase of the output fields for multiple input excitations.

CHAPTER 2

Circuit-based Modeling of 2D Omega Bianisotropic Media

2.1 Introduction

The introduction of 1-D circuit-based or TL metamaterials in the early 2000's created renewed interest in circuit analogies of electromagnetic media [19, 31, 32]. This work allowed for a wide range of effective material properties to be synthesized including a negative index. These negative index TL metamaterials enabled several of the phenomena predicted by Veselago, [33], to be observed [2, 31]. The initial success of 1-D TL metamaterials motivated researchers to develop isotropic 2-D TL metamaterials [34, 35], allowing for the verification of sub-diffraction imaging using a negative index lens, [5]. It was subsequently demonstrated that TL metamaterials can provide anisotropic [36] and tensor material responses, aiding in the realization of a wide range of transformation optics designs [21, 22, 37]. In [23], 1-D bianisotropic metamaterials with an omega response were introduced using asymmetric 1-D circuit networks. However, prior to this work a circuit-based equivalent to 2-D bianisotropic metamaterials possessing an omega response had not been reported.

Lossless bianisotropic media with an omega response (omega media) have complex wave impedances, making them well suited for impedance matching. This property has been exploited in bianisotropic metasurfaces that perform reflectionless field transformations, [6, 7, 39, 58], and wideband impedance matching [59]. These metasurfaces locally conserve the normal power density across their surface, i.e. in a pointwise manner, limiting these metasurfaces to control over transmission phase.

Typically, omega-type metasurfaces are realized with cascaded impedance sheets [39, 64]. An example of how three impedance sheets can be used to design omega-type metasurfaces is in Appendix A where a discussion regarding their quality factor and bandwidth is provided as well. Local conservation of normal power density (neglecting transverse

coupling) necessitates extremely sub-wavelength spacings between the sheets or metallic walls to isolate neighboring unit cells. However, if transverse coupling is accounted for in the design of metasurfaces, the incident and transmitted power density profiles could be made different. Metasurfaces that utilize transverse coupling could offer greater design freedom and eliminate the need to isolate neighboring unit cells.

Previously, it was shown that a material with tangential and normal polarizabilities (an inhomogeneous 2-D anisotropic medium) can control phase and power flow to perform field transformations [66]. However, these devices were electrically large because impedance matching and controlling transmission phase is not possible with an anisotropic medium. The complex wave impedance of 2-D omega media could be used to reduce the size of the these devices, providing a route to design electrically thin layers that do not require local conservation of normal power density.

There are two major challenges associated with designing a 2-D omega metamaterial: (a) synthesis of the necessary 2-D omega material parameters and (b) simulating the omega material design. This work aims to address these issues through the development of a circuit-based model for omega media. A circuit model will allow for the materials to be fabricated as 2-D transmission line networks and simulated using commercial circuit solvers. The circuit model is analyzed as a general 2-D periodic circuit network composed of 1-D asymmetric circuit networks. The dispersion relation and wave impedance are then taken in the homogeneous limit to establish an equivalence with a 2-D reciprocal and lossless omega medium. This circuit equivalent is then used to design a 2-D omega slab that acts as an impedance matching layer. The impedance matching layer provides a desired phase delay and translates the power density profile of the incident wavefront.

2.2 1D Omega Bianisotropic Media

The constitutive relations for a bianisotropic medium are,

$$\overline{D} = \overline{\overline{\varepsilon}} \cdot \overline{E} + \overline{\overline{a}} \cdot \overline{H} \tag{2.1}$$

$$\overline{B} = \overline{\overline{\mu}} \cdot \overline{H} + \overline{\overline{b}} \cdot \overline{E} \tag{2.2}$$

If the medium has an omega response, the magneto-electric dyadics are anti-symmetric: $\overline{\overline{a}} = -\overline{\overline{a}}^T$ and $\overline{\overline{b}} = -\overline{\overline{b}}^T$. Further, if it is lossless $\overline{\overline{\varepsilon}}$ and $\overline{\overline{\mu}}$ are purely real and $\overline{\overline{a}}$ and $\overline{\overline{b}}$ are purely imaginary. Additionally, reciprocity requires $\overline{\overline{\varepsilon}} = \overline{\overline{\varepsilon}}^T$, $\overline{\overline{\mu}} = \overline{\overline{\mu}}^T$, and $\overline{\overline{b}} = -\overline{\overline{a}}^T$.

In [23], the equivalence between TEM propagation along a lossless, reciprocal, omega medium and propagation in a 1-D periodic circuit network was established. The dispersion

relation and wave impedance for a lossless and reciprocal 1-D omega medium are,

$$k^{\pm 2} = \omega^2(\mu\varepsilon + a^2) \tag{2.3}$$

$$\eta^{\pm} = \frac{\omega\mu}{k^{\pm} - \omega a} \tag{2.4}$$

where the permeability, μ, and permittivity, ε, are purely real, the magneto-electric coupling, a, is purely imaginary, and the wavenumber is $k^{\pm} = \pm k^{'} - jk^{''}$. The $\pm$ superscripts are included to differentiate between forward and reverse propagating waves.

Performing Bloch analysis on a periodic network with period d, composed of a lossless and reciprocal electrical network represented by a transmission (ABCD) matrix (see Fig. 2.1), yields the following dispersion relation and Bloch impedance

$$\sin^2 k_B^{\pm} d = -BC + \left(j\frac{D-A}{2}\right)^2 \tag{2.5}$$

$$Z_B^{\pm} = \frac{-jB}{\sin k_B^{\pm} d - j\frac{D-A}{2}} \tag{2.6}$$

where the Bloch wavenumber $k_B^{\pm} = \pm k_B^{'} - jk_B^{''}$, [28]. Since the network is lossless, A and D are purely real while B and C are purely imaginary. Further, reciprocity requires that

$$AD - BC = 1. \tag{2.7}$$

In the homogeneous limit, $|k_B^{\pm} d| \ll 1$, so (2.5) and (2.6) become,

$$(k_B^{\pm} d)^2 = -BC + \left(j\frac{D-A}{2}\right)^2 \tag{2.8}$$

$$Z_B^{\pm} = \frac{-jB}{k_B^{\pm} d - j\frac{D-A}{2}} \tag{2.9}$$

Comparing (2.3) with (2.8), and (2.5) with (2.9), reveals the following equivalency between the asymmetric network ($A \neq D$) and an omega medium,

$$\mu = -j\frac{B}{\omega d}, \quad \varepsilon = -j\frac{C}{\omega d}, \quad a = j\frac{D-A}{2\omega d} \tag{2.10}$$

It should be noted that although these expressions are different from those presented in [23], they are equivalent.

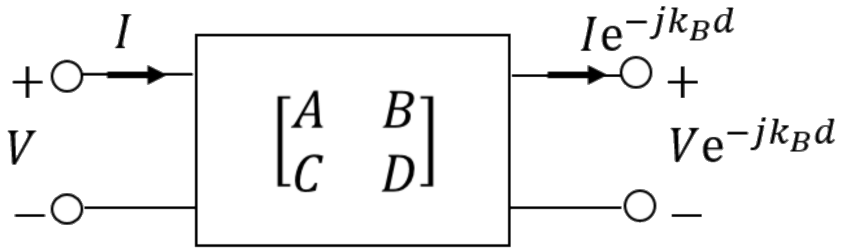

Figure 2.1: Transmission (ABCD) matrix representing a unit cell of a one-dimensional periodic circuit network.

2.3 2D Omega Bianisotropic Media

2.3.1 Field Theory

There are two major classes of reciprocal bianisotropic media: chiral and omega. This work focuses on TE polarized plane waves in a lossless bianisotropic omega-type medium, i.e. a reciprocal bianisotroic medium with an omega response. To maintain a TE polarization it is assumed that the medium preserves polarization. That is, induced magnetic flux densities are along the same axes as the magnetic field and the induced electric flux densities are along the same axes as the electric field. For a TE plane wave propagating in the x-z plane, its wavevector is $\overline{k} = k_x\hat{x} + k_z\hat{z}$, and the relevant fields are, $\overline{E} = E\hat{y}$ and $\overline{H} = H_x\hat{x} + H_z\hat{z}$. The permittivity, $\overline{\overline{\varepsilon}}$, has one relevant entry, ε_{yy}, and the remaining relevant material parameters are,

$$\overline{\overline{\mu}} = \begin{bmatrix} \mu_{xx} & 0 \\ 0 & \mu_{zz} \end{bmatrix} \tag{2.11}$$

$$\overline{\overline{a}} = \overline{\overline{b}} = \begin{bmatrix} 0 & -ja_{xy} & 0 \\ ja_{xy} & 0 & ja_{zy} \\ 0 & -ja_{zy} & 0 \end{bmatrix} \tag{2.12}$$

For an $e^{j\omega t}$ time convention and TE plane wave propagation in the x-z plane, Faraday and Ampere's laws can be written as the following system of equations,

$$-k_z\frac{E_y}{H_x} = \omega(\mu_{xx} - ja_{xy}\frac{E_y}{H_x}) \tag{2.13}$$

$$k_x\frac{E_y}{H_z} = \omega(\mu_{zz} - ja_{zy}\frac{E_y}{H_z}) \tag{2.14}$$

$$k_z \frac{H_x}{E_y} - k_x \frac{H_z}{E_y} = -\omega(\varepsilon_{yy} + j a_{xy} \frac{H_x}{E_y} + j a_{zy} \frac{H_z}{E_y}) \tag{2.15}$$

Solving (2.13)–(2.15), the dispersion relation and wave impedances along the principal axes of the medium can be written,

$$\frac{k_x^{\pm 2} + (\omega a_{zy})^2}{\omega \mu_{zz}} + \frac{k_z^{\pm 2} + (\omega a_{xy})^2}{\omega \mu_{xx}} = \omega \varepsilon_{yy} \tag{2.16}$$

$$\eta_x^{\pm} = \frac{E_y}{H_z} = \frac{\omega \mu_{zz}}{k_x^{\pm} + j\omega a_{zy}} \tag{2.17}$$

$$\eta_z^{\pm} = -\frac{E_y}{H_x} = \frac{\omega \mu_{xx}}{k_z^{\pm} - j\omega a_{xy}} \tag{2.18}$$

where $k_x^{\pm} = \pm k_x^{'} - j k_x^{''}$ and $k_z^{\pm} = \pm k_z^{'} - j k_z^{''}$. The $\pm$ superscripts differentiate between the forward and reverse propagating fields.

2.3.2 Circuit Theory

For comparison with a 2-D omega medium, a 2-D periodic circuit network with the unit cell depicted in Fig. 2.2 will be analyzed. It is composed of four branches of 1-D constituent circuit networks. The two constituent networks along a single direction (x or z) are the same. It is important to note that if the constituent networks are asymmetric the overall unit cell is asymmetric. The propagation characteristics of this network can be determined using the analysis procedure presented in [35]. The dispersion relation and Bloch impedances for the network in Fig. 2.2 are,

$$\frac{\sin^2 \frac{k_{Bx}^{\pm} d}{2} + \left(\frac{A_1 - D_1}{2}\right)^2}{j B_1 \left(\frac{jC_1}{A_1 + D_1} + \frac{jC_2}{A_2 + D_2}\right)(A_1 + D_1)} + \frac{\sin^2 \frac{k_{Bz}^{\pm} d}{2} + \left(\frac{D_2 - A_2}{2}\right)^2}{j B_2 \left(\frac{jC_1}{A_1 + D_1} + \frac{jC_2}{A_2 + D_2}\right)(A_2 + D_2)} = 1 \tag{2.19}$$

$$Z_{Bx}^{\pm} = \frac{-j \frac{2B_1}{A_1 + D_1}}{\tan \frac{k_{Bx}^{\pm} d}{2} + j\left(\frac{A_1 - D_1}{A_1 + D_1}\right)} \tag{2.20}$$

$$Z_{Bz}^{\pm} = \frac{-j \frac{2B_2}{A_2 + D_2}}{\tan \frac{k_{Bz}^{\pm} d}{2} - j\left(\frac{D_2 - A_2}{A_2 + D_2}\right)} \tag{2.21}$$

where, $k_{Bx}^{\pm} = \pm k_{Bx}^{'} - j k_{Bx}^{''}$ and $k_{Bz}^{\pm} = \pm k_{Bz}^{'} - j k_{Bz}^{''}$, and $A_{1,2}$, $B_{1,2}$, $C_{1,2}$, and $D_{1,2}$ satisfy the lossless and reciprocal conditions for an ABCD matrix given by (2.7). Two constraints are imposed on electrical lengths within the circuit network. One constraint is on the electrical lengths of the constituent networks and the second is on the electrical lengths

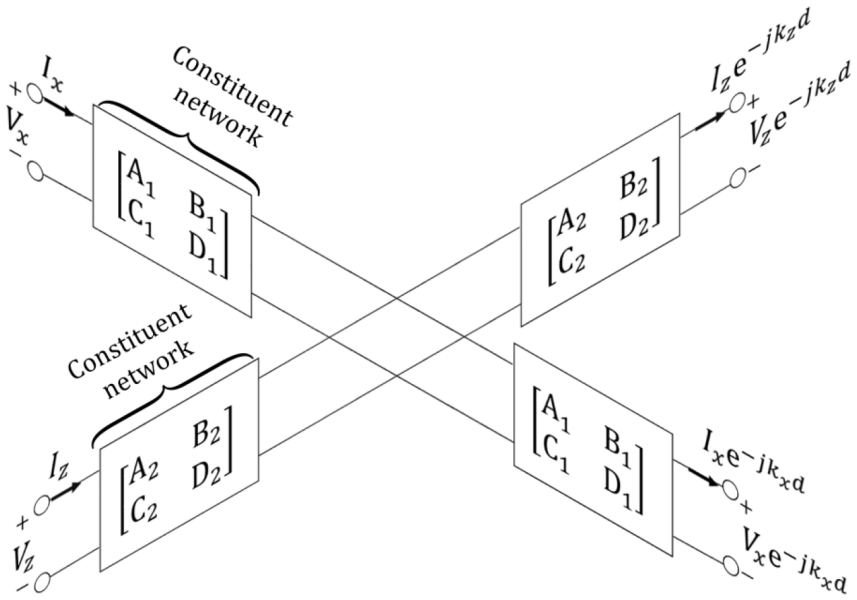

Figure 2.2: ABCD matrix representation of a two-dimensional periodic circuit network with common constituent networks along each axis.

of the overall unit cell, which are not necessarily equivalent conditions. The first constraint reduces spatial dispersion within the unit cell, while the second constraint allows for homogenization of the unit cell. The first constraint can be satisfied by observing from 1-D periodic analysis that the electrical length, $k_{B_{1,2}}\frac{d}{2}$, of each constitutive network is given by $\cos(k_{B_{1,2}}\frac{d}{2}) = (A_{1,2} + D_{1,2})/2$. Therefore, requiring the circuit networks to be electrically small is equivalent to mandating that $A_{1,2} + D_{1,2} \approx 2$, since $\cos(x) \approx 1$ as $x \to 0$. Taking the homogeneous limit, i.e. $(k''_{Bx,z}d, k'_{Bx,z}d \ll 1)$, assuming the constituent networks are electrically small, and $C_1 + C_2 \neq 0$, (2.19)–(2.21) become,

$$\frac{(k^{\pm}_{Bx}d)^2 + \left(A_1 - D_1\right)^2}{j2B_1} + \frac{(k^{\pm}_{Bz}d)^2 + \left(D_2 - A_2\right)^2}{j2B_2} = j2(C_1 + C_2) \tag{2.22}$$

$$Z^{\pm}_{Bx} = \frac{-j2B_1}{k^{\pm}_{Bx}d + j(A_1 - D_1)} \tag{2.23}$$

$$Z^{\pm}_{Bz} = \frac{-j2B_2}{k^{\pm}_{Bz}d - j(D_2 - A_2)} \tag{2.24}$$

Comparing these expressions to those from field theory reveals a one-to-one relationship between (2.16)–(2.18) and (2.22)–(2.24). Therefore, if the 1-D constitutive networks are electrically small, and the unit cell can be homogenized, the 2-D network shown in Fig. 2.2

behaves like an omega medium with material parameters,

$$\mu_{xx} = -j\frac{2B_2}{\omega d},\ \ \mu_{zz} = -j\frac{2B_1}{\omega d},\ \ \varepsilon_{yy} = -j\frac{2(C_1+C_2)}{\omega d}$$
$$a_{xy} = \frac{D_2 - A_2}{\omega d},\ \ a_{zy} = \frac{A_1 - D_1}{\omega d} \tag{2.25}$$

For a simpler comparison between the 1-D and 2-D effective material parameters, consider the situation where the ABCD parameters in all of the constitutive networks are halved, then (2.25) becomes,

$$\mu_{xx} = -j\frac{B_2}{\omega d},\ \ \mu_{zz} = -j\frac{B_1}{\omega d},\ \ \varepsilon_{yy} = -j\frac{(C_1+C_2)}{\omega d}$$
$$a_{xy} = \frac{D_2 - A_2}{2\omega d},\ \ a_{zy} = \frac{A_1 - D_1}{2\omega d} \tag{2.26}$$

Comparing (2.26) to (2.10) reveals that the relationship between a 1-D circuit network's ABCD-parameters and its effective material parameters is the same as a 2-D network's with the exception of the permittivity. The effective permittivity is the sum of the permittivities of the constituent networks, as previously observed in isotropic TL grids [19].

A notable feature of both (2.10) and (2.25) is that the magneto-electric response is proportional to the difference between A and D. Therefore, if there is no asymmetry in the constituent networks the magneto-electric response disappears. This is consistent with the fact that asymmetry gives rise to magneto-electric effects in omega-type bianisotropic media, [23, 27].

2.4 Asymmetry in 2-D Periodic Circuit Networks

As previously noted, bianisotropic responses arise in periodic circuit networks if their unit cells are asymmetric. In this section, different types of asymmetries and their effects on the general 2-D unit cell composed of four constituent networks, shown in Fig. 2.3, will be studied. The unit cell is asymmetric in the x-direction if: (a) $B_1 \neq B_3$ or (b) $D_1 \neq A_3$. Due to reciprocity, the condition $C_1 \neq C_3$ is not a sufficient condition to make the unit cell asymmetric if neither (a) or (b) is satisfied. Similar conditions hold for the z-direction. To gain understanding on the effects of these asymmetries, the periodic network's dispersion relation and Bloch impedances will be studied for different conditions placed on the networks ABCD parameters. The dispersion relation and Bloch impedances for the

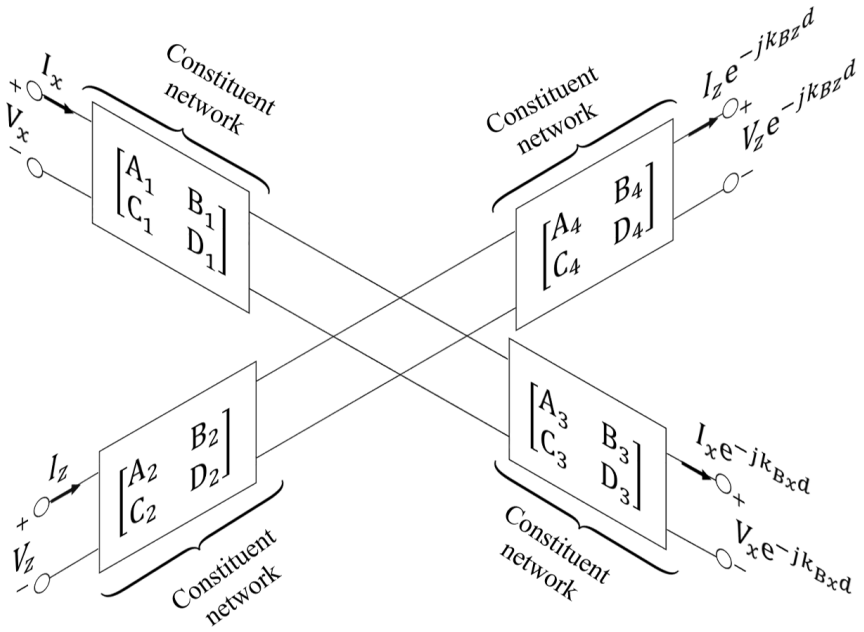

Figure 2.3: ABCD matrix representation of a generalized two-dimensional periodic circuit network where all constituent networks are different.

network shown in Fig. 2.3 are,

$$\frac{4\sin^2\frac{k_{Bx}^{\pm}d}{2}+\left(\frac{D_1-A_3}{\sqrt{A_3D_1}}\right)^2}{j(B_1A_3+B_3D_1)}+\frac{4\sin^2\frac{k_{Bz}^{\pm}d}{2}+\left(\frac{A_4-D_2}{\sqrt{A_4D_2}}\right)^2}{j(B_2A_4+B_4D_2)} = j\frac{A_3C_1+D_1C_3}{A_3D_1}+j\frac{A_4C_2+D_2C_4}{A_4D_2} \quad (2.27)$$

$$Z_{Bx}^{\pm}=\frac{-j\left(\Sigma_{B_{13}}+\left(\frac{\Delta_{B_{13}}}{\sqrt{\Sigma_{B_{13}}}}\right)^2\tan^2\frac{k_{Bx}^{\pm}d}{2}\right)\frac{\Sigma_{B_{13}}}{B_3D_1+B_1A_3}}{2\tan\frac{k_{Bx}^{\pm}d}{2}-j\left(\Delta_{13}+\frac{\Delta_{B_{13}}}{\Sigma_{B_{13}}}\Sigma_{13}\tan^2\frac{k_{Bx}^{\pm}d}{2}\right)\frac{\Sigma_{B_{13}}}{B_3D_1+B_1A_3}} \quad (2.28)$$

$$Z_{Bz}^{\pm}=\frac{-j\left(\Sigma_{B_{24}}+\left(\frac{\Delta_{B_{24}}}{\sqrt{\Sigma_{B_{24}}}}\right)^2\tan^2\frac{k_{Bz}^{\pm}d}{2}\right)\frac{\Sigma_{B_{24}}}{B_4D_2+B_2A_4}}{2\tan\frac{k_{Bz}^{\pm}d}{2}-j\left(\Delta_{24}+\frac{\Delta_{B_{24}}}{\Sigma_{B_{24}}}\Sigma_{42}\tan^2\frac{k_{Bz}^{\pm}d}{2}\right)\frac{\Sigma_{B_{24}}}{B_4D_2+B_2A_4}} \quad (2.29)$$

where $\Sigma_{B_{ij}}=B_i+B_j$, $\Delta_{B_{ij}}=B_i-B_j$, $\Delta_{13}=D_1-A_3$, $\Sigma_{13}=D_1+A_3$, $\Delta_{24}=D_2-A_4$, and $\Sigma_{42}=A_4+D_2$. In this generalized form, there is no medium equivalence. However, the effects of the different types of asymmetry can be understood. By comparing (2.17) to (2.28) one notices that the asymmetry introduced by setting $B_1\neq B_3$ requires spatially dispersive material parameters if the wave impedance is to match that of an omega medium. This is due to the fact that terms proportional to $k_{Bx}^{\pm}d$, occur in (2.28) when $B_1\neq B_3$. The same effect occurs in the z-directed wave impedance when $B_2\neq B_4$. To eliminate

such spatial dispersion, the following conditions are imposed on the constituent networks: $B_1 = B_3$ and $B_2 = B_4$. Under these constraints (2.27)–(2.29) become,

$$\frac{4\sin^2\frac{k_{Bx}^{\pm}d}{2} - \left(j\frac{D_1-A_3}{\sqrt{A_3D_1}}\right)^2}{jB_1(A_3+D_1)} + \frac{4\sin^2\frac{k_{Bz}^{\pm}d}{2} - \left(j\frac{A_4-D_2}{\sqrt{A_4D_2}}\right)^2}{jB_2(A_4+D_2)} = j\frac{A_3C_1+D_1C_3}{A_3D_1} + j\frac{A_4C_2+D_2C_4}{A_4D_2} \tag{2.30}$$

$$Z_{Bx}^{\pm} = \frac{-j\frac{4B_1}{A_3+D_1}}{2\tan\frac{k_{Bx}^{\pm}d}{2} - j2\frac{D_1-A_3}{A_3+D_1}} \tag{2.31}$$

$$Z_{Bz}^{\pm} = \frac{-j\frac{4B_2}{A_4+D_2}}{2\tan\frac{k_{Bz}^{\pm}d}{2} - j2\frac{D_2-A_4}{A_4+D_2}} \tag{2.32}$$

If it is further assumed that the constituent networks and the unit cells are electrically small, it can be shown that the unit cell in Fig. 2.2 is required for a one-to-one relationship to exist between (2.16)–(2.18) and (2.30)–(2.32). Therefore, to limit spatial dispersion in the periodic network the asymmetric unit cell in Fig. 2.2 was used rather than that in Fig. 2.3.

2.5 Characterization of a Lumped Element Unit Cell

The equivalency between omega media and the proposed circuit network in Fig. 2.2 is verified by comparing the simulated dispersion characteristics of the circuit network with the analogous medium's. Isofrequency contours (the intersection of a constant frequency plane with the surface described by the dispersion relation) are used to compare the analogous medium, (2.16), and the circuit network at a fixed frequency. In order to simulate the proposed unit cell, Fig. 2.2, a suitable unit cell is chosen such that the asymmetry of the unit cell can be easily tailored. Lumped element T-networks and π-networks are suitable building blocks (see Fig. 2.4), since they provide asymmetric responses whenever $Z_1 \neq Z_2$ or $Y_1 \neq Y_2$. This can be seen by examining the ABCD parameters of the π and T-networks shown in Fig. 2.4,

$$\begin{bmatrix} A_\pi & B_\pi \\ C_\pi & D_\pi \end{bmatrix} = \begin{bmatrix} 1+ZY_2 & Z \\ Y_1+Y_2+ZY_1Y_2 & 1+ZY_1 \end{bmatrix} \tag{2.33}$$

$$\begin{bmatrix} A_T & B_T \\ C_T & D_T \end{bmatrix} = \begin{bmatrix} 1+Z_1Y & Z_1+Z_2+Z_1Z_2Y \\ Y & 1+Z_2Y \end{bmatrix} \tag{2.34}$$

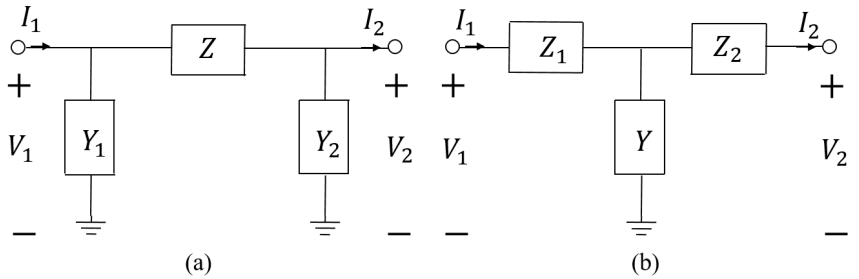

Figure 2.4: (a) A lumped element π-network (b) A lumped element T-network.

Element	Value	Element	Value
L_x	3.53 nH	L_z	2.43 nH
C_{x1}	0.58 fF	C_{z1}	0.94 fF
C_{x2}	3 fF	C_{z2}	2.64 fF

Table 2.1: The inductor and capacitor values necessary to synthesize a medium with the effective material parameters: $\varepsilon_{yy} = 2\varepsilon_0$, $\mu_{xx} = 5\mu_0$, $\mu_{zz} = 7\mu_0$, $a_{xy} = -a_{yx} = j0.1\sqrt{\mu_0\varepsilon_0}$, and $a_{zy} = -a_{yz} = -j0.2\sqrt{\mu_0\varepsilon_0}$ at a frequency of 10 GHz.

In both cases, if $Z_1 \neq Z_2$ or $Y_1 \neq Y_2$ then $A \neq D$ and the network is asymmetric. The π-network will be examined because it results in the simplest overall unit cell. To construct the 2-D network, shown in Fig. 2.2, each constituent network is an asymmetric π-network resulting in the unit cell shown in Fig. 2.5. It can be further simplified by combining all the shunt elements at the central node, as shown in Fig. 2.6.

Since C_1 and C_2 from Fig. 2.2 appear in (2.25) only as a sum they can be set equal without any loss of generality. Additionally, they only appear in the expression for ε_{yy} so, it is equivalent to setting the permittivity of the two constitutive networks equal. Using (2.25) and $C_1 = C_2$, or $Y_{x1} + Y_{x2} + Y_{x1}Y_{x2}Z_x = Y_{z1} + Y_{z2} + Y_{z1}Y_{z2}Z_z$, the equivalent material parameters in terms of the circuit elements are,

$$\begin{gathered}\omega\mu_{xx}d = -2jZ_z,\ \omega\mu_{zz}d = -2jZ_x\ \ \omega\varepsilon_{yy}d = -4j(Y_{x1} + Y_{x2} + Y_{x1}Y_{x2}Z_x), \\ \omega a_{xy}d = Z_z(Y_{z1} - Y_{z2}),\ \ \omega a_{zy}d = Z_x(Y_{x2} - Y_{x1})\end{gathered} \tag{2.35}$$

Generally this unit cell produces a dispersive omega medium. However, by choosing the magneto-electric coupling to satisfy $|a_{xy}| \ll \sqrt{\mu_{xx}\varepsilon_{yy}}$ and $|a_{zy}| \ll \sqrt{\mu_{zz}\varepsilon_{yy}}$, the π-networks are low-pass circuits, thereby reducing the effects of dispersion below the cutoff frequency of the π-network: $\omega_c = 2/\sqrt{L_k(C_{k1} + C_{k2})}$; where, $Z = j\omega L_k$ and $Y_1 = j\omega C_{k1}$ and $Y_2 = j\omega C_{k2}$ in Fig. 2.4 (a). Let's consider a medium with the following material parameters at 10 GHz: $\varepsilon_{yy} = 2\varepsilon_0$, $\mu_{xx} = 5\mu_0$, $\mu_{zz} = 7\mu_0$, $a_{xy} = -a_{yx} = j0.1\sqrt{\mu_0\varepsilon_0}$, and $a_{zy} = -a_{yz} = -j0.2\sqrt{\mu_0\varepsilon_0}$. To satisfy the homogeneous limit assumption, the maximum

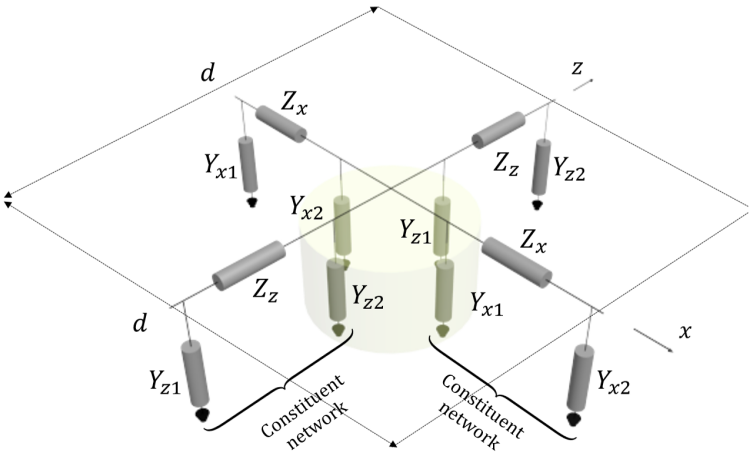

Figure 2.5: A representation of the 2-D lumped element unit cell representing a 2-D omega medium composed of 1-D asymmetric π-networks comprising each constituent network.

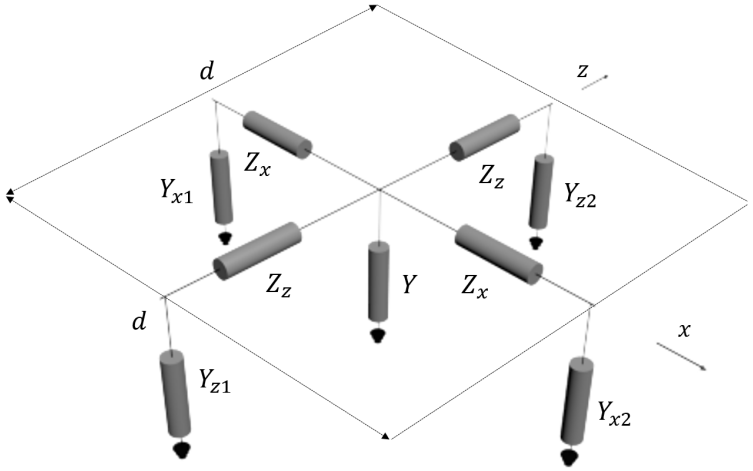

Figure 2.6: A representation of the 2-D unit cell used to implement a 2-D omega medium composed of 1-D asymmetric π-networks in each constituent network. It is constructed by combining the central elements in Fig. 2.5, $Y = Y_{x1} + Y_{x2} + Y_{z1} + Y_{z2}$.

phase delay for on axis propagation is $k_{Bx}d = \pi/5$ rad at $f_0 = 10$ GHz ($d = 0.8$ mm). Using (2.35) the lumped elements of the unit cell in Fig. 2.5 are,

$$\begin{aligned} Z_x &= j\omega_0 L_x = j222\ \Omega, \quad Y_{x1} = j\omega_0 C_{x1} = j36.6\ \mu\text{S}, \quad Y_{x2} = j\omega_0 C_{x2} = j188\ \mu\text{S} \\ Z_z &= j\omega_0 L_z = j159\ \Omega, \quad Y_{z1} = j\omega_0 C_{z1} = j59.3\ \mu\text{S}, \quad Y_{z2} = j\omega_0 C_{z2} = j166\ \mu\text{S} \end{aligned} \tag{2.36}$$

where $\omega_0 = 2\pi f_0$. These impedances and admittances are implemented with the inductors and capacitors in Table 2.1. Substituting (2.36) into (2.35) yields the following effective

material parameters,

$$\begin{aligned}
\mu_{xx} &= 2\frac{L_z}{d} = 5.03\mu_0, \;\; \mu_{zz} = 2\frac{L_x}{d} = 7.02\mu_0, \\
\varepsilon_{yy} &= \frac{4}{d}(C_{x1} + C_{x2} - \omega^2 C_{x1} C_{x2} L_x) = (2.02 - \omega^2(3.5 \times 10^{-24} \;\; s^2))\varepsilon_0, \\
a_{xy} &= -\omega\frac{L_z(C_{z1} - C_{z2})}{d} = \omega(1.61 \times 10^{-12} \;\; s)\sqrt{\mu_0\varepsilon_0}, \\
a_{zy} &= -\omega\frac{L_x(C_{x2} - C_{x1})}{d} = -\omega(3.2 \times 10^{-12} \;\; s)\sqrt{\mu_0\varepsilon_0}
\end{aligned} \tag{2.37}$$

Considering the form of the material parameters in (2.37), the permeability is non-dispersive and the permittivity does not exhibit significant dispersion if,

$$\omega \ll \min\Big(\frac{1}{\sqrt{L_x(C_{x1} + C_{x2})}}, \frac{1}{\sqrt{L_z(C_{z1} + C_{z2})}}\Big) \tag{2.38}$$

due to the low-pass nature of the design. However, the magneto-electric terms exhibit a linear frequency dispersion: $a_{xy} \propto \omega$ and $a_{zy} \propto \omega$. Therefore, even at low frequencies there will be appreciable frequency variation in the magneto-electric terms.

The equivalent material parameters for the unit cell with circuit elements given in Table 2.1 are plotted in Fig. 2.7a, 2.7b over a frequency range from 0 to 15 GHz. The permittivity and permeability show no dispersion over this frequency range, but there is dispersion in the magneto-electric terms, as expected. Due to the relatively small magnitude of the magneto-electric terms, compared to $\sqrt{\mu_{xx}\varepsilon_{yy}}$ and $\sqrt{\mu_{zz}\varepsilon_{yy}}$, the dispersion curves will not diverge significantly from the desired omega materials response below 10 GHz. However, dispersion in the magneto-electric term has significant effects on the imaginary part of the wave impedance. At 9 GHz it has been reduced to 90% of its value at 10 GHz. This will ultimately place bandwidth limitations on devices designed with these structures.

Using Keysight's Advanced Design System (ADS), isofrequency contours were computed for the unit cell at 8, 9, and 10 GHz. The dispersion of the unit cell was characterized by terminating its ports in the appropriate Bloch impedances given by (2.20) and (2.21). The input terminals were driven in the x and z-directions with voltage sources V_x and V_z such that a plane wave was established in the periodic network. The necessary relationship between the voltage sources to produce a plane wave with a given wave vector $k_B = k_{Bx}\hat{x} + k_{Bz}\hat{z}$ in the periodic network is provided in [35]. The simulation was performed by setting V_x to $1V$ and the input terminal in the z-direction was driven with [35],

$$V_z(k_{Bx}d) = \frac{A_1 + D_1}{A_2 + D_2}\frac{\cos(k_{Bz}d/2)}{\cos(k_{Bx}d/2)}e^{j\frac{k_{Bz} - k_{Bx}}{2}d} \tag{2.39}$$

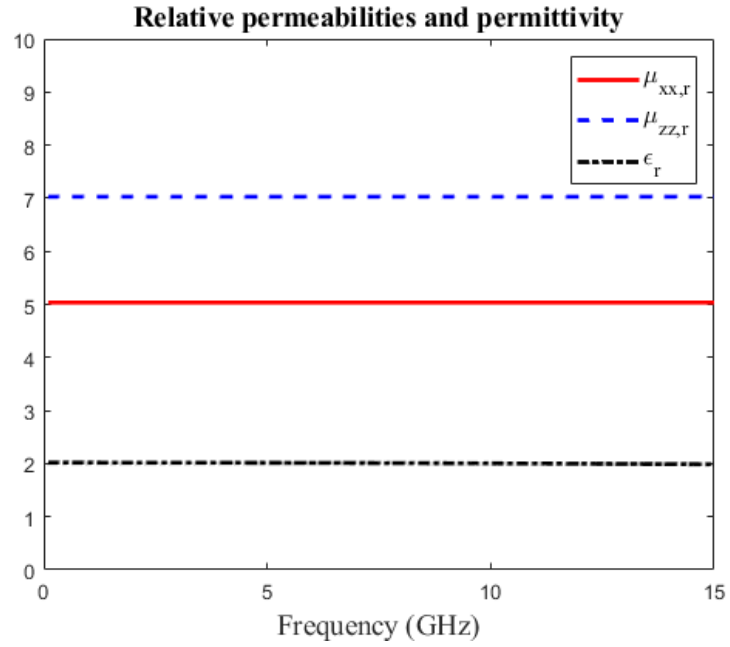

(a)

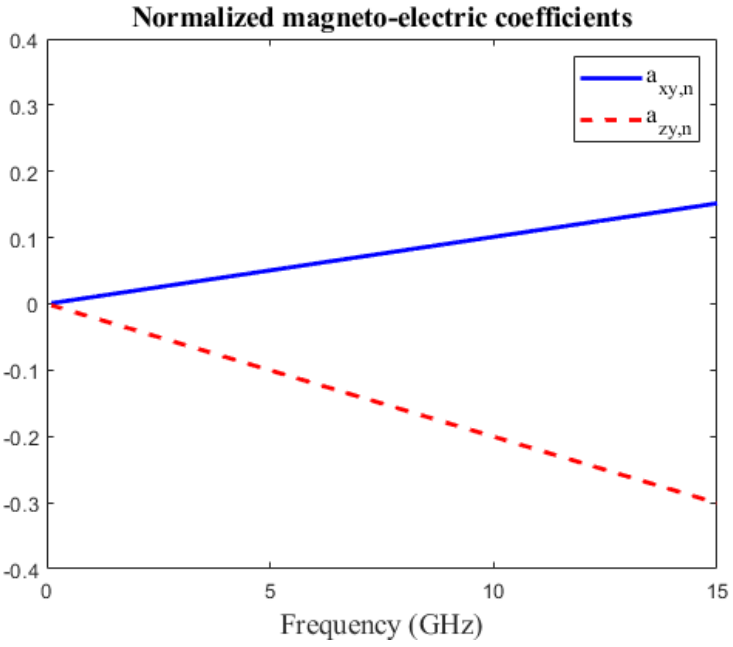

(b)

Figure 2.7: Material parameters of the unit cell shown in Fig. 2.6, composed of the elements given in Table 2.1 up to 15 GHz. (a) Relative permittivity and permeabilities (b) Normalized magneto-electric coefficients, $a_{yz}/\sqrt{\mu_0\varepsilon_0}$ and $a_{yx}/\sqrt{\mu_0\varepsilon_0}$.

The voltage excitation's were defined to provide a desired $k_{Bx}d$ and the resulting $k_{Bz}d$ was retrieved from the simulation. This was done using the full dispersion relationship for the network, (2.19), and expressing $k_{Bz}d$ in terms of the network parameters and $k_{Bx}d$.

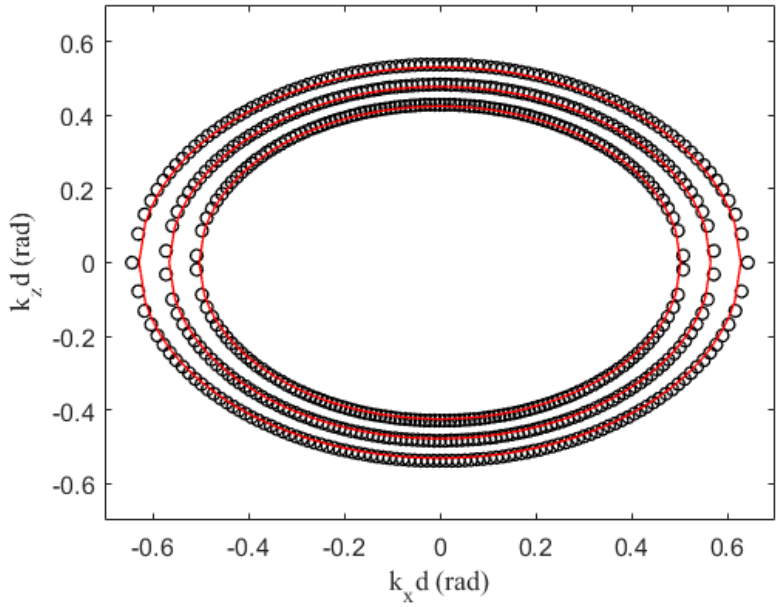

Figure 2.8: Isofrequency contours at 8 GHz (inner), 9 GHz (middle), and 10 GHz (outer) for the unit cell shown in Fig. 2.6 with elements given in Table 2.1. The black circles are the dispersion characteristics extracted from an ADS simulation of the unit cell. The red solid lines are calculated using (2.16) for the equivalent omega medium.

Therefore, (2.39) can be expressed solely in terms of the network parameters and $k_{Bx}d$. To obtain the isofrequency contours $k_{Bx}d$ was swept from $-\pi/5$ to $\pi/5$ rad while measuring $k_{Bz}d$ across the unit cell. The results are shown in Fig. 2.8. There is close agreement between the simulated isofrequency contours and the analogous omega medium's isofrequency contours. Thus, indicating that the propagation characteristics match that of the omega medium within this frequency range.

2.6 Impedance Matched Beamshifting Slab with Phase Control

In [59], a 1-D propagation model was used to impedance match a normally incident plane wave with a Huygens' bianisotropic metasurface separating two regions of dielectric. Further, it was shown that an omega-type response could be used to control the normal phase delay. In this section, a 2-D circuit-based omega medium will be used to design an impedance matching layer that provides a desired normal phase delay but also translates the incident power density profile of a wavefront. The impedance matching condition and desired transmission phase are controlled with the tangential polarizabilities in the layer

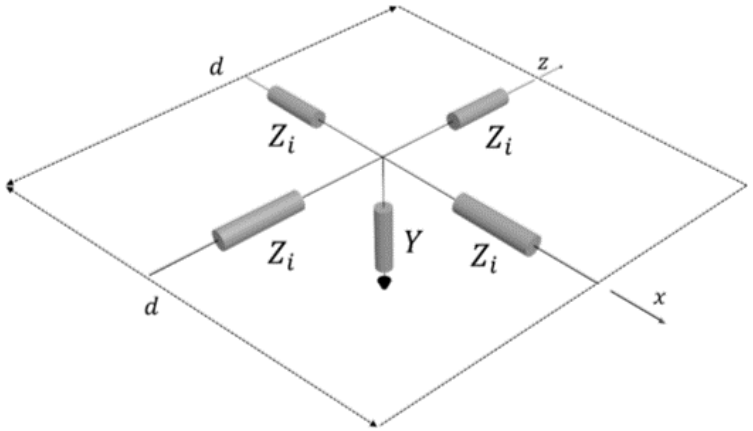

(a)

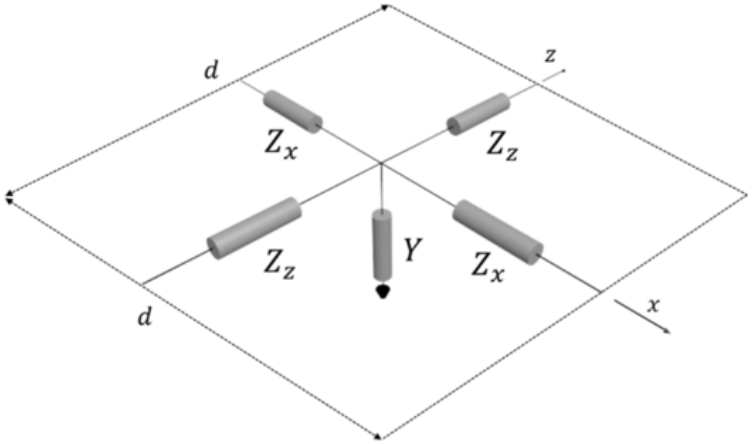

(b)

Figure 2.9: (a) Lumped element unit cell used to implement a 2-D isotropic medium, consisting of two identical symmetric branches along the principal axes (x and z directions). (b) Lumped element unit cell used to implement anisotropic medium, consisting of two different symmetric branches along the principal axes.

and the direction of power flow is controlled by the normal polarizabilites.

To demonstrate this functionality, the circuit simulator ADS is used to simulate two isotropic half spaces of different materials separated by an omega medium slab with thickness d. The slab is infinite in the x-y plane and has finite extent in the z-direction. Therefore, $\hat{z}$ is normal to the slab while $\hat{x}$ and $\hat{y}$ are tangential to the surface of the slab. The simulation domain consists of three regions: medium 1, the omega slab, and medium 2. The two isotropic regions (medium 1 and 2) are implemented using the isotropic lumped element unit cells shown in Fig. 2.9a, and the unit cell shown in Fig. 2.6 was used to realize the omega slab. At the edges of the domain, each region is terminated in appropriate Bloch impedances to emulate an unbounded medium, as shown in Fig. 2.10.

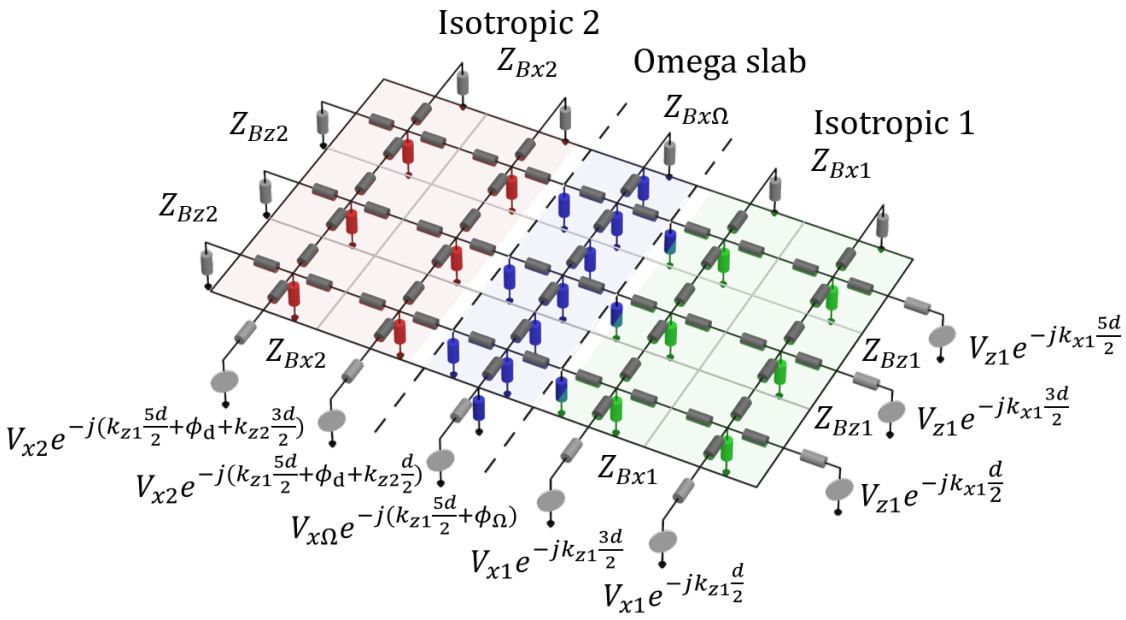

Figure 2.10: A circuit network representation of two different isotropic half spaces separated by a slab of omega medium. The slab acts as a matching layer which provides a desired phased delay ϕ_d in the z-direction. The omega impedance matching layer is shown (in blue) between the two isotropic grids. The boundary of the domain is terminated in the appropriate Bloch impedances to emulate an unbounded structure. The excitation is set by the voltage sources on the boundary. In medium 1 and 2, the amplitudes (V_{x1} and V_{x2}) and phases of the voltage sources are set by the desired incident and transmitted fields. The source connected to the slab provides the amplitude ($V_{x\Omega}$) and phase necessary to emulate the standing wave that exists in the infinite slab.

To design the slab, an omega medium separating two dielectrics illuminated by a TE wave propagating in the x-z plane is analyzed. The slab is designed to impedance match the two regions, provide a transmission phase, ϕ_d, in the $\hat{z}$ (normal) direction and support a prescribed angle of power flow, θ_S. A plane wave is incident from the first medium at an angle, θ_i (relative to the z-axis). The angle of incidence sets the normal wave impedance in medium 1, η_{z1}. Phase-matching sets the tangential wavenumber in the slab, as well as in medium 2. This determines the normal wave impedance in medium 2, η_{z2}. The phase delay ϕ_d determines the necessary normal wavenumber, k_z. The normal wave impedance, η_z, in the omega medium is determined by η_{z1} and η_{z2}. The design equations are calculated using 1-D TL analysis (see Fig. 2.11). By setting the input impedance of the transmission line equal to the incident wave impedance, $Z_{\text{in}} = \eta_1$, and specifying the normal phase delay, ϕ_d, across the transmission line, a system of equations can be written. If $\phi_d \neq n\pi$ for $n \in \mathbb{Z}$ then the system of equations can be solved for the wavenumber and wave impedance of the

omega medium as follows,

$$\tan k_z d = \frac{\sqrt{4\eta_{z1}\eta_{z2}\tan^2\phi_d - (\eta_{z2}-\eta_{z1})^2}}{\eta_{z1}+\eta_{z2}} \tag{2.40}$$

$$\eta_z' = \frac{\sqrt{4\eta_{z1}\eta_{z2}\tan^2\phi_d - (\eta_{z2}-\eta_{z1})^2}}{2\tan\phi_d} \tag{2.41}$$

$$\eta_z'' = \frac{\eta_{z2}-\eta_{z1}}{2\tan\phi_d} \tag{2.42}$$

There exist real solutions to (2.40) and (2.41) if the following inequality is satisfied,

$$|\cos\phi_d| \leq \frac{\sqrt{\eta_{z1}\eta_{z2}}}{(\eta_{z1}+\eta_{z2})/2} \tag{2.43}$$

The time-averaged Poynting vector for a TE plane wave propagating in a lossless, reciprocal omega medium in the x-z plane is given by,

$$\overline{S} = S_x\hat{x} + S_z\hat{z} = \frac{|E_y|^2}{2}\left(\frac{\eta_x}{|\eta_x|^2}\hat{x} + \frac{\eta_z}{|\eta_z|^2}\hat{z}\right) \tag{2.44}$$

The angle of power flow, θ_S, is defined as the angle that the time-averaged Poynting vector makes with the z-axis. This angle θ_S can be expressed in terms of the wave impedances along the principal axes as follows,

$$\tan\theta_S = \frac{\Re(S_x)}{\Re(S_z)} = \frac{\eta_x'}{\eta_z'}\left(\frac{\eta_z'^2 + \eta_z''^2}{\eta_x'^2 + \eta_x''^2}\right) \tag{2.45}$$

where $\eta_i = \eta_i' + j\eta_i''$ for $i = x, z$. From (2.45), it is clear that controlling power flow in the omega medium and impedance matching in the x and z-directions is not possible. Specifying the direction of power flow and impedance matching in the normal direction leaves only one degree of freedom in (2.45). As a result either the real or the imaginary part of the transverse wave impedance, η_x can be matched, while the other is determined by (2.45). Solving (2.16)–(2.18) for the material parameters in terms of k_x, k_z, η_x', η_x'', η_z', and η_z'' yields,

$$\begin{gathered}\varepsilon_{yy} = \frac{1}{\omega}\left(\frac{k_z}{\eta_z'} + \frac{k_x}{\eta_x'}\right),\ \ \mu_{xx} = \frac{k_z}{\omega}\frac{\eta_z'^2 + \eta_z''^2}{\eta_z'},\ \ \mu_{zz} = \frac{k_x}{\omega}\frac{\eta_x'^2 + \eta_x''^2}{\eta_x'}, \\ a_{xy} = \frac{k_z}{\omega}\frac{\eta_z''}{\eta_z'},\ \ a_{zy} = -\frac{k_x}{\omega}\frac{\eta_x''}{\eta_x'}\end{gathered} \tag{2.46}$$

Therefore, an impedance matching omega slab that provides a desired phase delay and

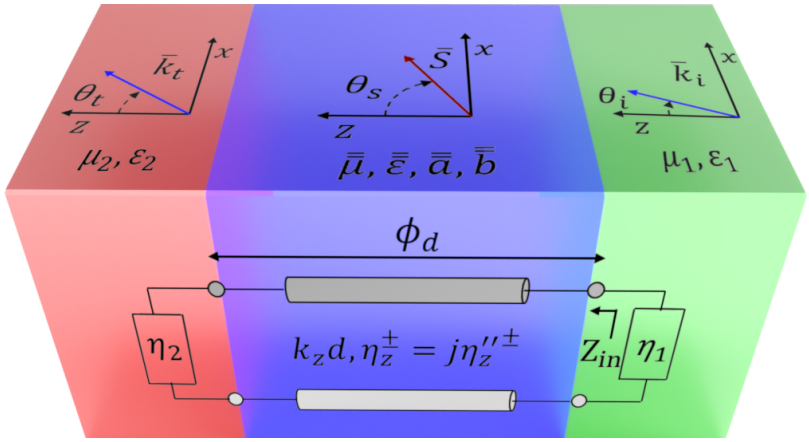

Figure 2.11: Front face: TL analogy for analyzing propagation through a slab separating two half spaces characterized by their wave impedances η_1 and η_2. Top face: Definition of the angles θ_i, θ_S, and θ_t in the corresponding regions: medium 1 (right), omega slab (center), or medium 2 (left).

power flow direction can be designed in the following manner. First, phase-matching is applied at the two boundaries of the slab then (2.40)–(2.42) and (2.45) are solved for the necessary normal wavenumber and wave impedances in the slab. Next, (2.46) is used to determine the necessary omega material parameters as a function of either the real or imaginary part of the transverse wave impedance. While the other component is given by (2.45).

As an example, an impedance matching omega slab is designed for a TE plane wave propagating from medium 1 into medium 2. The wave is incident on the slab separating the two regions of non-magnetic dielectrics. Medium 1 has $\varepsilon_r = 10$ and medium 2 is free space. The angle of incidence is $\theta_i = 10°$. The normal wave impedance in media 1 and 2 are $\eta_{z1} = 121\ \Omega$ and $\eta_{z2} = 451\ \Omega$, respectively. To limit spatial dispersion in all three regions, the unit cell dimension is chosen to be $d = \frac{\lambda_0}{10\sqrt{10}} = 0.95$ mm at 10 GHz. This results in the following lumped elements for the two isotropic grids (see Fig. 2.9a),

$$Z_{i1} = j38.71\ \Omega, \quad Y_{i1} = j4.93\ \text{mS} \tag{2.47a}$$

$$Z_{i2} = j37.55\ \Omega, \quad Y_{i2} = j0.52\ \text{mS} \tag{2.47b}$$

where Z_{i1} and Y_{i1} refer to medium 1 and Z_{i2} and Y_{i2} to medium 2. In the design of the impedance matching slab the imaginary part of the tangential wave impedance, η_x'', is a free variable and is chosen to be zero. In this case the real part of the transverse wave impedance, or equivalently μ_{zz}, is used to control the direction of power flow. In this example, the

direction of the Poynting vector is selected to demonstrate extreme redirection of power to an unbound propagating wave in the second medium. Using the design procedure outlined earlier in this section, the slab is designed to provide a normal phase delay of $\phi_d = 36^\circ$ and support a Poynting vector at $\theta_S = 89.5^\circ$ relative to the z-axis. These conditions result in the following material parameters for the slab: $\varepsilon_{yy} = 28.6\varepsilon_0$, $\mu_{xx} = 1.8\mu_0$, $\mu_{zz} = 0.013\mu_0$, $a_{xy} = -a_{yx} = -2.9\sqrt{\mu_0\varepsilon_0}$, and $a_{zy} = -a_{yz} = 0$. From (2.35), the necessary lumped impedances and admittances to implement the slab, using Fig. 2.6, are calculated,

$$\begin{aligned} Z_x &= j0.47\ \Omega,\ \ Y_{x1} = j1.89\ \text{mS},\ \ Y_{x2} = j1.89\ \text{mS} \\ Z_z &= j68.9\ \Omega,\ \ Y_{z1} = -j2.80\ \text{mS},\ \ Y_{z2} = j5.51\ \text{mS} \end{aligned} \tag{2.48}$$

For comparison, an anisotropic slab with the same power flow angle and phase delay is designed. The necessary normal wavenumber, k_z, and wave impedance, η_z, for the anisotropic slab is also determined using 1-D TL analysis, as shown in Fig. 2.11 with $\eta_z'' = 0$. Solving for the normal wavenumber in terms of the normal phase delay yields,

$$\tan k_z d = \frac{\eta_{z2}}{\eta_z} \tan \phi_d \tag{2.49}$$

In order to minimize reflections, the normal wave impedance of the slab is optimized since impedance matching with an arbitrary phase delay is not possible with an anisotropic medium. The normal wave impedance is optimized by solving for the magnitude of the reflection coefficient as a function of the normal wave impedance in the anisotropic medium, $|\Gamma(\eta_z)|$. By applying the first and second derivative tests to $|\Gamma(\eta_z)|$, the wave impedance is found in terms of the normal phase delay, impedance of the incident wave (η_{z1}), and load impedance (η_{z2}). This procedure yields the following optimal wave impedance,

$$\eta_z = \frac{|\sin\phi_d|\eta_{z2}}{\sqrt{(\cos^2\phi_d + (\frac{\eta_{z2}}{\eta_{z1}})^2 \sin^2\phi_d)^{1/2} - \cos^2\phi_d}} \tag{2.50}$$

Using the optimal normal wave impedance, η_z, for the anisotropic medium, and the wavenumber from (2.49), the following material properties are calculated for the anisotropic medium: $\varepsilon_{yy} = 9.4\varepsilon_0$, $\mu_{xx} = 2.8\mu_0$, $\mu_{zz} = 26.4\mu_0$. The anisotropic slab was implemented using the lumped element unit cell shown in Fig. 2.9b with the following lumped elements,

$$Z_x = j987.93\ \Omega,\ \ Z_z = j67.17\ \Omega,\ \ Y = j7.0\ \text{mS} \tag{2.51}$$

The anisotropic and omega slabs were simulated in Keysight's ADS using a grid similar to Fig. 2.10. The results are shown in Fig. 2.12a and 2.12b, for a domain where each

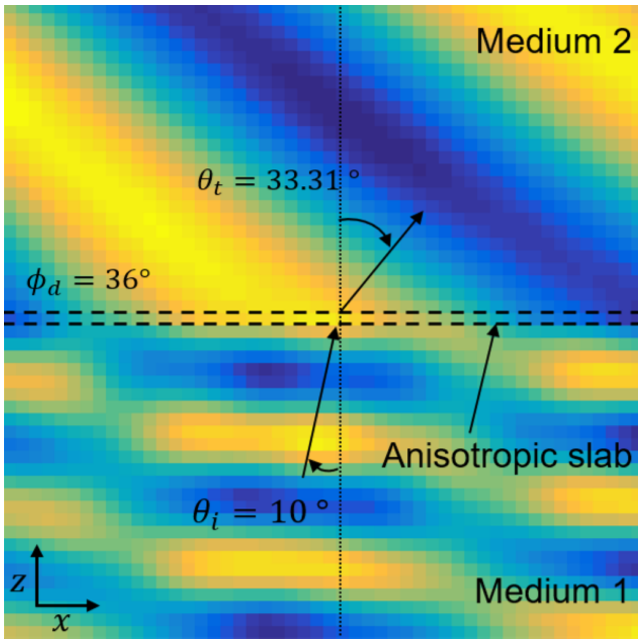

(a)

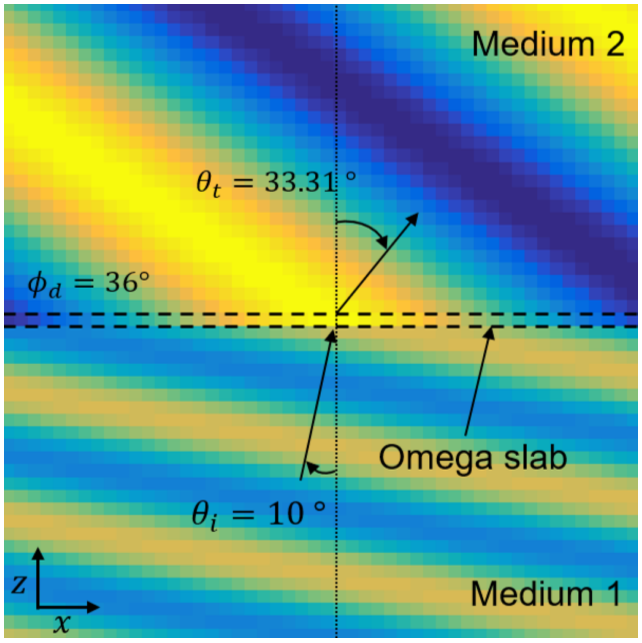

(b)

Figure 2.12: Simulation results using Keysight's ADS for the instantaneous voltage (electric field) when a TE wave is incident at $\theta_i = 10°$ on either the (a) anisotropic or (b) omega slab. The slabs are designed to provide a phase delay $\phi_d = 36°$ in the z-direction and supports a Poynting vector directed at $\theta_S = 89.5°$. The anistropic slab provides the appropriate phase delay, but suffers from significant reflections even for an optimized impedance value. In contrast to the anisotropic slab, the omega slab provides the desired phase delay and is reflectionless.

isotropic region is $25\text{x}51$ unit cells and the slabs are $1\text{x}51$ unit cells. In both cases there is a phase delay of 36°. Since the optimal wave impedance for the anisotropic slab results in a reflectance of $|\Gamma|^2 = 0.13$, there are appreciable reflections present in Fig. 2.12a. However, there are no reflections for the omega slab, as shown in Fig. 2.12b.

To verify the direction of power flow within the omega slab, the slab was illuminated by a Gaussian beam with a beam waist, $w_0 = 5.4\lambda_0$. The incident and transmitted power densities across the slab were simulated in Keysight's ADS for a $3\text{x}601$ grid, similar to Fig. 2.10, where all three regions are composed of $1\text{x}601$ unit cell grids. In Fig. 2.13, it is observed that the beam is laterally shifted by $0.63\lambda_0$ over a distance of approximately $0.03\lambda_0$. This lateral shift does not correspond to an angle of 89.5°. This is due to the presence of forward and reverse traveling waves in the impedance matching omega slab, resulting in a different net power flow angle. The theoretical net power flow angle across the slab is calculated by determining the total fields in the slab and finding the average transverse and normal power densities to calculate the average Poynting vector. This procedure results in a theoretical average power flow angle of 87.9° if $\theta_S = 89.5^\circ$ in the slab. The simulated direction of power flow was found to be 87.3°, which is in close agreement with the theoretical value. The 0.6° difference is likely due to the fact that the Gaussian beam is not a plane wave and the theoretical value assumes a plane wave illumination.

2.7 Summary

A circuit-based approach to synthesizing and simulating 2-D omega materials was presented. A 2-D periodic circuit network, composed of four 1-D asymmetric transmission (ABCD) matrices (constituent networks) was analyzed. Then an equivalency between the periodic circuit network and an omega medium was established in the homogeneous limit. For validation, the propagation characteristics of a lumped element unit cell emulating an omega medium was simulated in the commercial circuit solver Keysight ADS. These results were in close agreement with those of the analogous omega medium.

Additionally, a 2-D omega medium was used to design an impedance matching layer that utilizes normal polarizabilities to control power flow. The impedance matching layer provides a desired normal phase delay and laterally translates an incident beam's power density profile. The impedance matching layer illustrates the extreme control over phase and power that 2-D omega media offer while remaining electrically small. This capability makes them a promising candidate to reduce the size of beamforming networks.

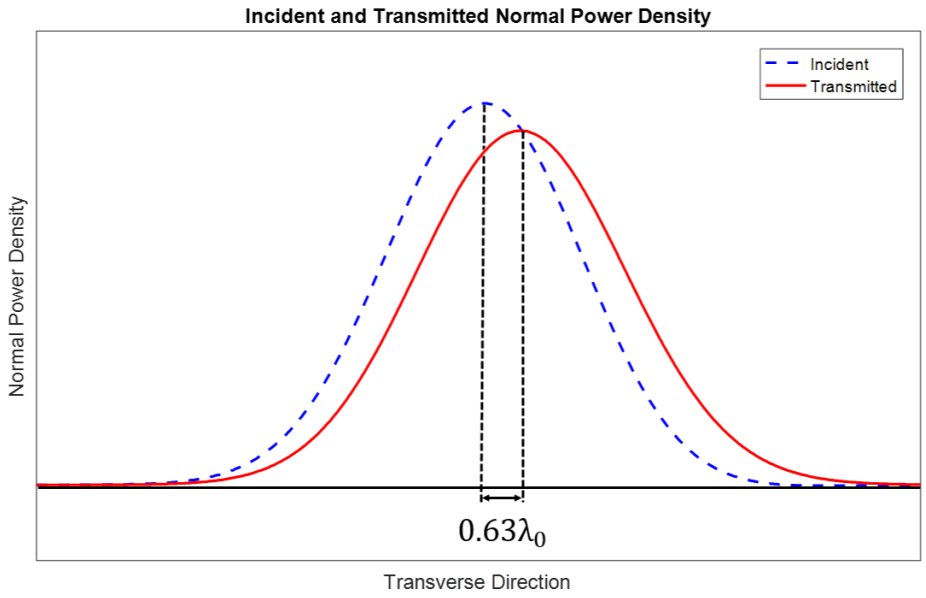

Figure 2.13: The incident and transmitted normal power density profiles along the boundaries of the omega matching layer with a Gaussian illumination, $w_0 = 5.4\lambda_0$, simulated using Keysight's ADS. The incident power density (dashed line) profile is shifted in the transverse direction. The lateral shift of the peak in transmitted power density (solid line) profile corresponds to a lateral displacement of $0.63\lambda_0$ over a distance of 0.03 λ_0. Note that the total power across the slab is conserved. The broadening of the transmitted profile accounts for the observed decrease in peak amplitude, so it is lossless and reflectionless as expected.

CHAPTER 3

Inverse Design of Multi-input Multi-output Metastructures

3.1 Introduction

In the previous chapter, a method for modeling 2D omega bianisotropic media using a circuit-based unit cell was provided. There it was shown that 2D omega bianisotropic metamaterials can be used to design reflectionless devices that provide control over the transmission phase and direction of power flow. However, it did not provide a method for designing devices that are capable of performing arbitrary sets of field transformations. In this chapter, a synthesis method for metastructures that are capable of multiple field transformations is introduced.

The need for electromagnetic devices that can perform multiple field transformations, or exhibit MIMO functionality, arises in many applications such as in antenna beamforming, mode conversion, and recently for analog signal processing [15, 48, 68]. A promising route to the realization of these devices is through metastructured, or subwavelength textured, devices. Metastructured devices provide large degrees of freedom allowing for a single device to perform multiple field transformations. However, the design of MIMO metastructured devices requires the solution of an inverse design problem. This entails the determination of a set of unknown device characteristics, such as its geometry or material parameters, from a set of known inputs and outputs. Inverse design problems like these often lack direct solution methods and require heuristic or optimization-based methods to be solved. Heuristic methods can significantly simplify the design problem making it analytically tractable. However, they often impose limitations on the possible inputs and outputs, and have inherent errors associated with them. To avoid the limitations of heuristic methods an optimization-based approach is adopted in this work to design MIMO metastructured devices.

Previous work in the design of MIMO metastructured devices has included optimization-based design procedures that have been used to realize beamforming networks [16, 52], and analog signal processors, [15, 48]. The design procedures in [15, 16, 52] use full-wave solutions to Maxwell's equations to solve the forward problem at every step of the optimization routine. This imposes a high computational cost on these design methods and places practical limitations on their ability to produce large, complex device's. In [48], a method to reduce the computational cost of the forward problem was introduced that used a combination of full-wave solutions and the paraxial approximation to design a cascade of metasurfaces with MIMO functionality. However, only amplitude control of the transmitted field profiles was considered. The aim of this work is to provide an optimization-based procedure for designing MIMO metastructured devices with control over both the amplitude and phase of the transmitted fields.

Optimization-based inverse design of metastructured devices presents a computational challenge for two main reasons: (1) The large number of forward problems that need to be solved with different design parameters. (2) The multi-scale nature of the forward problem: subwavelength features in the unit cells and a multi-wavelength device size. The first difficulty is unavoidable so the forward problem solver must be fast. The second difficulty makes the forward problem solver slower, particularly when full-wave solutions are used. Here, these issues are addressed using a fast 2-D circuit network solver that uses reduced-order models for the unit cells of the metastructured device.

The design procedure implemented in this work poses the input-output relationship of a MIMO metastructured device as an optimization problem over the design variables. To realize the devices, the optimization problem is solved using a fast 2-D circuit network solver in conjunction with a gradient-based optimization routine that uses the adjoint variable method to efficiently calculate the gradient [14, 48, 54]. The utility of the proposed design procedure is demonstrated through the design of a planar beamformer and an analog signal processor for aperture field decomposition.

3.2 Design approach

3.2.1 2-D Circuit Network Solver

In this section, a frequency domain solver for 2-D structures supporting either transverse electric (TE) or transverse magnetic (TM) polarized fields is introduced. Numerical solutions to these types of problems typically use full-wave methods like finite-difference frequency-domain, finite element methods, or the method of moments. These solution

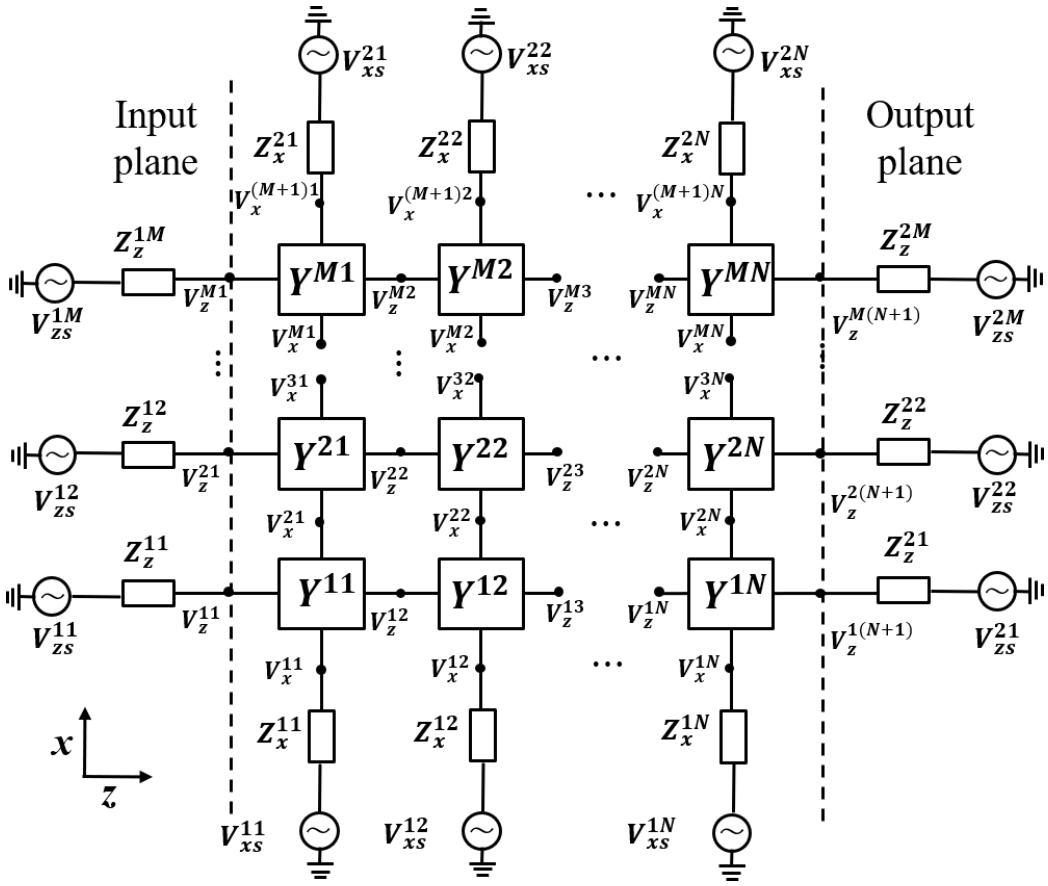

Figure 3.1: A metastructure (computational domain) consisting of an MxN grid of four-port admittance matrices. The boundary conditions are imposed using lumped element impedances and voltage sources. The voltages at all nodes are solved for by enforcing current conservation (KCL) at each node in the network.

methods are very accurate, however, for electrically-large aperiodic metastructures they are computationally expensive and are impractical to use in their inverse design. Since full-wave solutions are restrictive, alternative solution methods are required to reduce the computational cost of solving the forward problem. Here, this is done by approximating the full-wave solution using reduced-order models of the unit cells and modeling the unit cell interactions with circuit theory, similar to [20]. Solving for the device response this way is particularly useful when dealing with port-fed problems like guided-wave structures. In these scenarios, the unit cells can be characterized in isolation to produce good reduced-order models, and the coupling between the unit cells is primarily through their ports. The combination of these attributes allows for the response of complex large structures to be predicted with good accuracy.

To derive the system of equations that govern the 2-D circuit network solver a unit cell is selected and the device (computational domain) is discretized. Since circuit theory is

used to model the unit cell coupling a natural representation for a 2-D unit cell is a general four port network. These four port networks can be represented by scattering matrices, wave matrices, or impedance/admittance matrices, but admittance matrices are used here. Discretizing the computational domain into an MxN grid with unit cells defined by four-port admittance matrices results in the overall circuit shown in Fig. 3.1. It produces a staggered grid of nodal voltages that is organized into two sub-grids: the V_x and V_z grids. The V_x grid represents propagation along the x-direction, and these nodal voltages are referred to as V_x^{ij}. The V_z grid represents propagation along the z-direction, and these nodal voltages are referred to as V_z^{ij}. Since the computational domain is finite in size, the periphery of the grid is truncated using voltage sources connected in series with lumped impedances. They are used to excite the device and enforce desired boundary conditions.

To solve for the voltages in the network, Kirchoff's Current Law (KCL) is imposed at every node in the network. This produces a sparse linear system whose solution is the voltage at every node in the network.

$$\mathbf{v} = \overline{\overline{Q}}^{-1}\mathbf{s} \tag{3.1}$$

In (3.1), $\overline{\overline{Q}}$ characterizes all of the interactions between the unit cells in the network, **v** is a vector containing all of the nodal voltages, and **s** is a vector containing the source terms. To determine the structure of $\overline{\overline{Q}}$ and **s**, a grid with M unit cells in the x-direction and N unit cells in the z-direction is considered. There are six types of nodes that need to be accounted for: interior nodes on the V_x grid, interior nodes on the V_z grid, and the nodes on the four boundaries. The two different types of interior nodes and the boundary nodes along the input plane are shown in Fig. 3.2. The three other boundary nodes can be formed in a manner analogous to Fig. 3.2 (c).

The elements of $\overline{\overline{Q}}$ and **s** in (3.1) are found in the following manner. For a general interior node V_x^{ij} on the V_x grid, shown in Fig. 3.2 (a), KCL leads to the following equation,

$$\begin{aligned} &V_x^{ij}(Y_{11}^{ij} + Y_{33}^{(i-1)j}) + V_x^{(i-1)j}Y_{31}^{(i-1)j} + V_x^{(i+1)j}Y_{13}^{ij} \\ &+ V_z^{ij}Y_{12}^{ij} + V_z^{(i-1)j}Y_{32}^{(i-1)j} + V_z^{(i-1)(j+1)}Y_{34}^{(i-1)j} \\ &+ V_z^{i(j+1)}Y_{14}^{ij} = 0 \end{aligned} \tag{3.2}$$

Applying KCL at a general interior node V_z^{ij} on the V_z grid, shown in Fig. 3.2 (b), leads to

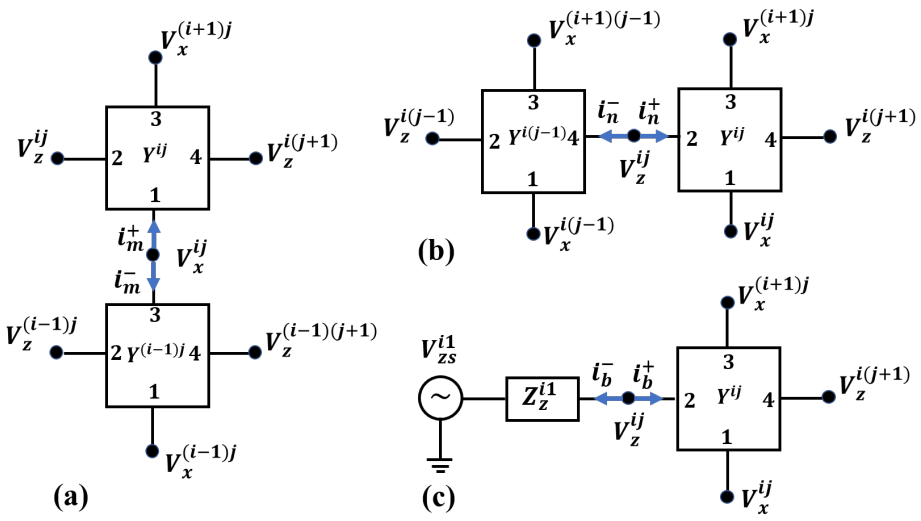

Figure 3.2: (a) An internal node on the x-grid. (b) An internal node on the z-grid. (c) A boundary node along the input plane in Fig. 3.1. The other boundaries can be obtained in a manner analogous to (c).

the following equation,

$$\begin{aligned} &V_z^{ij}(Y_{22}^{ij} + Y_{44}^{i(j-1)}) + V_z^{i(j-1)}Y_{42}^{i(j-1)} + V_z^{i(j+1)}Y_{24}^{ij} \\ &+ V_x^{ij}Y_{21}^{ij} + V_x^{(i+1)j}Y_{23}^{ij} + V_x^{(i+1)(j-1)}Y_{43}^{i(j-1)} \\ &+ V_x^{i(j-1)}Y_{41}^{i(j-1)} = 0 \end{aligned} \tag{3.3}$$

Applying KCL at the four types of boundary nodes (see Fig. 3.1) produces the following equations: the left boundary V_z^{i1} (shown in Fig. 3.2 (c)),

$$V_z^{i1}(Y_{22}^{i1} + \frac{1}{Z_z^{i1}}) + V_z^{i2}Y_{24}^{i1} + V_x^{i1}Y_{21}^{i1} + V_x^{(i+1)1}Y_{23}^{i1} = \frac{V_{zs}^{i1}}{Z_z^{i1}} \tag{3.4}$$

the right boundary $V_z^{i(N+1)}$,

$$\begin{aligned} V_z^{i(N+1)}(Y_{44}^{iN} + \frac{1}{Z_z^{i2}}) + V_z^{iN}Y_{42}^{iN} + V_x^{iN}Y_{41}^{iN} \\ + V_x^{(i+1)N}Y_{43}^{iN} = \frac{V_{zs}^{i2}}{Z_z^{i2}} \end{aligned} \tag{3.5}$$

the bottom boundary V_x^{1j},

$$V_x^{1j}(Y_{11}^{1j} + \frac{1}{Z_x^{1j}}) + V_x^{2j}Y_{13}^{ij} + V_z^{1j}Y_{12}^{1j} + V_z^{1(j+1)}Y_{14}^{1j} = \frac{V_{xs}^{1j}}{Z_x^{1j}} \tag{3.6}$$

the top boundary $V_x^{(M+1)j}$,

$$V_x^{(M+1)j}(Y_{33}^{Mj} + \frac{1}{Z_x^{2j}}) + V_x^{Mj}Y_{31}^{Mj} + V_z^{Mj}Y_{32}^{Mj} + V_z^{M(j+1)}Y_{34}^{Mj} = \frac{V_{xs}^{2j}}{Z_x^{2j}}. \tag{3.7}$$

Expressing KCL at every node in the network using (3.2)-(3.7) forms a linear system of $2MN+M+N$ equations shown in (3.1). The matrix $\overline{\overline{Q}}$ can be quite large as its dimensions are $(2MN + M + N) \times (2MN + M + N)$. However, there are a maximum of seven non-zero terms in each row of $\overline{\overline{Q}}$. Therefore, when its dimensions are large it is sparse. This sparsity allows for the total device response, **v**, of large aperiodic metastructured devices to be rapidly evaluated once the admittance matrices of its unit cells are characterized.

The major advantage of solving for the device response this way is that it can maintain a high-level of accuracy if good models of the unit cells are developed while avoiding full-wave solutions at run time. Eliminating full-wave solutions reduces the computational cost of solving the forward problem significantly, making the circuit network solver useful for the optimization-based inverse design of large aperiodic metastructures. The solver does come with limitations though. One limitation is the requirement that the unit cells can be represented as a four port networks. This means that the problem of interest's unit cells must have an equivalent guided wave representation, which is not always possible if there is a continuous spectrum of propagating waves. Another limiting assumption is that all of the interactions between the unit cells can be captured using a single guided mode. Meaning that mutual coupling between the unit cells and higher-order modes excited by inclusions or discontinuities are neglected. If these interactions become significant this assumption can be relaxed, and multi-modal Y-matrices or wave matrices can be used to capture these effects, [69, 70]. Using higher-order modes is not always necessary and does increase the computational cost, which is why they were not used here.

3.2.2 MIMO Inverse Design Procedure

The fast 2-D circuit network solver introduced in the previous section solves for the output of a device given an input and all of the unit cell's admittance parameters. However, in a MIMO inverse-design problem the unit cell's admittance parameters are solved for given a set of desired inputs and outputs. In this section, an optimization-based inverse design procedure is described that achieves this goal. The desired MIMO functionality is realized by formulating the design objectives as an optimization problem that can be solved using the 2-D circuit network solver in conjunction with an off-the-shelf optimization routine. The design procedure is outlined in Fig. 3.3, and the details of how the optimization problem is formulated and solved is provided in the following subsections.

3.2.2.1 Optimization Problem

The design of a multi-input multi-output device begins with a set of inputs and outputs that describe its functionality. Here, these inputs and outputs are voltage distributions along the input and output planes of the device, see Fig. 3.1. These voltage distributions will be referred to as $\{\mathbf{v}_{\text{in}}^k\}$ for the inputs and $\{\mathbf{v}_{\text{out}}^k\}$ for the outputs where, $k \in \{1, 2, ..., K\}$ and K is the total number of input-output pairs. Here, the term input-output pair refers to an input voltage distribution and its associated output voltage distribution, $(\mathbf{v}_{\text{in}}^k, \mathbf{v}_{\text{out}}^k)$. Specifically, $\mathbf{v}_{\text{out}}^k$ are the observed voltages when the network is excited by $\mathbf{v}_{\text{in}}^k$. To realize the MIMO network described by $\{\mathbf{v}_{\text{in}}^k\}$ and $\{\mathbf{v}_{\text{out}}^k\}$ using optimization, the device's performance for each input-output pair must be represented by a single real number. This can be done with the following cost function for the k^{th} input-output pair,

$$g_k(\mathbf{p}) = \frac{1}{2}(\mathbf{v}^k(\mathbf{p}) - \mathbf{v}_{\text{out}}^k)^H \overline{\overline{G}} (\mathbf{v}^k(\mathbf{p}) - \mathbf{v}_{\text{out}}^k) \tag{3.8}$$

where $\mathbf{p}$ is a vector containing all of the design variables in the network, the vector $\mathbf{v}^k(\mathbf{p})$ contains the voltages in the network (subject to the design variables) when it is excited by $\mathbf{v}_{\text{in}}^k$, and the superscript H indicates the conjugate transpose. The matrix $\overline{\overline{G}}$ is diagonal and positive-semidefinite. It is used to select and scale the elements of $\mathbf{v}^k(\mathbf{p}) - \mathbf{v}_{\text{out}}^k$. The performance of the device over all of the input-output pairs is determined by summing (3.8) over k to produce the total cost function,

$$g(\mathbf{p}) = \sum_{k=1}^{K} g_k(\mathbf{p}) \tag{3.9}$$

Framing the problem in this way reduces the design of the multi-input multi-output network to finding the design that minimizes the total cost, i.e. the minimizer $\mathbf{p}^*$, of (3.9). This goal is represented by the following optimization problem,

$$\begin{aligned} &\arg\min_{\mathbf{p}} g(\mathbf{p}) \\ &\text{subject to :} \quad \mathbf{p}_{\text{lb}} \preceq \mathbf{p} \preceq \mathbf{p}_{\text{ub}} \end{aligned} \tag{3.10}$$

where $\mathbf{p}_{\text{lb}}$ and $\mathbf{p}_{\text{ub}}$ are vectors containing the lower and upper bounds of the design variables, respectively.

Now that the optimization problem (3.10) has been posed an appropriate optimization algorithm needs to be selected to solve it. Since the optimization problem is in general non-convex, local optimization or gradient-based algorithms are not guaranteed to find globally optimal solutions. However, global optimization algorithms do not tend to perform well in high-dimensional design spaces like the design space of a metastructured device. In high-dimensional spaces, local methods tend to outperform global methods when they use gradient information to navigate the design space. However, if the gradient cannot be expressed explicitly in closed form and the dimensions of the design space are large the computational cost of calculating the gradient can become prohibitive. To avoid this issue the adjoint variable method [14, 48, 54] can be used to calculate the gradient at a reduced computational cost. For these reasons, a gradient-based optimization routine utilizing the adjoint variable method is chosen to solve (3.10). Since it is a local method there is no guarantee of convergence to a globally optimal solution, i.e. the solution of (3.10). However, this is not a problem since the globally optimal design is not required. The required design is just one that meets the design specifications so, a solution to (3.10) is considered any design that satisfies the design specifications.

3.2.2.2 Adjoint Variable Method

As discussed in the previous section, the optimization problem, (3.10), will be solved using an off-the-shelf gradient-based optimization routine. Here, MATLAB's constrained optimization routine fmincon() is used. To improve the performance of the algorithm on large-scale problems, a user defined gradient is implemented that is calculated using the adjoint variable method. To motivate the use of the adjoint variable method, a comparison between calculating the gradient using it and using finite-differences is considered. Consider the design of a device with P design variables and K input-output pairs. Calculating the gradient of (3.9) using finite-differences requires $(P + 1) \times K$ forward solutions to (3.1). When P becomes large this is not a practical means of determining the gradient

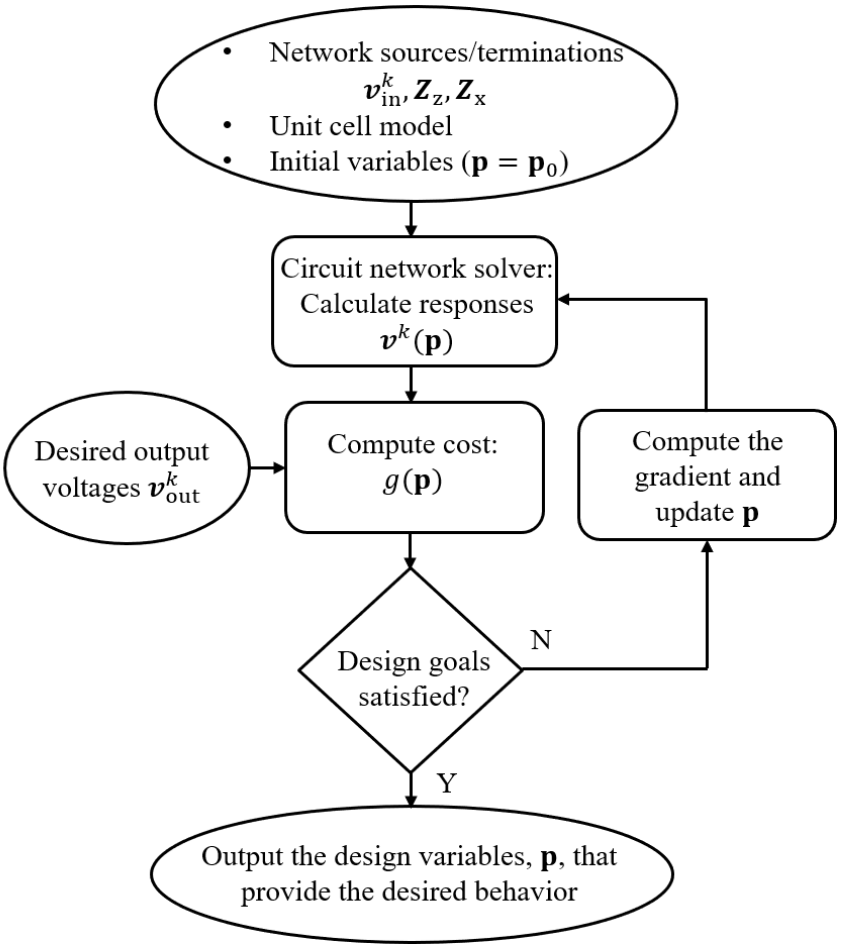

Figure 3.3: Flowchart depicting the inverse-design procedure.

especially if the dimensions of $\overline{\overline{Q}}$ are also large. On the other hand, if the adjoint variable method is used only $2 \times K$ forward solutions are required. This reduction in the number of forward problem solutions significantly accelerates the optimization routine, and is critical to enabling the inverse design of electrically-large aperiodic metastructures.

The implementation of the adjoint variable method presented here is a quasi-analytical technique for calculating the gradient of (3.9). It requires solutions to the forward problem, (3.1) and an adjoint problem associated with (3.9), [71]. The adjoint problem associated with (3.9) is formed by observing that the gradient of (3.8) can be expressed as,

$$\nabla_{\mathbf{p}}(g_k(\mathbf{p})) = -\Re\{(\mathbf{v}^k - \mathbf{v}_{\text{out}}^k)^H \overline{\overline{G}}\ \overline{\overline{Q}}_k^{-1} \overline{\overline{V}}_{\mathbf{p}}^k\} \tag{3.11}$$

where $\overline{\overline{V}}^k_{\mathbf{p}}$ is the following matrix,

$$\overline{\overline{V}}^k_{\mathbf{p}} = (\frac{\partial \overline{\overline{Q}}_k}{\partial p_1}\mathbf{v}^k|\frac{\partial \overline{\overline{Q}}_k}{\partial p_2}\mathbf{v}^k|\frac{\partial \overline{\overline{Q}}_k}{\partial p_3}\mathbf{v}^k|\ldots|\frac{\partial \overline{\overline{Q}}_k}{\partial p_P}\mathbf{v}^k) \tag{3.12}$$

This matrix can be solved for analytically if expressions for the derivatives of the admittance matrix (Y-matrix) elements in $\overline{\overline{Q}}_k$, the $\overline{\overline{Q}}$ matrix for the kth input-output pair, are available to determine $\frac{\partial \overline{\overline{Q}}_k}{\partial p_i}$. Otherwise, it can be obtained using finite-differences to approximate $\frac{\partial \overline{\overline{Q}}_k}{\partial p_i}$ at a low computational cost. The efficiency of calculating the gradient using (3.11) can be improved by observing that the product on the right hand side of (3.11), excluding $\overline{\overline{V}}^k_{\mathbf{p}}$, forms a vector, $\boldsymbol{\lambda}^H_k$, that can be solved for independently,

$$\boldsymbol{\lambda}^H_k = (\mathbf{v}^k - \mathbf{v}^k_{\text{out}})^H \overline{\overline{G}}\ \overline{\overline{Q}}_k^{-1} \tag{3.13}$$

Rearranging this expression yields the adjoint problem associated with (3.8),

$$\overline{\overline{Q}}^H_k \boldsymbol{\lambda_k} = \overline{\overline{G}}(\mathbf{v}^k - \mathbf{v}^k_{\text{out}}). \tag{3.14}$$

This allows for the adjoint variable λ_k to be computed at the cost of solving a forward problem of equal complexity to the original problem (3.1). Using (3.13) in (3.11) yields,

$$\nabla_{\mathbf{p}}(g_k(\mathbf{p})) = -\Re\{\boldsymbol{\lambda}^H_k \overline{\overline{V}}^k_{\mathbf{p}}\} \tag{3.15}$$

Expressing (3.11) in this way provides a means of obtaining the gradient of the kth cost function, (3.8), at the computational expense of effectively two forward problem solutions. The gradient of (3.9) is then obtained by summing (3.15) over k,

$$\nabla_{\mathbf{p}}(g(\mathbf{p})) = -\sum_{k=1}^{K} \Re\{\boldsymbol{\lambda}^H_k \overline{\overline{V}}^k_{\mathbf{p}}\}. \tag{3.16}$$

Therefore, in a problem containing P design variables the gradient can be determined with $2 \times K$ forward problem solutions using (3.16). Rather than the $(P + 1) \times K$ forward problem solutions required by finite-differences.

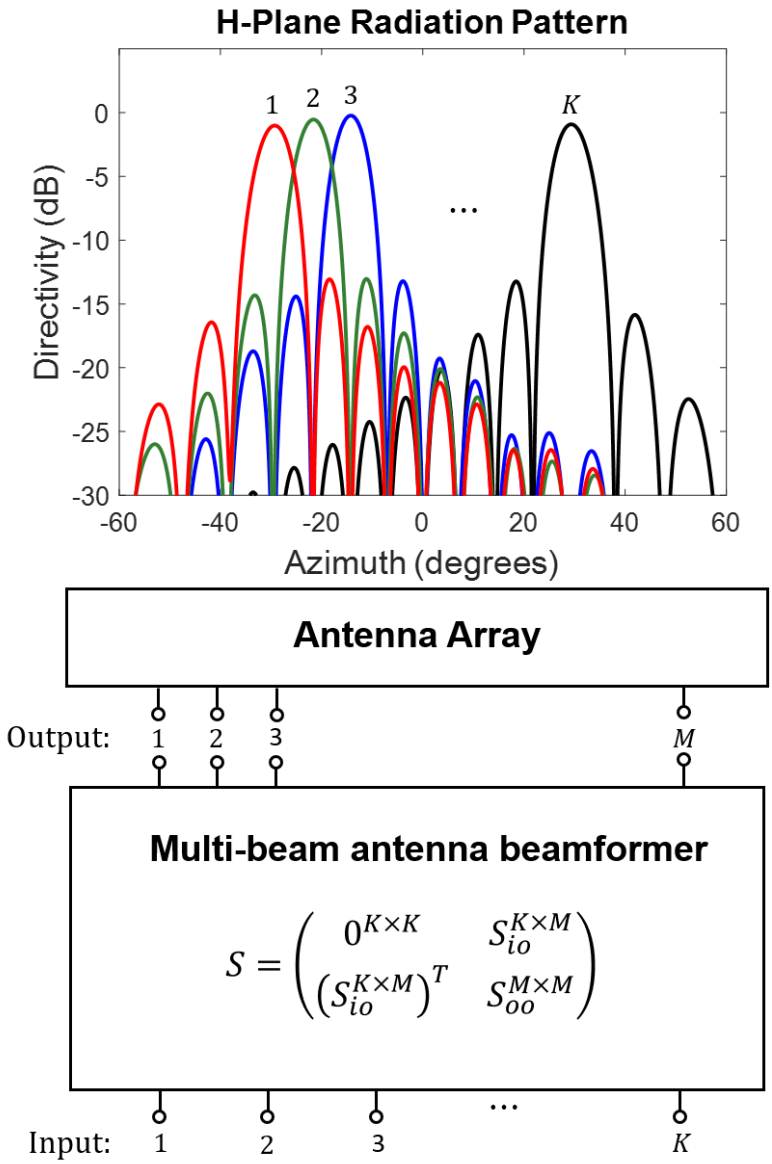

Figure 3.4: A block diagram of a multi-beam antenna system. It is composed of an antenna array and a reciprocal beamformer that can produce K beams simultaneously. The upper left block of the beamformer's S-matrix is $0^{K\text{x}K}$ indicating that its input ports are impedance matched and decoupled. The block $S_{io}^{K\text{x}M}$ determines the aperture field produced by exciting each of the input ports. The elements of $S_{oo}^{M\text{x}M}$ are free variables, and are neglected in the design of the beamformer.

3.3 Design Examples

3.3.1 Planar Metastructured Beamformer

To demonstrate the effectiveness of the design procedure presented in Section III the multi-beam antenna beamformer shown in Fig. 3.4 is designed. The beamformer designed using this framework provides several advantages over Butler matrices and quasi-optical beamformers such as the Rotman lens, [72], the Luneburg lens, [73], or beamformers based on transformation optics [74]. The advantage of the proposed design procedure is that it allows for perfect control of both the amplitude and phase of every aperture field. In contrast, a Rotman lens lacks amplitude control and provides perfect phasing for a maximum of three aperture fields. The Luneburg lens produces identical aperture fields for all scan angles but the amplitude pattern cannot be controlled. To control amplitude, the design method reported in [74] can be used. However, this design method allows for perfect phasing and amplitude control of only one aperture field. Butler matrices provide an alternative to quasi-optical beamformers, and they can theoretically produce an arbitrary number of perfectly phased uniform amplitude aperture fields, [75]. However, Butler matrices are limited to uniform aperture fields for single port excitations. Whereas beamformers designed using the procedure presented in Section III have no inherent restrictions on the possible aperture fields, and could be advantageous when designing beamformers for antenna arrays with deeply subwavelength element spacings and high input impedances like tightly coupled or connected arrays, [76].

3.3.1.1 Design Specifications

The beamforming region is assumed to be lossless and reciprocal and is designed to produce nine beams that are each associated with a different input port. It will operate at 10 GHz and is intended for use with an aperture antenna that has a width of $W_{ap} = 8\lambda_0$. To produce a close approximation to a continuous aperture field the spacing between the output ports is chosen to be $\lambda_0/10$. This determines the discretization of the beamforming region and thus the unit cell size. The width of the beamformer is the same as the width of the aperture antenna, $8\lambda_0$, and the depth is chosen to be $2.4\lambda_0$. This depth was selected to provide sufficient distance to spread out the input power without utilizing cavity effects from the edges of the beamformer. Therefore, the overall dimensions of the beamformer are $8\lambda_0 \times 2.4\lambda_0$. This corresponds to a network with $M = 80$ unit cells in the transverse direction and $N = 24$ in the longitudinal direction.

The nine inputs to the network are $70\ \Omega$ port excitations located along the input plane,

shown in Fig. 3.1. The inputs are spaced by $0.8\lambda_0$ starting from the center line of the beamformer. This spacing aids in isolating the input ports from each other: a requirement for the simultaneous excitation of the beams. The requirement of isolation between the input ports and losslessness mandate that the radiated fields are orthogonal over a period of the radiation pattern [77]. This restricts the possible aperture fields and must be considered when selecting the desired radiation patterns of the aperture antenna. A well known set of functions that satisfy mutual orthogonality are sinc functions with appropriate angular spacings. For this reason, the aperture fields are chosen to have uniform amplitude with linear phase gradients corresponding to the following tangential wavenumbers,

$$k_n = \frac{2\pi n}{Md},\ n \in \{0, \pm 1, \pm 2, ..., \pm(M-1)\}. \tag{3.17}$$

In (3.17), d is the spacing between the output ports and M is the total number of output ports. In this design the nine beams correspond to $n = 0, \pm 1, \pm 2, \pm 3, \pm 4$. Since $d = \lambda_0/10$ and $M = 80$, these correspond to beams at $\theta_n = 0°, \pm 7.18°, \pm 14.48°, \pm 22.02°, \pm 30°$. The output terminations are given by the input impedance of the aperture antennas ports. The input impedance for each port is $140\ \Omega$ at broadside so, the output terminations for each of the n excitations are given by $140\ \Omega/\cos\theta_n$. The remaining ports in Fig. 3.1 along the top and bottom of the beamformer, as well as the unused ports along the input plane are terminated in open circuits. Alternatively, the exact termination presented by each antenna at the output ports could be included directly in the design process. This would only require a slight modification to the forward problem solver. An M-port termination at the output plane would need to be included altering (3.5). Then an M-port admittance matrix of the antenna could be characterized and included in the design process.

3.3.1.2 Unit Cell Design

In order to use the design procedure presented in Section III, a suitable unit cell must be chosen and characterized. The unit cell should contain the maximum number of degrees of freedom to allow for extreme field transformations with a compact design, be easy to tile in a plane, and provide a broadband response. For ease of tiling a square unit cell, with dimensions dxd where d $= 3$ mm, is chosen. A TL unit cell is selected to ensure a broadband response and that the designed beamformer can be manufactured using a standard printed-circuit board (PCB) process. To determine how many design variables should be included, consider that an arbitrary lossless and reciprocal four-port admittance matrix has a maximum of ten degrees of freedom. However, due to field averaging arguments, the degrees of freedom are reduced to effective material parameters in electrically-small

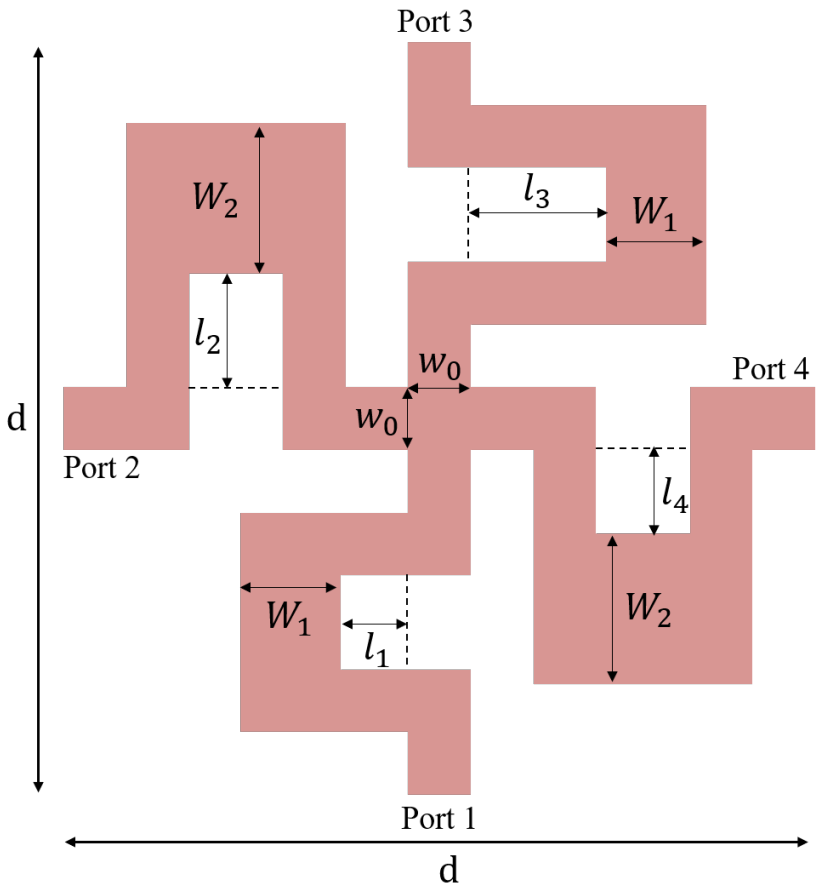

Figure 3.5: The microstrip unit cell used in the design of the metastructured beamformer and the analog signal processor. The square unit cell has dimensions dxd. It possesses six degrees of freedom, $W_1,\ W_2,\ l_1,\ l_2,\ l_3,$ and l_4 that can be varied to realize a variety of four-port admittance matrices. The microstrip lines at the input ports, central junction, and the lines corresponding to $l_1,\ l_2,\ l_3,$ and l_4 have a constant width of w_0.

structures, [78, 79]. The beamformer can be viewed as a lossless, reciprocal, polarization conserving medium supporting a TE wave in the x-z plane. The most general medium supporting this type of propagation is a 2-D omega medium that conserves polarization, i.e. a medium with the following material properties,

$$\overline{\overline{\mu}} = \begin{pmatrix} \mu_{xx} & \mu_{xz} \\ \mu_{xz} & \mu_{zz} \end{pmatrix}, \quad \varepsilon_{yy}, \quad \overline{\overline{a}} = \overline{\overline{b}} = j \begin{pmatrix} 0 & a_{xy} & 0 \\ -a_{xy} & 0 & a_{zy} \\ 0 & -a_{zy} & 0 \end{pmatrix}$$

where, $\overline{\overline{a}}$ and $\overline{\overline{b}}$ are the magneto-electric and electro-magnetic tensors, respectively. This perspective provides some guidance for designing the unit cell. It points to the fact that a maximum of six design variables should be included in the unit cell. Additional de-

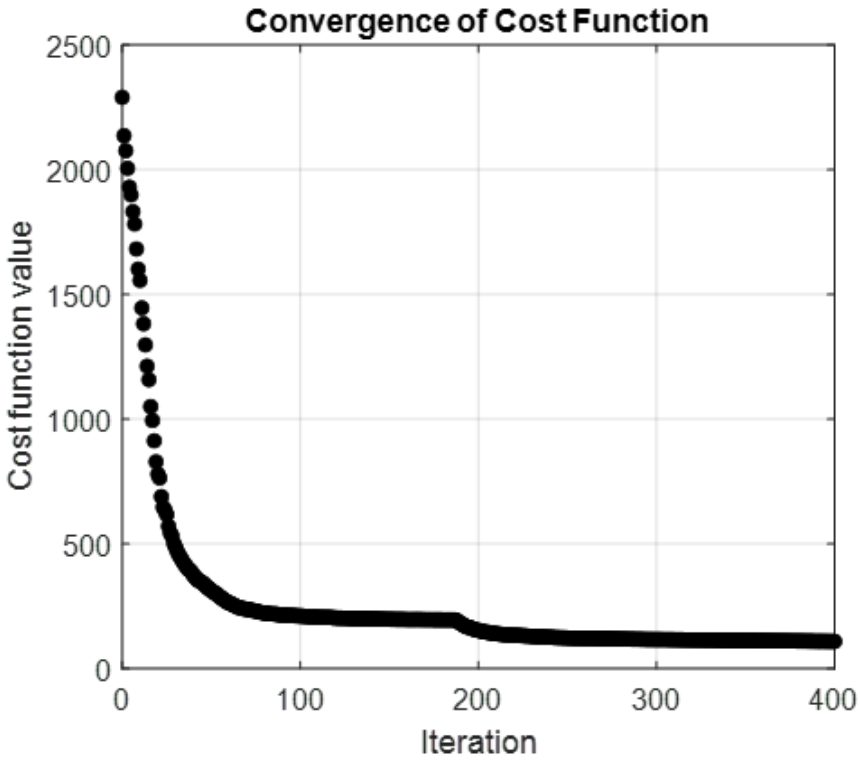

Figure 3.6: Plot of the cost function behavior for the planar metastructured beamformer design.

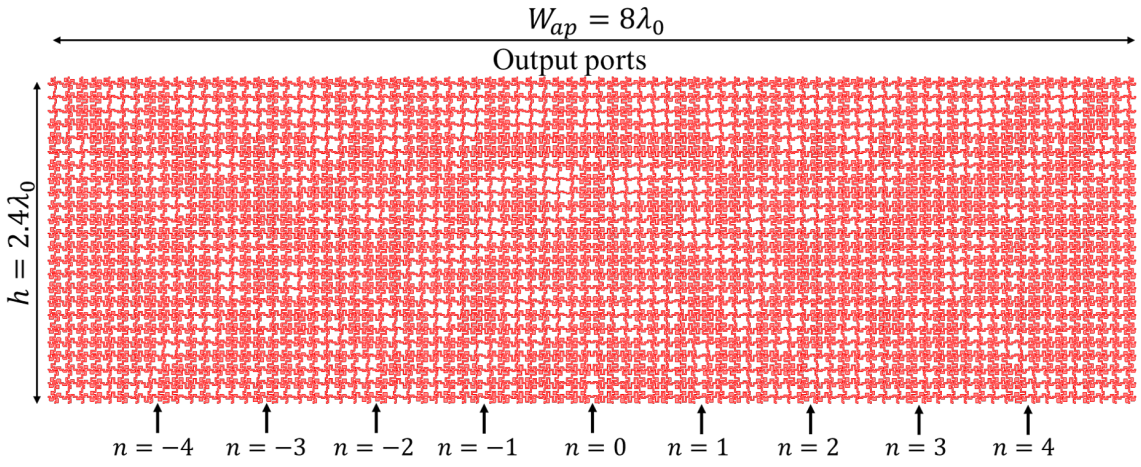

Figure 3.7: The patterned metastructured beamformer produced by the proposed inverse-design procedure. There are nine input ports that each produce unique voltage distributions across the 80 output ports to form the desired aperture fields. These aperture fields produce beams at $\theta_n = 0°, \pm 7.18°, \pm 14.48°, \pm 22.02°, \pm 30°$. The beamformer is designed to work at 10 GHz and is composed of 1920 unit cells. The width of the aperture is $W_{ap} = 8\lambda_0$ (24cm) and the beamformer has a depth of $h = 2.4\lambda_0$ (7.2 cm).

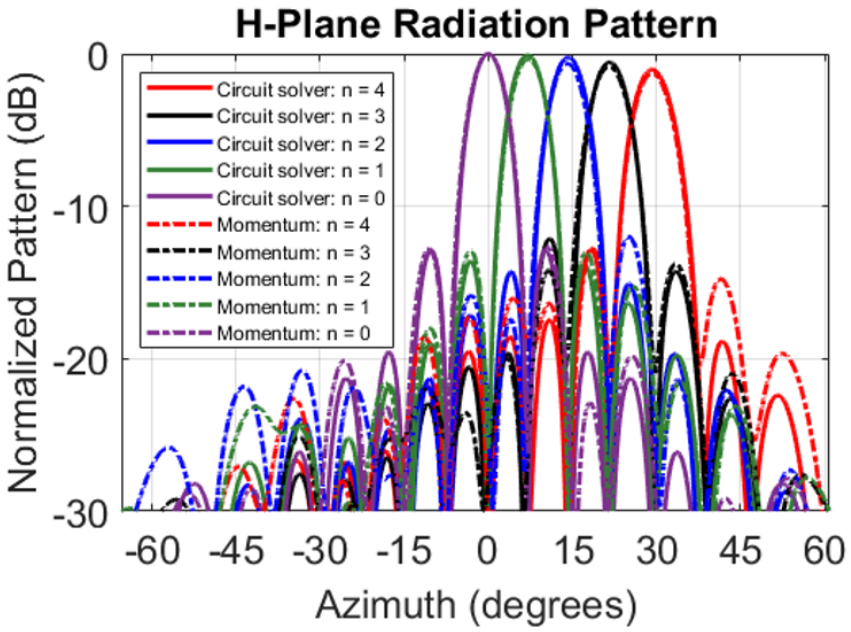

Figure 3.8: Radiation from an aperture antenna excited by the output voltages of the beamforming network: dashed lines correspond to the radiation pattern from the desired voltages and the solid lines correspond to the voltages calculated using the circuit network solver. For clarity, only beams corresponding to positive scan angles are shown since the beams corresponding to negative scan angles are identical due to symmetry.

sign variables will only complicate the characterization of the unit cell without producing observable degrees of freedom in the response. It also provides information on what characteristics of the unit cell the design variables should affect. The design variables should control: (1) The path lengths in the x and z directions, as well as coupling between the two directions to change $\overline{\overline{\mu}}$. (2) The TL widths to change ε_{yy}. (3) The asymmetry in the x and z directions changes the bianisotropic response, $\overline{\overline{a}}$.

For these reasons the unit cell depicted in Fig. 3.5 is selected. It is composed of four branches of microstrip TLs meeting at a cross junction in the center. To avoid parasitic effects when interconnecting the unit cells, the TL width at all of the ports is a constant value of $w_0 = 0.25$ mm. There are six degrees of freedom in the unit cell: four lengths and two widths. Each branch contains one of the four length variables. While one of the width variables is in the x-directed branches and the other width variable is in the the z-directed branches.

To design the beamformer, the unit cell admittance parameters need to be available as continuously differentiable functions of the lengths and widths. Here, this is achieved by constructing a reduced-order model of the unit cell from a database of full-wave simulations. The unit cells in the database were characterized in isolation using Keysight's

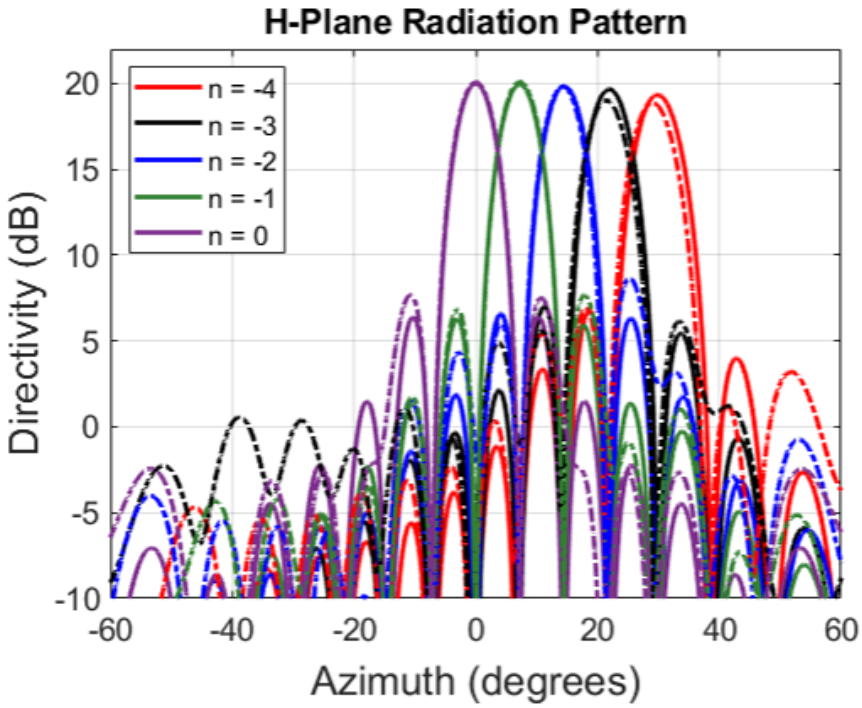

Figure 3.9: Radiation from an aperture antenna excited by the output voltages of the beamforming network: solid lines correspond to the radiation pattern from the voltages calculated using the circuit network solver and the dot-dashed lines correspond to the voltages calculated using the full-wave results. For clarity, only beams corresponding to positive scan angles are shown since the beams corresponding to negative scan angles are identical due to symmetry.

Momentum, and a model of Rogers RO5880 substrate neglecting dissipative losses was used. The substrate has a height of $h = 0.787$ mm and a relative permittivity $\varepsilon_r = 2.2$. The design variables for each unit cell in the database are chosen to form a uniformly spaced grid of the allowable lengths and widths in the design space. The allowable range of widths is $0.2 \leq W_{1,2} \leq 0.8$ mm and the lengths are allowed to vary between $0 \leq l_i \leq l_i^{max}$. Where $l_i^{max} = d/2 - w_0/2 - W$ and W corresponds to the width of the line which is connected to l_i for $i \in \{1, 2, 3, 4\}$. The lower bound on the width is chosen to avoid thin, lossy TLs and the upper bound is chosen to allow for sufficient variation in the length variables for all the width values. The admittance parameters from the database were then spline interpolated using MATLAB's gridded data interpolation function griddedInterpolant() using the modified Akima method. This results in a unit cell model that is C^1 differentiable with respect to the length and width variables, which is suitable for use in a Quasi-Newton optimization procedure.

3.3.1.3 Optimization and Results

Since the beamformer produces symmetric beams, the beamformer should be symmetric as well. For this reason symmetry is imposed across the center line in the forward problem solver. This results in the device having 5,760 design variables. The design variables are solved for by providing the optimization routine with the input and output terminations, the model of the unit cell, and an initial guess of uniform lengths and widths for the design variables. The algorithm then searched the design space to find a set of design variables that produce the desired input field profiles (impedance matched and isolated input ports) and output field profiles. The algorithm converged on a satisfactory design after 400 iterations (approximately 6 hours of execution) on a personal computer with an i7-9700 CPU @ 3GHz w/8 cores and 64GB RAM. The convergence of the cost function is shown in Fig. 3.6, and the layout of the design is shown in Fig. 3.7.

To evaluate the performance of the beamformer, the radiation pattern from an ideal aperture antenna fed by the beamformer is computed using MATLAB. The calculation assumes that the aperture has width of $W_{ap} = 8\lambda_0$, a height of $H_{ap} = 1\lambda_0$, and the electric field across the aperture has a piece-wise uniform amplitude and phase. The equivalent magnetic currents are then determined and the total radiated electric field is calculated. The radiation patterns resulting from the circuit network solver (forward problem solver) are in excellent agreement with the desired beams, as shown in Fig. 3.8. The lowest aperture efficiency is $e_a = 0.99$ occurring for the broadside beam ($n = 0$). The beamformer inputs have a worst case isolation of 24.5 dB and a worst case reflectance of -31.5 dB for the broadside excitation. These results are then compared to a full-wave simulation of the beamformer performed in Keysight Momentum using the Green's function for an infinite substrate that possesses the same characteristics as the unit cells. The simulation, the equivalent of one forward problem solution using Momentum, took approximately 98 hours on a high-performance computing cluster with access to 15 cores and 600 GB RAM. The results of the simulation are shown in Fig. 3.9. Due to slight variations in the observed voltages at the beamformer ports, there are small shifts and a slight broadening of the beams. Resulting in a worst case aperture efficiency of $e_a = 0.945$ for excitation $n = \pm 4$. The isolation and input impedance match are slightly degraded as well. There is a worst case isolation of 13.47 dB and a maximum reflectance of -15.2dB for the broadside excitation. However, the overall agreement is quite good between the full-wave and circuit network solver results.

To characterize the bandwidth of the beamformer, simulations were performed in Keysight Momentum at 9.75, 9.875, 10.125, and 10.25 GHz. From these simulations it was determined that the beamformer's impedance bandwidth is greater than 5%. While its 3-dB

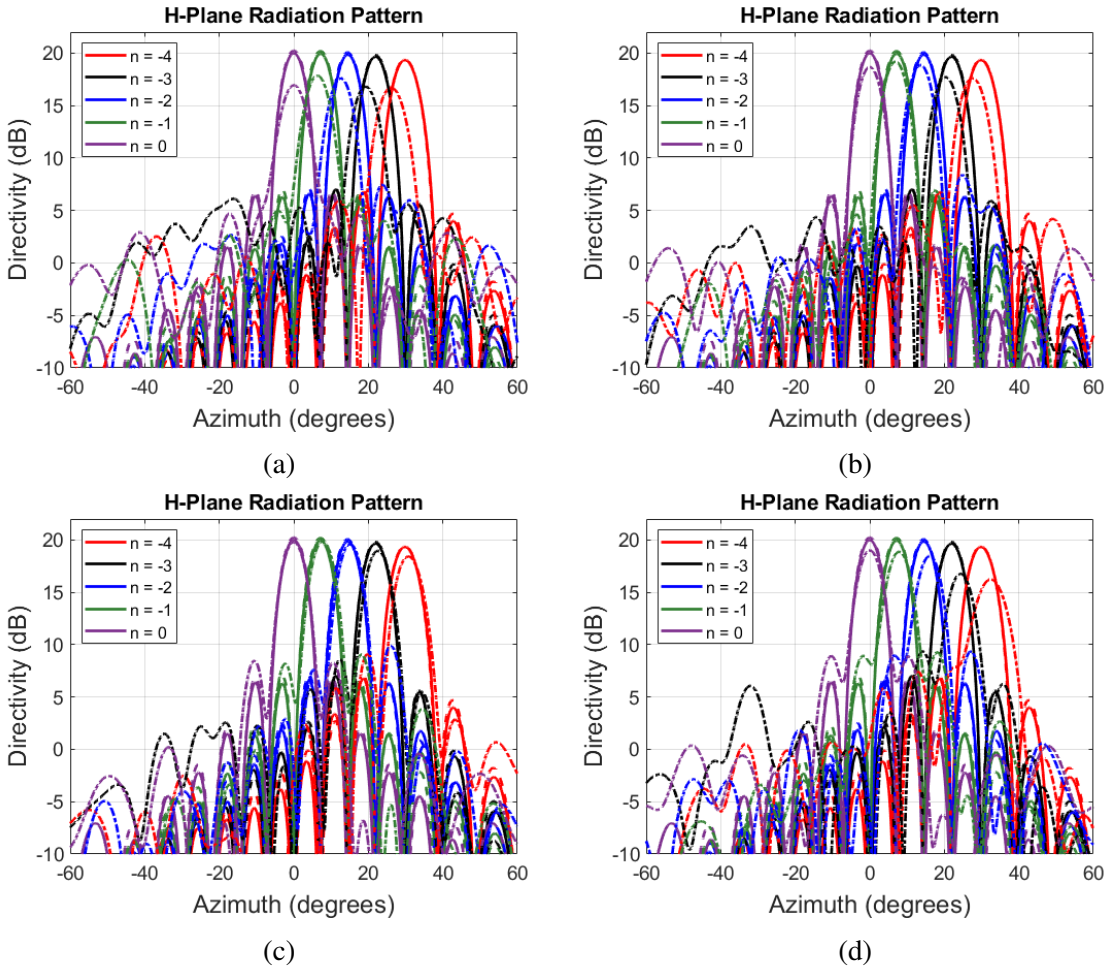

Figure 3.10: Plots of the simulated radiation patterns calculated from the full-wave results for the beamformer at: (a) 9.75 GHz (b) 9.875 GHz (c) 10.125 GHz (d) 10.25 GHz. The dashed lines indicate the simulated results and the solid lines indicate the targeted radiation patterns at 10 GHz. The maximum decrease in the directivity for each of the desired beam-pointing directions (θ_n) at each frequency is: (a) 3.77 dB for n = -4 (b) 1.64 dB for n = -4 (c) 1.07 dB for n = -4 (d) 4.55 dB for n = -3 .

directivity bandwidth is between $2.5 - 5\%$. The range of $2.5 - 5\%$ is provided since the frequencies at which the directivity was reduced by 3 dB were not determined exactly but, lie between $9.75 - 9.875$ GHz and $10.125 - 10.25$ GHz, shown in Fig. 3.10a - 3.10d. These results indicate that the beamformer is relatively narrowband. However, the bandwidth was not considered during the design process, by altering the cost function to include the performance at multiple frequencies the bandwidth of the beamformer could be improved.

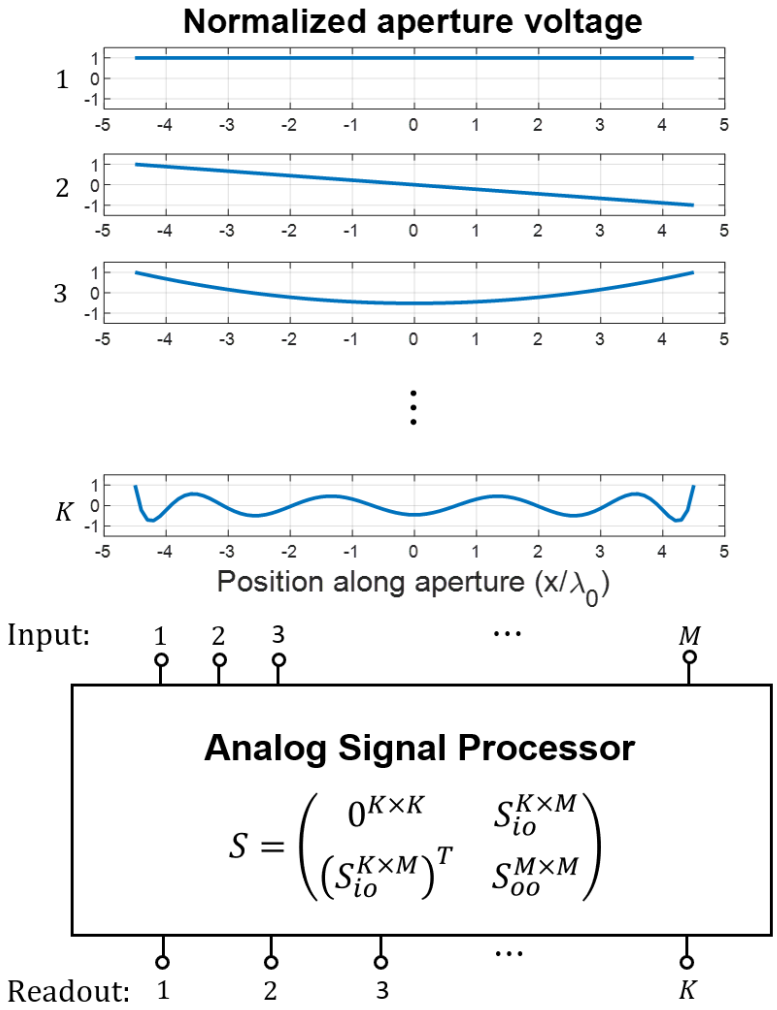

Figure 3.11: A depiction of the analog signal processor that performs aperture field decomposition. It has K readout ports and M input ports that can interface with an aperture antenna. The upper left block of the analog signal processor's S-matrix is $0^{K\text{x}K}$ indicating that its input ports are impedance matched and decoupled. The block $S_{io}^{K\text{x}M}$ performs the inner product of the aperture field with each of the aperture basis functions, and produces the weighting coefficients at each of the readout ports. The elements of $S_{oo}^{M\text{x}M}$ are free variables, and are neglected in the design.

3.3.2 Analog Signal Processor

In this section, an analog signal processor is designed to demonstrate the design method's ability to realize a variety of aperture fields. The analog signal processor samples an incident aperture field at its input ports and decomposes it into a set of aperture basis functions, and outputs the complex-valued weighting coefficient for each basis function, see Fig. 3.11. The coefficients are extracted from the network by observing the amplitude and phase of the voltage present at the readout port associated with each basis function. The extracted

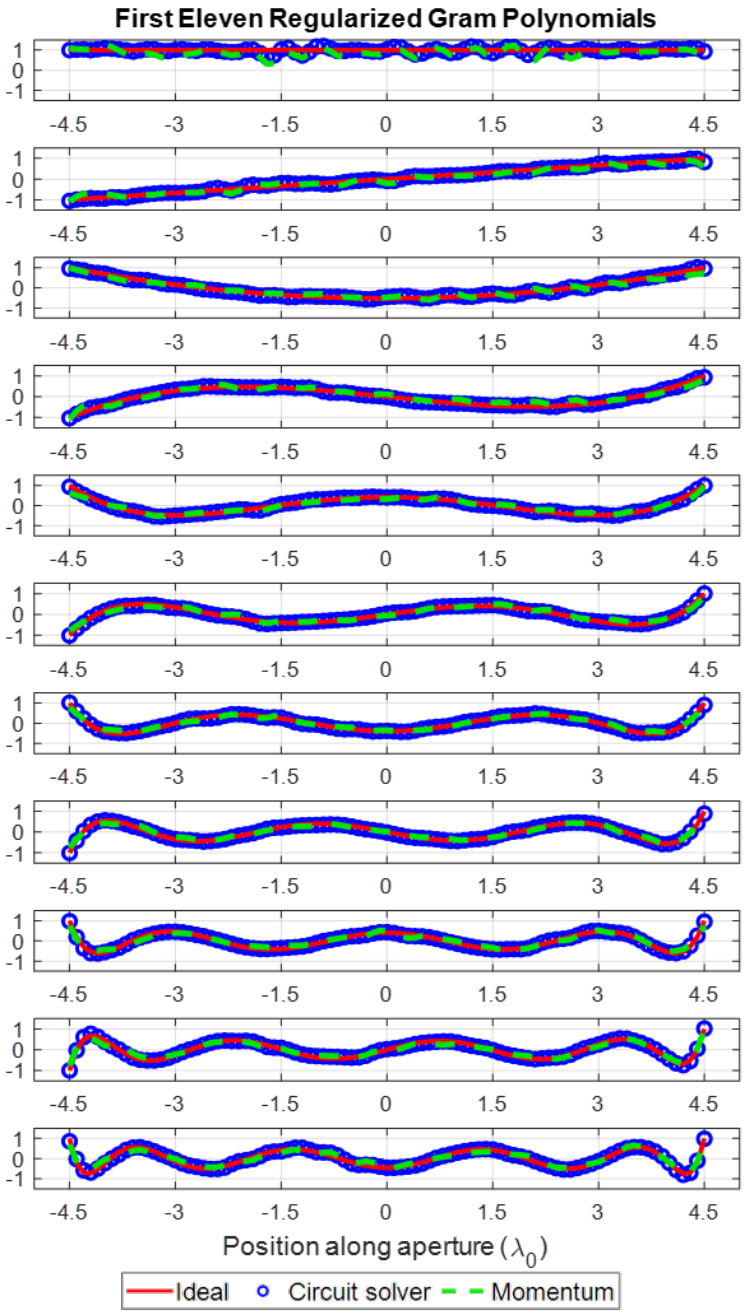

Figure 3.12: The eleven aperture basis functions (first eleven regularized Gram polynomials) used in the analog signal processor. The Gram polynomials have been normalized and plotted on a common scale. The solid red lines are the ideal Gram polynomials, the blue circles are the realized voltages using the circuit network solver, and the green dashed line are from the full wave simulation.

weighting coefficients can then be used to numerically reconstruct the aperture field using the known aperture basis functions.

The aperture basis functions used in this example are a set of discrete orthogonal poly-

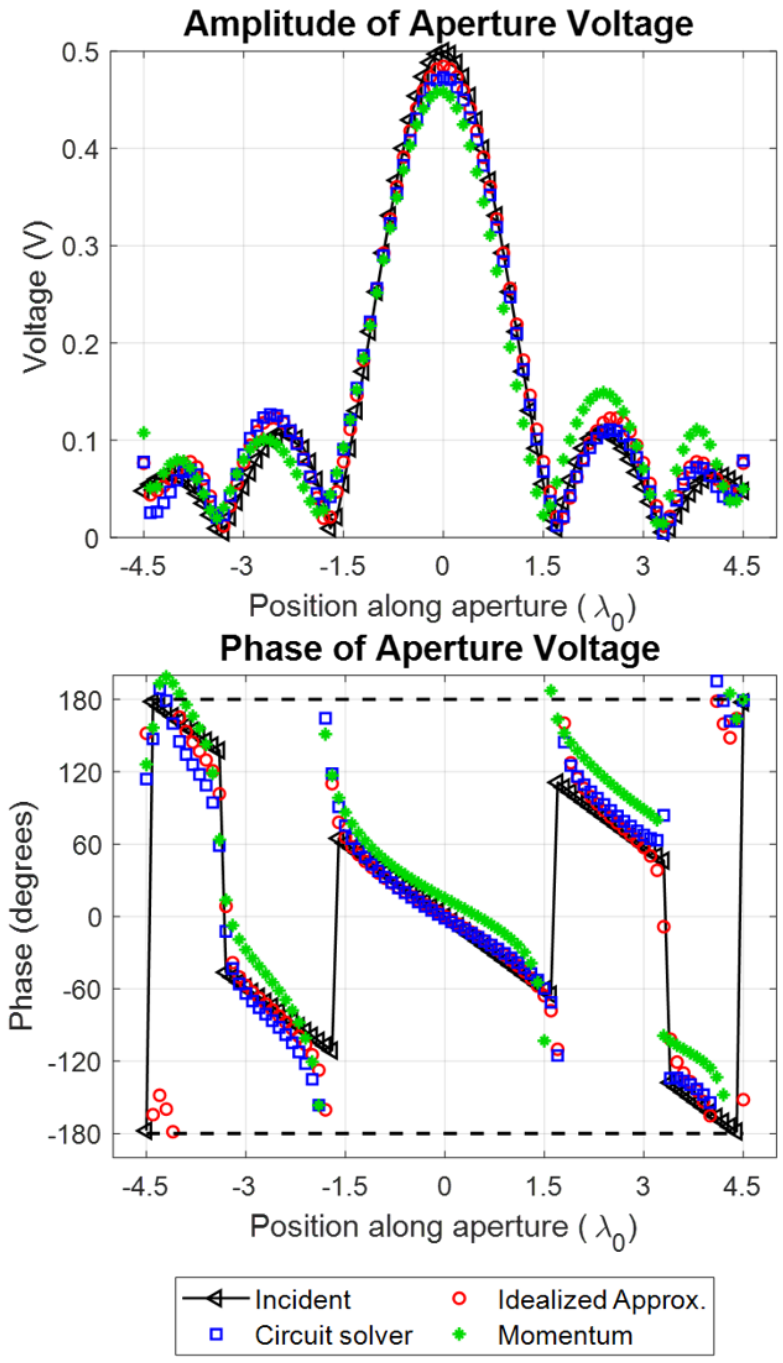

Figure 3.13: Comparison of the incident field profile to its approximation using the first eleven Gram polynomials with the idealized weighting coefficients and the weighting coefficients from the planar microstrip network (metastructure) computed using the circuit network solver and from the full-wave simulation. The incident aperture field is given by (3.18).

nomials with equal Euclidean norm (ensures conservation of power). Specifically, the basis

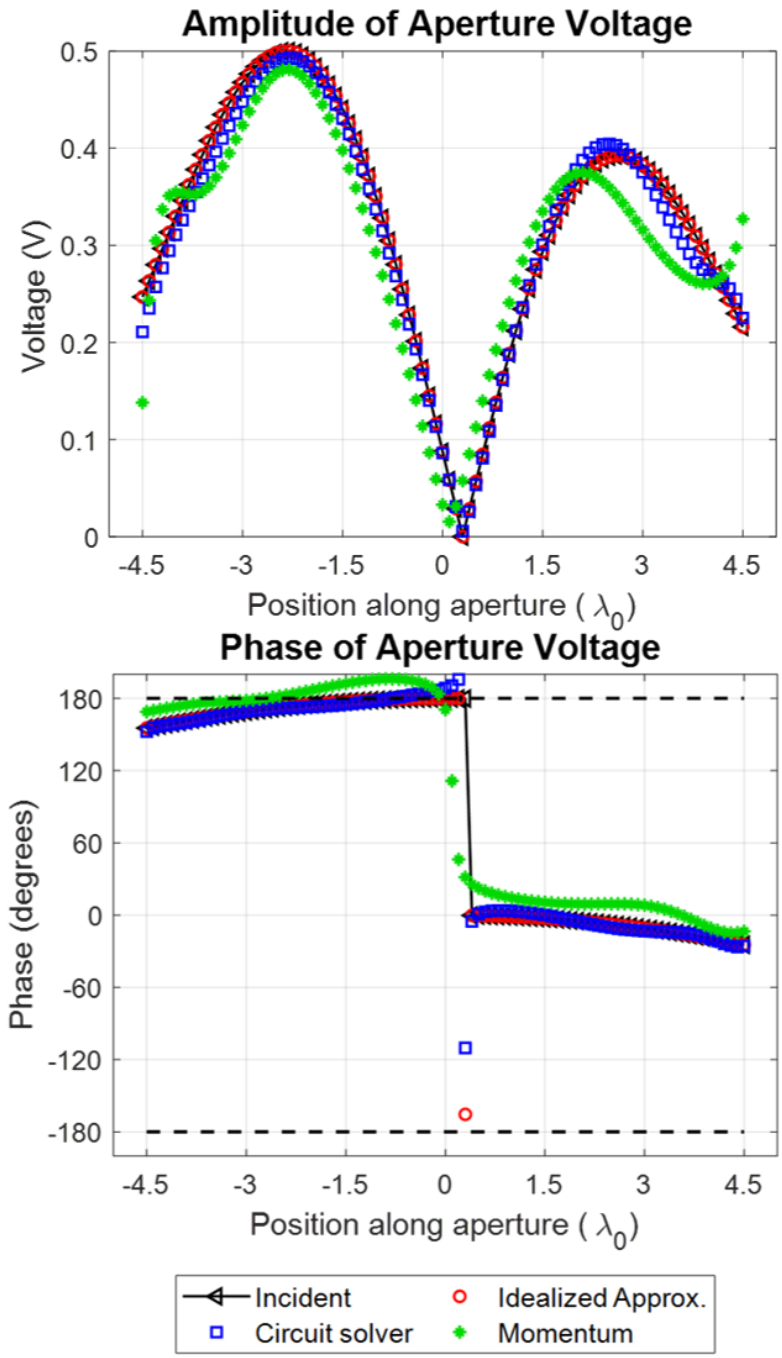

Figure 3.14: Comparison of the incident field profile to its approximation using the first eleven Gram polynomials with the idealized weighting coefficients and the weighting coefficients from the planar microstrip network (metastructure) using the circuit network solver and from the full-wave simulation. The incident aperture field is given by (3.19).

functions are a regularized version of the first eleven Gram or discrete Chebyshev polynomials. The Gram polynomials are selected since they are close approximations to the

minimax polynomials used for approximating functions with finite sets of polynomials. The aperture basis functions are produced using the Discrete Orthogonal Polynomial toolbox in MATLAB [80], and are depicted in Fig. 3.12. Here, eleven basis functions are used, and it is demonstrated that eleven basis functions are sufficient to approximate some non-trivial aperture fields. However, if more accuracy is needed for highly oscillatory or aperture fields with discontinuities additional basis functions can be included by making the network larger or adjusting the spacings between the readout ports.

3.3.2.1 Design Specifications

The analog signal processor is implemented as a planar microstrip network. It can interface with an aperture antenna that operates at 10 GHz and has a width of $W_{ap} = 9.1\lambda_0 = 27.3$ cm. The network has the same width as the antenna aperture and has a depth of $h = 3\lambda_0 = 9$ cm. The microstrip unit cell shown in Fig. 3.5 is used to design the network. The unit cell size is $d = \lambda_0/10 = 3$ mm, and the corresponding grid has the following dimensions, $N = 91$ and $M = 30$. Each of the eleven aperture basis functions are assigned to a $50\ \Omega$ readout port. The readout ports are located along the input plane, shown in Fig. 3.1, and are spaced by $0.7\lambda_0$, starting from the center line of the device. To ensure that each aperture basis function is associated with one readout port, all of the readout ports are required to be isolated from each other. The aperture field input ports, which interface with the aperture antenna, are located along the output plane, shown in Fig. 3.1. Similar to the beamformer example, the aperture antenna's input ports have an input impedance of $140\ \Omega$ at broadside so, the aperture field input ports are matched to $140\ \Omega$ for each basis function. All of the remaining ports besides the readout and aperture field input ports are open-circuited during the design process.

3.3.2.2 Optimization and Results

To design the network, the optimization routine is provided with the desired inputs (aperture basis functions) and readout voltages (single port excitations), the unit cell model, the terminations, and a initial set of 16,380 design variables. The design process took approximately 10 hours on a personal computer (i7-9700 CPU @ 3GHz w/8 cores with 64GB RAM) to produce a satisfactory design. The designed network's aperture basis functions are shown in Fig. 3.12. Excellent agreement between the desired and realized aperture basis functions is observed. The readouts are well matched with a maximum reflectance of -19.2 dB for the seventh polynomial's readout port. The worst case isolation between the readout ports is 28.8 dB, occurring between the readout port for the first polynomial and

the readout port for the fifth polynomial.

Two different incident aperture fields are used to test the analog signal processor's ability to decompose an incident field. The first aperture field is given by,

$$V_{ap}(x) = 0.5\,\mathrm{sinc}(20x)e^{-jk_0\sin(\pi/6)x}\ \ V \tag{3.18}$$

and the second incident aperture field is given by,

$$V_{ap}(x) = 9.7\cos^5(\pi x/W_{ap})(x-0.009)e^{-j0.87k_0x^2} \tag{3.19}$$

where x is the position along the aperture in meters and k_0 is the free space wavenumber at 10 GHz. The network is tested by solving for the complex weighting coefficients produced by the network for each incident aperture field using the circuit network solver. This is done by terminating the readout ports in $50\ \Omega$ and the input ports in $140\ \Omega$, and exciting the input ports with either (3.18) or (3.19). The reconstructed fields are calculated in MATLAB using the complex weighting coefficients produced by the network and the ideal aperture basis functions, and are shown in Fig. 3.13 for (3.18) and Fig. 3.14 for (3.19). They are compared to the exact aperture fields as well, as idealized approximations of the aperture field. The weighting coefficients for the idealized approximation are computed by taking the inner product of the incident field with the first eleven Gram polynomials. The amplitude and phase of the reconstructed aperture fields show good agreement in both cases. The largest errors between the reconstructed and the exact amplitude and phase profiles occur near discontinuities or where the derivative changes sign. In these regions the reconstructed and idealized approximations of the aperture field show good agreement. Indicating that these errors are largely due to the number of basis functions used rather than issues with the design itself.

For full-wave verification of the analog signal processor's performance, it is simulated in Keysight Momentum. The full-wave simulation took ~ 250 hours to complete and the results for the aperture basis functions are shown in Fig. 3.12. Some variations in the aperture basis functions are observed but, overall the performance matches the circuit network solver quite well. The readouts are well matched with a maximum reflectance of -12.7 dB for the fifth polynomial's readout port. The worst case isolation between the readout ports is 22 dB, occurring between the readout port for the fourth polynomial and the readout port for the sixth polynomial. The full-wave solution for the device's scattering matrix is then used to reconstruct the aperture fields given by (3.18) and (3.19) and the results are shown in Fig. 3.13 and Fig. 3.14, respectively. Again the results match quite well but, some errors are observed due to the errors in the aperture basis functions. The

largest error is seen in the reconstructed amplitude of (3.14) around the position $2\lambda_0$. This is largely due to errors present in the full-wave results for the fourth aperture basis function around this position since, (3.19) has a significant component along this basis function.

3.4 Summary

In this paper, an inverse-design procedure for multi-input multi-output (MIMO) metastructured devices was provided. The design procedure uses a fast 2-D circuit network solver in conjunction with a gradient-based optimization routine to produce devices with desired MIMO functions. Since the gradient must be calculated at every step of the optimization routine, and metastructures have a large number of design variables, the adjoint variable method is used to calculate the gradient. The computational efficiency gained by using the fast 2-D circuit-based solver and the adjoint variable method enables the design procedure to realize electrically large aperiodic MIMO metastructures.

The efficacy of the design procedure was then demonstrated through the design of a planar antenna beamformer and an analog signal processor for aperture field decomposition. The beamformer supports the simultaneous excitation of nine beams, contains approximately 6000 design variables, and took approximately six hours to design. The analog signal processor uses eleven orthogonal aperture basis functions to decompose incident field profiles. It contains approximately 16,400 design variables and took approximately 10 hours to design. Both of the devices were implemented in microstrip technology and their performances were verified using the Keysight method of moments solver Momentum.

CHAPTER 4

Experimental Realization of a Multi-beam Antenna

4.1 Introduction

In this chapter, the focus is on using the computational inverse design procedure introduced in the previous chapter to design a particular type of MIMO metastructure: a metastructured antenna beamformer. The inverse design procedure provided in Chapter 3 is used over other design procedures, like those provided in [11, 15, 16, 48, 52], because it is better suited to the design of guided-wave devices that are electrically large, contain many subwavelength features, and possess a large number of design variables. It performs well on these types of problems because it circumvents full-wave simulations during the optimization process through the use of a circuit network solver, and utilizes the adjoint variable method to efficiently calculate gradients.

To understand the potential benefits of using MIMO metastructures over more conventional methods for beamforming such as Rotman lenses, planar Luneburg lenses, or Butler matrices consider the following comparisons. Note that the following comparisons assume that the beamformers are implemented on microwave substrates, with $\epsilon_r < 3$, and are used to feed an antenna that is $8\lambda_0$ wide. Rotman lenses provide broadband performance but they have curved interfaces and are relatively large in both their transverse and longitudinal dimensions ($4 - 8\lambda_0$). Additionally, they provide a maximum of three perfectly phased aperture fields and have no control over the aperture field's amplitude [72]. Planar Luneburg lenses are also broadband and produce identical aperture fields for all scan angles but, again there is no control over the amplitude pattern [81]. They also possess curved interfaces and are quite large with a diameter of at least $8\lambda_0$. An alternative to quasi-optical beamformers are Butler matrices which, can theoretically produce an arbitrary number of perfectly phased aperture fields [75]. However, Butler matrices are typically narrowband,

lossy, and have limited control over the amplitude of the aperture fields. They are also relatively large with a depth greater than $4\lambda_0$. The advantage of using MIMO metastructures is that they can provide amplitude and phase control for all output fields, have planar interfaces which may be easier to integrate into various platforms, reduce the overall size of the beamforming region and have the potential to operate over wide bandwidths as demonstrated in [11].

This work reports the experimental realization of a metastructured beamformer that has been integrated with a 3D printed aperture antenna. The metastructured beamformer is designed using the computational inverse design procedure proposed in [53], which is briefly reviewed and then applied. Measurements of the antenna's radiation patterns, return loss, and isolation demonstrate that the proposed design method can be used to design practical devices.

4.2 Design approach

The antenna beamformer for the multi-beam antenna system, shown in Fig. 4.2, is designed using the computational inverse design procedure for MIMO metastructures provided in [53]. The main advantage of this design procedure is its computational efficiency, which enables the rapid synthesis of electrically large devices with multiple functionalities. This is achieved by avoiding full-wave simulations during run-time by using a 2-D circuit network solver, and the adjoint variable method to evaluate gradients in the quasi-newton optimization procedure. This section contains a brief review of the design procedure for the details refer to [53].

4.2.1 2-D Circuit Network Solver

Designing metastructures through computational inverse design requires the selection of a forward problem solver to evaluate device responses. To make the design of electrically large MIMO devices tractable, the forward problem solver should be able to evaluate device responses quickly and accurately. Full-wave solvers provide a high level of accuracy but when devices are electrically large and contain many subwavelength features, which is common in metastructured devices, they consume significant computational resources and are prohibitively slow. Therefore, it is desirable to avoid the use of full-wave solutions during the optimization process, if possible. For 2-D metastructures supporting guided waves, this can be achieved by representing the device as a 2-D circuit network composed of four-port admittance matrices (representing the unit cells) tiled in the x-z plane, as shown

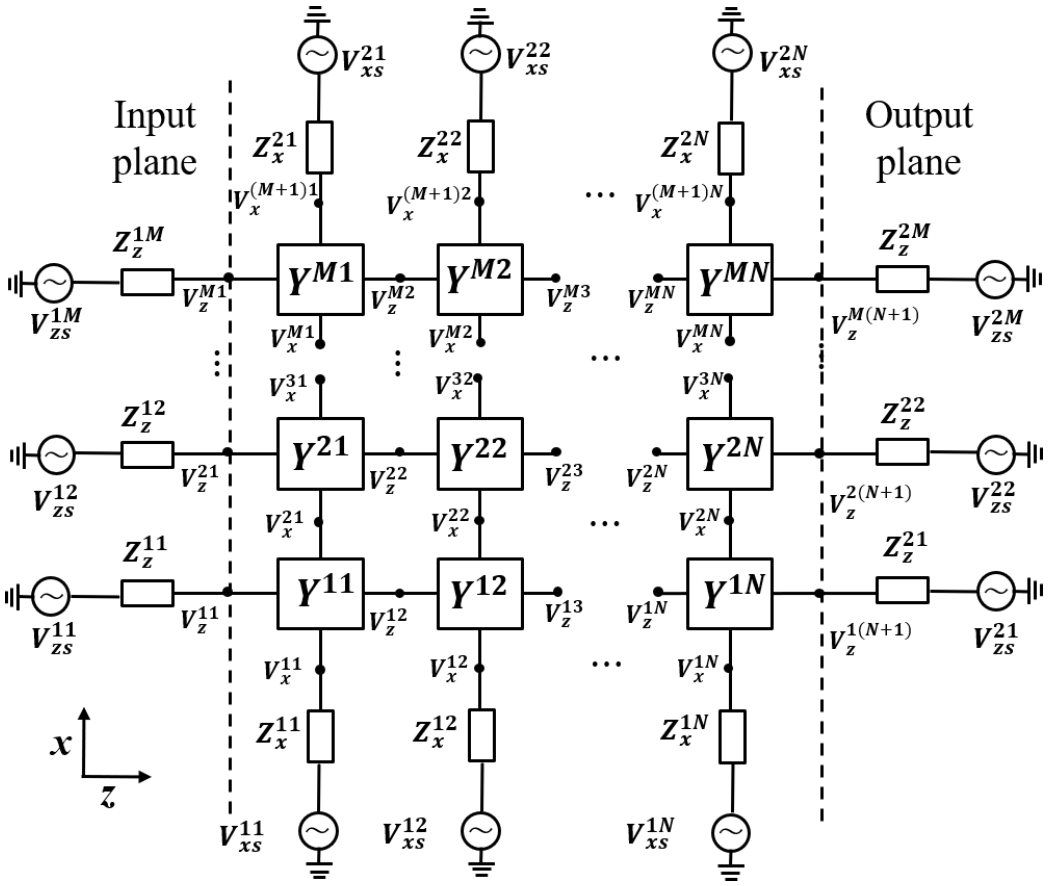

Figure 4.1: A metastructure consisting of an MxN grid of four-port admittance matrices. The admittance matrices represent the metastructure's unit cells. Lumped impedances and voltages along the boundaries are used to excite the metastructure and produce the desired boundary conditions.

in Fig. 4.1. By representing the problem in this way, macroscale or device level effects are accounted for by modeling the interactions between neighboring unit cells using circuit theory, and microscale or unit cell level effects are accounted for by using a reduced-order model of the unit cell's admittance matrix. The accuracy of these models can be maintained by using full-wave simulations to generate the reduced-order models. Accuracy is then only limited by the number of accessible modes that are accounted for by the admittance matrices [69]. If all of the accessible modes at the ports of the unit cell are included in the model, then it is a perfect representation of the unit cell's response. However, if the unit cell supports a single propagating mode and all other modes are well below their cut-off frequency then a single guided mode can be used to obtain satisfactory results, as is shown here.

4.2.2 Optimization procedure

Here, the design of MIMO metastructures is posed as an optimization problem over the unit cell's characteristics (design variables). The design procedure starts with a set of excitations (inputs) and their desired responses (outputs). Since a circuit network solver is used, the excitations are specified as voltage distributions along the input plane and the desired responses are voltage distributions along the boundaries of the network, see Fig. 4.1. The inputs are referred to as $\{\mathbf{v}_{\text{in}}^k\}$ and the outputs as $\{\mathbf{v}_{\text{out}}^k\}$, where $k \in \{1, 2, 3, ..., K\}$ and K is the total number of input-output pairs. An "input-output pair" refers to an input voltage distribution and its associated output voltage distribution. The cost function is formed by defining a cost function $g_k(\mathbf{p})$ that captures the error in the output for each input-output pair,

$$g_k(\mathbf{p}) = \frac{1}{2}(\mathbf{v}^k(\mathbf{p}) - \mathbf{v}_{\text{out}}^k)^H \overline{\overline{G}}(\mathbf{v}^k(\mathbf{p}) - \mathbf{v}_{\text{out}}^k) \tag{4.1}$$

where $\mathbf{p}$ is a vector containing all of the design variables in the network, the vector $\mathbf{v}^k(\mathbf{p})$ contains the voltages in the network (subject to the design variables) when it is excited by $\mathbf{v}_{\text{in}}^k$, and the superscript H indicates the conjugate transpose. The matrix $\overline{\overline{G}}$ acts as a mask and is used to select and scale the elements of $\mathbf{v}^k(\mathbf{p}) - \mathbf{v}_{\text{out}}^k$. The total cost function is then formed by summing over all of the input-output pairs as follows,

$$g(\mathbf{p}) = \sum_{k=1}^{K} g_k(\mathbf{p}). \tag{4.2}$$

Using (4.2) the following optimization problem can be defined to design MIMO devices,

$$\begin{aligned} &\arg\min_{\mathbf{p}} g(\mathbf{p}) \\ &\text{subject to :} \quad \mathbf{p}_{\text{lb}} \preceq \mathbf{p} \preceq \mathbf{p}_{\text{ub}} \end{aligned} \tag{4.3}$$

where $\mathbf{p}_{\text{lb}}$ and $\mathbf{p}_{\text{ub}}$ are vectors containing the lower and upper bounds of the design variables, respectively. To solve (4.3) a quasi-newton optimization routine is employed that uses the adjoint variable method to calculate the gradient. Further details regarding the optimization procedure are provided in Chapter 3.

4.3 Multi-beam Antenna Design

In this section, a multi-beam antenna system that produces nine switched beams and operates at 10 GHz is designed. The multi-beam antenna system consists of a printed-

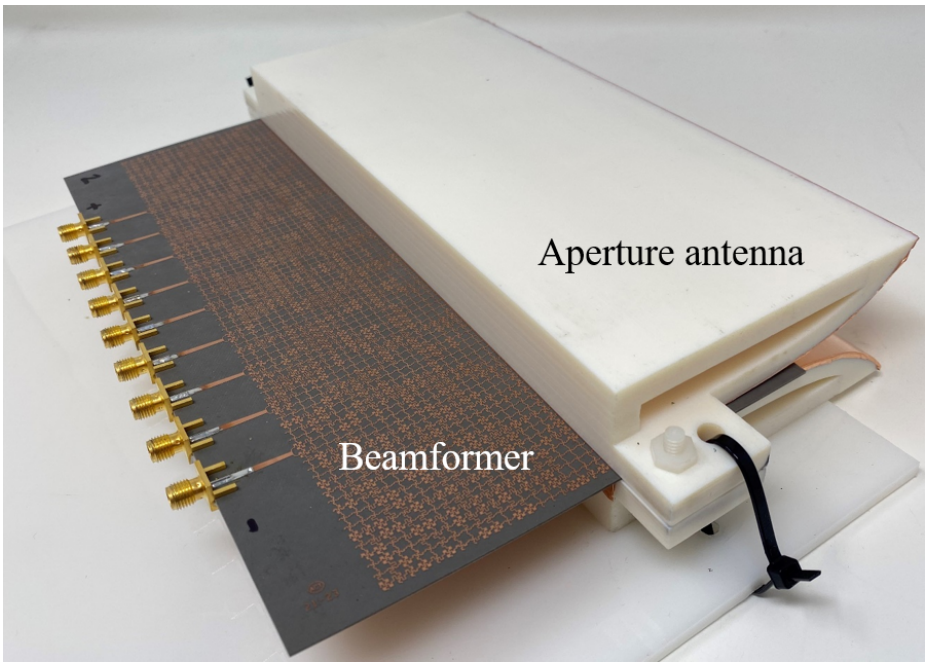

Figure 4.2: A picture of the multi-beam antenna system. It is composed of a printed-circuit beamformer and a 3D printed aperture antenna.

circuit beamformer that is integrated with a 3-D printed aperture antenna. The printed-circuit beamformer is designed using a TL unit cell in the design procedure outlined in Section II. A TL unit cell is selected because it provides a wideband response and is planar, compact, low-cost, and amenable to printed-circuit processes. The aperture antenna is then designed to be integrated with the beamformer and provides broadband impedance matching for all nine excitations.

4.3.1 Microstrip Beamformer Design

4.3.1.1 Positive Refraction Beamformer

The printed-circuit beamformer is designed to feed an aperture antenna, designed in Section III B (see Fig. 4.2), and is patterned on a Roger's RT/Duroid RO5880 substrate, $\epsilon_r = 2.2$ and $\tan\delta = 0.0009$, with a substrate thickness of $h = 0.787$ mm and a copper thickness of 35 μm. The width of the beamformer is chosen to match the width of the antenna's input aperture, i.e. $W = 24$ cm $(8\lambda_0)$, and the depth of the beamformer is chosen to be $D = 6$ cm $(2\lambda_0)$. This depth is chosen to minimize the size of the beamforming network while allowing for the power distribution at the aperture to be shaped without utilizing cavity effects from the edges of the beamformer.

Since the design procedure outlined in Section II is used, the following steps are re-

quired to properly define the problem: (1) the beamforming region must be discretized, (2) a unit cell topology must be selected, (3) a model of the unit cell needs to be developed, (4) the design goals need to be stated in terms of an output voltage profile for each input. First, the beamforming region is discretized into square unit cells with a side length of $d = 3$ mm $(\lambda_0/10)$. This discretization corresponds to a grid of unit cells modeled with admittance matrices, see Fig. 4.1. The grid has 80 unit cells in the x-direction ($M = 80$) and 20 unit cells in the z-direction ($N = 20$). Next, the microstrip unit cell topology, shown in Fig. 4.3, is selected. The unit cell has six degrees of freedom: two TL widths and four TL lengths. The variable width lines are allowed to vary from 0.2 mm to 0.8 mm and have a length of 0.875 mm. The variable length lines have a width of $w_0 = 0.25$ mm and their lengths are allowed to vary from 0 to $l_i^{\max}$. The variable $l_i^{\max} = d/2 - w_0/2 - W_j$ and W_j corresponds to the variable width line connected to l_i for $i \in \{1, 2, 3, 4\}$. This is the same unit cell used in [53]. It was chosen to balance the unit cell's complexity with the number of degrees of freedom, as well as the variables' ability to control the unit cell's admittance parameters. To create a differentiable model of the unit cell a database of $15,625$ unit cells were simulated in the commercial method of moments solver Keysight Momentum. For these simulations, the substrate and conductors were assumed to be lossless, and the conductors had no thickness or surface roughness. The database of simulated admittance parameters were then spline interpolated to generate a model of the unit cell for use in the design procedure, for the details see Chapter 3.

To state the design goals in terms of output voltage profiles along the boundaries of the grid, the desired characteristics of the beamformer need to be specified. The beamformer is designed to operate at 10 GHz and produce nine beams that are excited by nine different $50\ \Omega$ input ports. The input ports are impedance matched and isolated from each other to allow for the beams to be simultaneously excited. During the design process the beamformer is assumed to be lossless which, combined with the condition of isolated input ports, requires the antenna's radiation patterns to be mutually orthogonal [77]. For this reason, the radiation patterns are chosen to be sinc functions with beampointing directions corresponding to the following tangential wave numbers,

$$k_n = \frac{2\pi n}{Md}, \quad n \in \{0, \pm 1, \pm 2, \pm 3, \pm 4\}. \tag{4.4}$$

In (4.4), d is the physical spacing between the beamformer output ports, and M is the number of output ports. For M and d in this design, the wavenumbers given by (4.4) correspond to the following beampointing directions: $\theta_B = 0°, \pm 7.18°, \pm 14.48°, \pm 22.02°, \pm 30°$. The aperture fields corresponding to these radiation patterns are uniform amplitude with linear

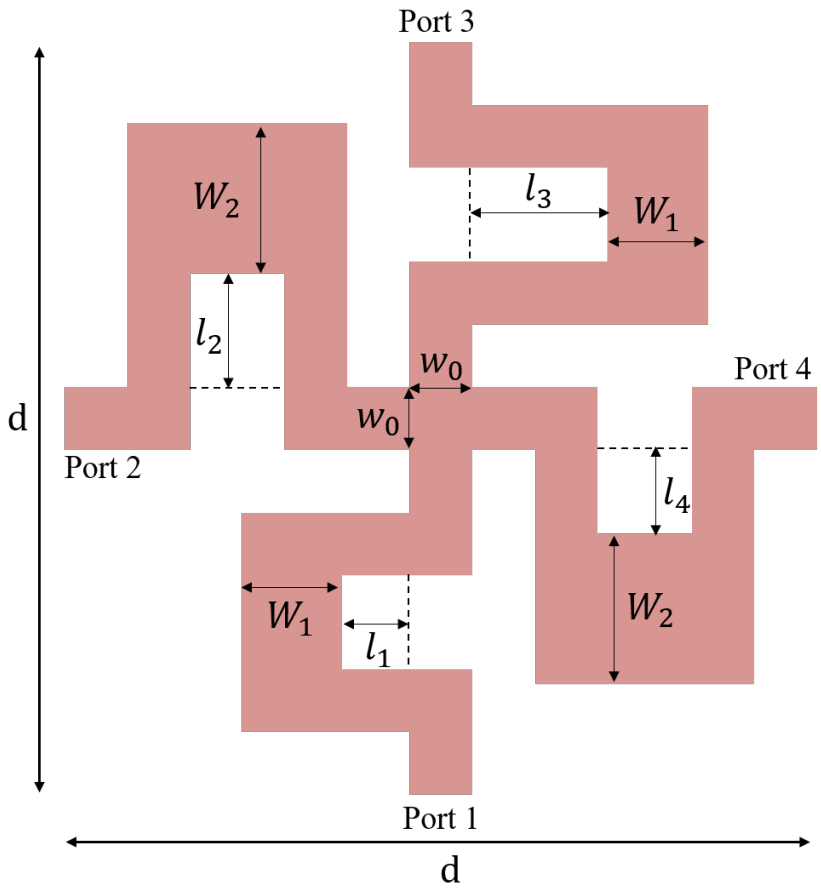

Figure 4.3: Example of a microstrip unit cell used to design the metastructured beamformer. The unit cell is parameterized using six design variables: W_1, W_2, l_1, l_2, l_3, and l_4. The microstrip lines all have a width of $w_0 = 0.25$ mm except for the lines with widths W_1 or W_2.

phase gradients given by (4.4). These aperture fields are the target output voltage profiles along the output plane of the beamformer, shown in Fig. 4.1. To ensure that the input ports are isolated and reduce reflections from the edges of the beamformer the desired output voltages at the remaining nodes along the boundary of the beamformer, besides those corresponding to the active input port, are set to zero. The voltages at the nodes corresponding to the active input port are used to ensure impedance matching. Since the nodes are terminated by a matched impedance and excited by a voltage V_n, the desired output voltage is $V_n/2$ to ensure that the port is impedance matched.

The two remaining considerations before designing the beamformer are determining how to excite the beamforming region and how to terminate the grid of admittance matrices. The beamforming region will be excited along the input plane by exciting pairs of nodes starting from the center line of the beamformer. Each of the pairs is separated by 1.2 cm,

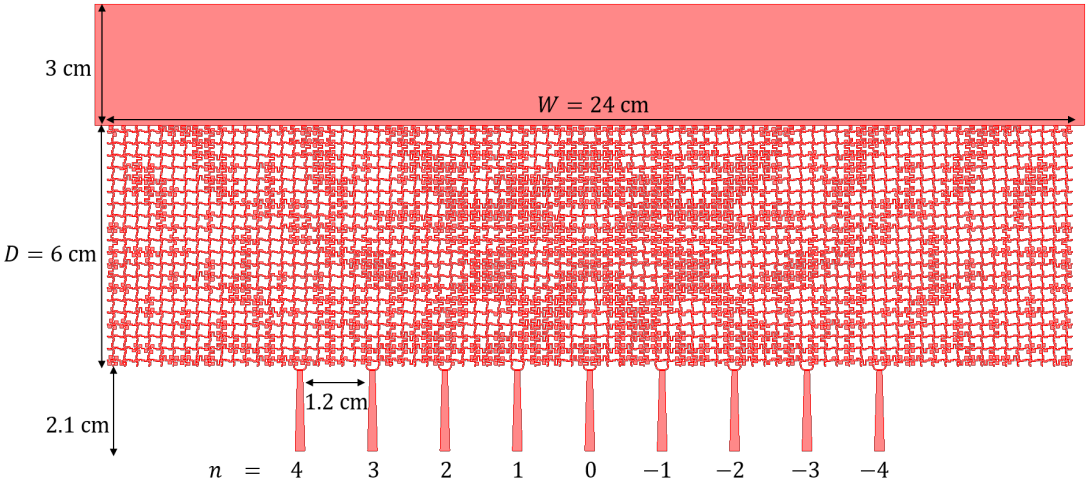

Figure 4.4: The layout of the positive refraction metastructured beamformer. The beamformer is fed by nine input ports and is terminated in a parallel-plate waveguide. The beamformer's input ports are labeled $n = 0, \pm 1, \pm 2, \pm 3, \pm 4$ which, produce aperture fields with phase gradients that correspond to transverse wavenumbers given by (4.4).

see Fig. 4.4. Exciting pairs of nodes serves two purposes: (1) it maintains symmetry in the beamformer (2) it makes impedance matching the microstrip lines with width w_0 ($Z_0 \approx 147\ \Omega$) at the unit cell's ports to $50\ \Omega$ easier. It makes impedance matching easier because it reduces the input impedance of the combined lines to $73.5\ \Omega$. Practically, the ports are combined by terminating the grid in microstrip lines with $Z_0 = 147\ \Omega$ and then using a T-junction to combine them in parallel, as shown in Fig. 4.4. Each pair of lines is then impedance matched to $50\ \Omega$ using a tapered-impedance microstrip line with a length of 2 cm. Therefore, in the circuit network solver, the input ports are terminated by $147\ \Omega$ lumped impedances.

The output plane of the admittance matrix grid should be impedance matched to the parallel-plate waveguide that the beamformer is terminated in. Since each of the output ports excite a section of the parallel-plate waveguide that is $d = 3$ mm wide, the output terminations correspond to the following TE wave impedances for each of the beampointing directions θ_B,

$$Z_{out} = \frac{\eta_0}{\sqrt{\epsilon_r}\cos\theta_B}\frac{h}{d} = \frac{66.7\ \Omega}{\cos\theta_B}, \tag{4.5}$$

where η_0 is the free-space wave impedance and ϵ_r is the dielectric constant of the substrate. The terminations for the remaining ports along the input plane and the sides of the beamformer are assumed to be open-circuits. Combined with the target of zero voltage at these nodes allows the cost function to select designs with lower reflections from the edges of the beamformer.

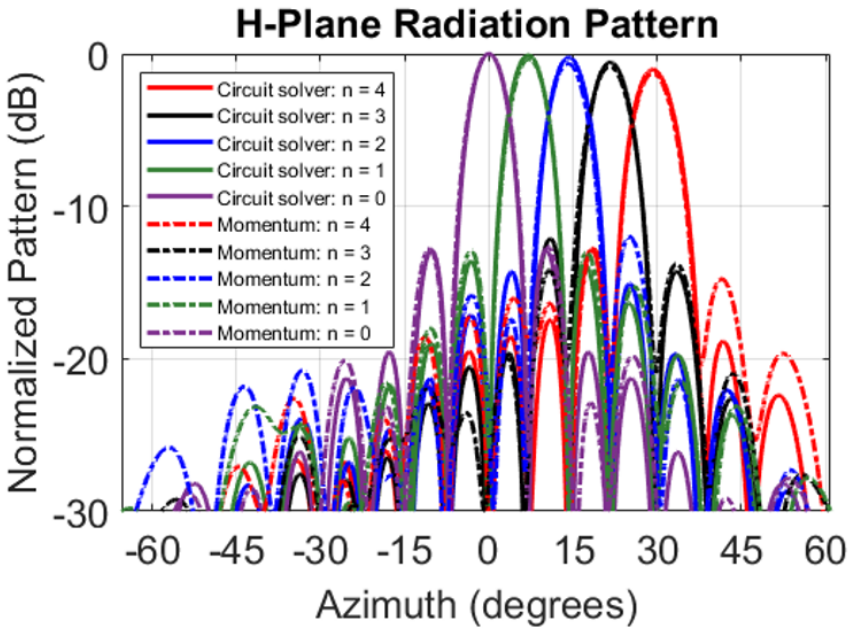

Figure 4.5: The analytically calculated co-polarized H-plane radiation patterns produced by an aperture antenna fed by the metastructured beamformer. The solid lines are calculated using the simulated voltages from the circuit network solver. The dot-dashed lines are calculated using the simulated voltages from the full-wave (Momentum) simulation. For clarity only the positive scan angles are shown. The negative scan angles are identical due to symmetry.

With the design goals and terminations defined, the beamforming region can now be designed. However, before designing the beamformer, symmetries can be exploited to reduce the number of variables and improve convergence. Symmetry of the aperture fields and excitations across the center line of the metastructure allows for the number of design variables to be reduced from 9600 to 4800. This is achieved by mirroring the admittance matrices across the center line. After enforcing symmetry in the circuit network solver, the beamformer is designed by providing the optimization routine with the unit cell model, the excitations (input voltage profiles) and desired outputs (output voltage profiles), along with a seed of uniform lengths and widths for the design variables. The algorithm was run on a personal computer with an i7-9700 CPU @ 3 GHz w/8 cores and 64 GB of RAM, and was set to terminate after 400 iterations. After approximately 5.5 hours of execution the design shown in Fig. 4.4 was produced. The design has a minimum return loss of 26.4 dB for ports $n = \pm 4$, a minimum isolation of 21 dB between ports $n = \pm 2$ and $n = \pm 3$, and produces the radiation patterns shown in Fig. 4.5. These radiation patterns are calculated analytically assuming the aperture field is piece-wise uniform in amplitude and phase.

To verify the performance of the beamformer, a full-wave simulation was performed

in the commercial electromagnetics solver Keysight Momentum. As in the unit cell simulations, the substrate and conductors were assumed to be lossless, and the conductors had no thickness or surface roughness. It took approximately 94 hours to complete on a high-performance computing cluster with access to 15 cores and 600 GB of RAM. The full-wave results show good agreement, showing only a slight degradation in performance. The minimum return loss is 19.1 dB for ports $n = \pm 1$, the minimum isolation is 18.3 dB between ports $n = -2$ and $n = 2$, and the voltages at the output of the beamformer produce the radiation patterns shown in Fig. 4.5. Again, these radiation patterns are calculated analytically assuming the aperture field is piece-wise uniform in amplitude and phase. Overall, the performance is in good agreement with that predicted by the circuit network solver.

4.3.1.2 Negative Refraction Beamformer

To demonstrate that a metastructured beamformer has the ability to produce extreme phase transformations a beamformer that exhibits behavior analogous to negative refraction is designed. Again, the beamformer will be patterned on a Roger's RT/Duroid RO5880 substrate, $\epsilon_r = 2.2$ and $\tan\delta = 0.0009$, with a substrate thickness of $h = 0.787$ mm and a copper thickness of 35 μm; and, the same unit cell from the previous section is used again, see Fig. 4.3. The width of the beamformer is chosen to match the width of the antenna's input aperture, i.e. $W = 24$ cm $(8\lambda_0)$, and the depth of the beamformer is chosen to be the same as the positive refraction design, $D = 6$ cm $(2\lambda_0)$.

The beamformer is designed to operate at 10 GHz and produce nine beams that are excited by nine different 50 Ω input ports. The input ports are impedance matched and isolated from each other to allow for the beams to be simultaneously excited. During the design process the beamformer is assumed to be lossless. As a result, the radiation patterns must be orthogonal and the radiation patterns are chosen to be sinc functions with beampointing directions corresponding to the following tangential wave numbers,

$$k_n = -\frac{2\pi n}{Md}, \quad n \in \{0, \pm 1, \pm 2, \pm 3, \pm 4\}. \tag{4.6}$$

In (4.4), d is the physical spacing between the beamformer output ports, and M is the number of output ports. For M and d in this design, the wavenumbers given by (4.4) correspond to the following beampointing directions: $\theta_B = 0^\circ, \mp 7.18^\circ, \mp 14.48^\circ, \mp 22.02^\circ, \mp 30^\circ$. The aperture fields corresponding to these radiation patterns are uniform amplitude with linear phase gradients given by (4.6) which, are the negative of the positive refraction example. These aperture fields are the target output voltage profiles along the output plane of the beamformer, shown in Fig. 4.1. The target voltages along the input plane and edges of the

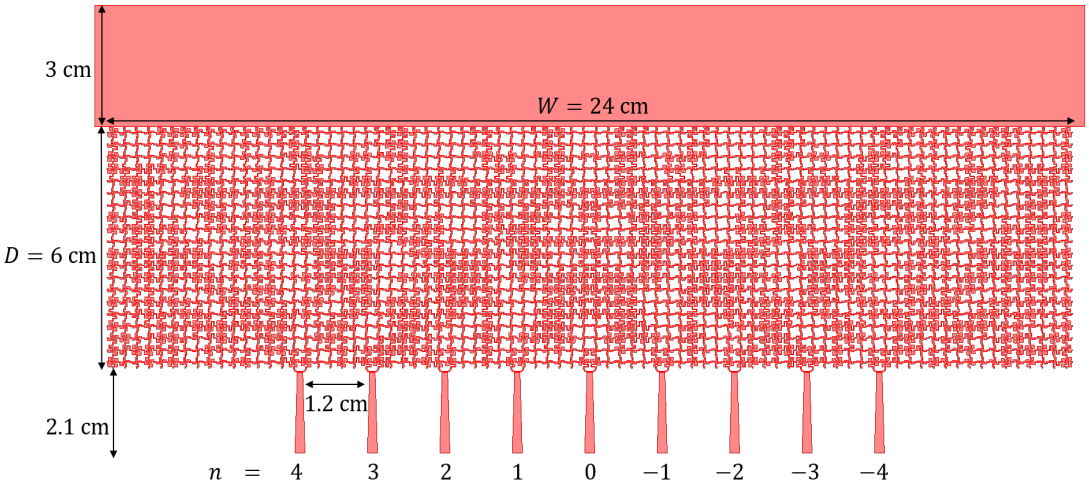

Figure 4.6: The layout of the negative refraction metastructured beamformer. The beamformer is fed by nine input ports and is terminated in a parallel-plate waveguide. The beamformer's input ports are labeled $n = 0, \pm1, \pm2, \pm3, \pm4$ which, produce aperture fields with phase gradients that correspond to transverse wavenumbers given by (4.4).

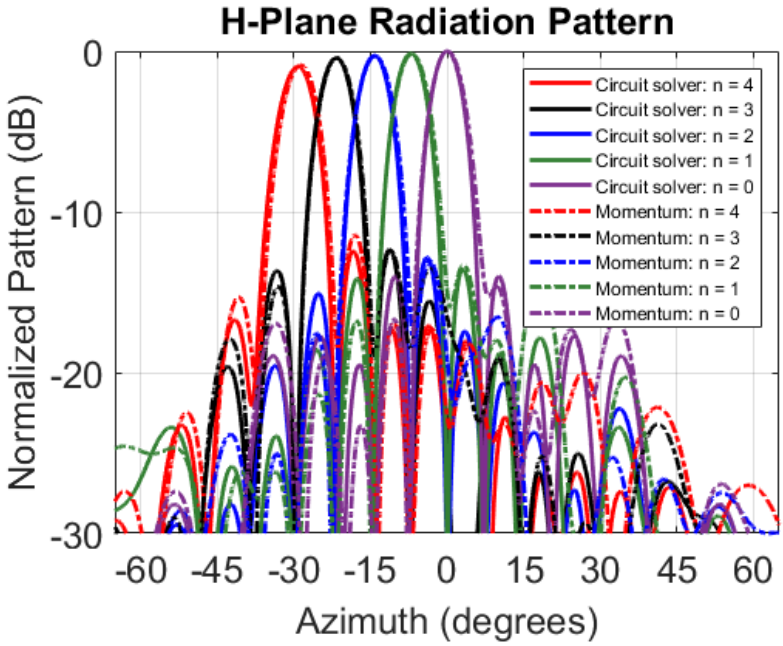

Figure 4.7: The analytically calculated co-polarized H-plane radiation patterns produced by an aperture antenna fed by the metastructured beamformer. The solid lines are calculated using the simulated voltages from the circuit network solver. The dot-dashed lines are calculated using the simulated voltages from the full-wave (Momentum) simulation. For clarity only the positive scan angles are shown. The negative scan angles are identical due to symmetry.

beamformer are the same as the positive refraction case.

The beamformer is designed for the same excitations and termination conditions as the positive refraction case, and symmetry is enforced to reduce the number of design variables from 9600 to 4800. The beamformer is then designed by providing the optimization routine with the unit cell model, the excitations (input voltage profiles) and desired outputs (output voltage profiles), along with a seed of uniform lengths and widths for the design variables. The algorithm was run on a personal computer with an i7-9700 CPU @ 3 GHz w/8 cores and 64 GB of RAM, and was set to terminate after 400 iterations. After approximately 5.2 hours of execution the design shown in Fig. 4.6 was produced. The design has a minimum return loss of 21.5 dB for ports $n = \pm 2$, a minimum isolation of 21.4 dB between ports $n = \pm 5$ and $n = \pm 4$, and produces the radiation patterns shown in Fig. 4.7. These radiation patterns are calculated analytically assuming the aperture field is piece-wise uniform in amplitude and phase.

To verify the performance of the beamformer, a full-wave simulation was performed in the commercial electromagnetics solver Keysight Momentum. As in the unit cell simulations, the substrate and conductors were assumed to be lossless, and the conductors had no thickness or surface roughness. It took approximately 94 hours to complete on a high-performance computing cluster with access to 15 cores and 600 GB of RAM. The full-wave results show good agreement, showing only a slight change in performance. The minimum return loss is 23.2 dB for ports $n = \pm 2$, the minimum isolation is 19.2 dB between ports $n = -1$ and $n = 1$, and the voltages at the output of the beamformer produce the radiation patterns shown in Fig. 4.7. Again, these radiation patterns are calculated analytically assuming the aperture field is piece-wise uniform in amplitude and phase. Overall, the performance is in good agreement with that predicted by the circuit network solver.

4.3.2 Antenna Design

The 3-D printed flared aperture antenna has a center frequency of 10 GHz and is designed to operate over a broad bandwidth. It is fed by a parallel-plate waveguide and transitions waves propagating in the TEM mode to radiated waves in free-space. The antenna interfaces with the printed-circuit beamformer designed in Section II A. Therefore, the parallel-plate waveguide feeding the antenna is a copper clad substrate. In this particular design, it is a 24 cm wide piece of a Roger's RT/Duroid RO5880 substrate, $\varepsilon_r = 2.2$ and $\tan\delta = 0.0009$, with a substrate thickness of $h = 0.787$ mm and a copper thickness of 35 μm. The antenna's input aperture has the same dimensions as the parallel-plate waveguide feed, i.e. $W_{\text{in}} = 24$ cm and $h_{\text{in}} = 0.787$ mm, and the aperture is tapered in the E-plane to the final dimensions $W_{\text{ap}} = 24$ cm and $h_{\text{ap}} = 5$ cm, see Fig. 4.8.

The antenna is impedance matched to the parallel-plate waveguide feed using an E-plane taper and a piece of substrate that is extended into the antenna's aperture, shown in Fig. 4.8. To allow for broadband impedance matching the height of the aperture is tapered exponentially from h_{in} to h_{ap} over a length of $L_{\text{taper}} = 7.5$ cm. To avoid an impedance mismatch at the junction between the dielectric-filled parallel-plate waveguide feed and the air-filled parallel-plate waveguide at the antenna's input, a piece of substrate with length $L_{\text{sub}} = 3$ cm is extended into the antenna. The substrate allows for the dielectric filling fraction within the antenna to be slowly tapered. This tapers the wave impedance and avoids large reflections at the interface. Alternatively, the height of the air-filled waveguide could have been reduced to $h_{\text{in}} = 0.53$ mm to match the impedance of the two waveguides. However, for ease of fabrication the former method for impedance matching was chosen.

The two lengths $L_{\text{taper}} = 7.5$ cm and $L_{\text{sub}} = 3$ cm were chosen by performing parametric sweeps in Ansys HFSS simulations. First, a 3 mm wide section of the antenna was simulated in a periodic environment and $L_{\text{sub}} = 3$ cm was swept to find the minimum length such that $|S_{11}|$ did not decrease with an increase in L_{sub}. Next, the same periodic simulation was ran and L_{taper} was swept until $|S_{11}|$ was less than -10 dB between 8 and 12 GHz for all scan angles.

The full antenna structure, shown in Fig. 4.8, was then simulated in Ansys HFSS to verify its performance. The antenna was then excited using the simulated output voltages of both beamformers for each scan angle, and the H-plane radiations patterns are shown in Fig. 4.9 for the positive refraction beamformer and Fig. 4.10. The antenna was manufactured with a Stratasys J750 Polyjet 3D printer using Verowhite material, and the tapered aperture was metalized using copper tape. A picture of the manufactured antenna is shown in Fig. 4.12.

4.4 Measurement Results

In this section, measurement results for the multi-beam antenna are reported. The multi-beam antenna was assembled by inserting the parallel-plate waveguide at the end of the patterned substrates into the aperture at the antenna's input. The antenna was then fastened to the beamformers with nylon screws, as shown in Fig. 4.11. In the following subsections, measurement results for the antenna's return loss, input isolation, and radiation patterns are provided when it is fed by the positive and negative refraction beamformers.

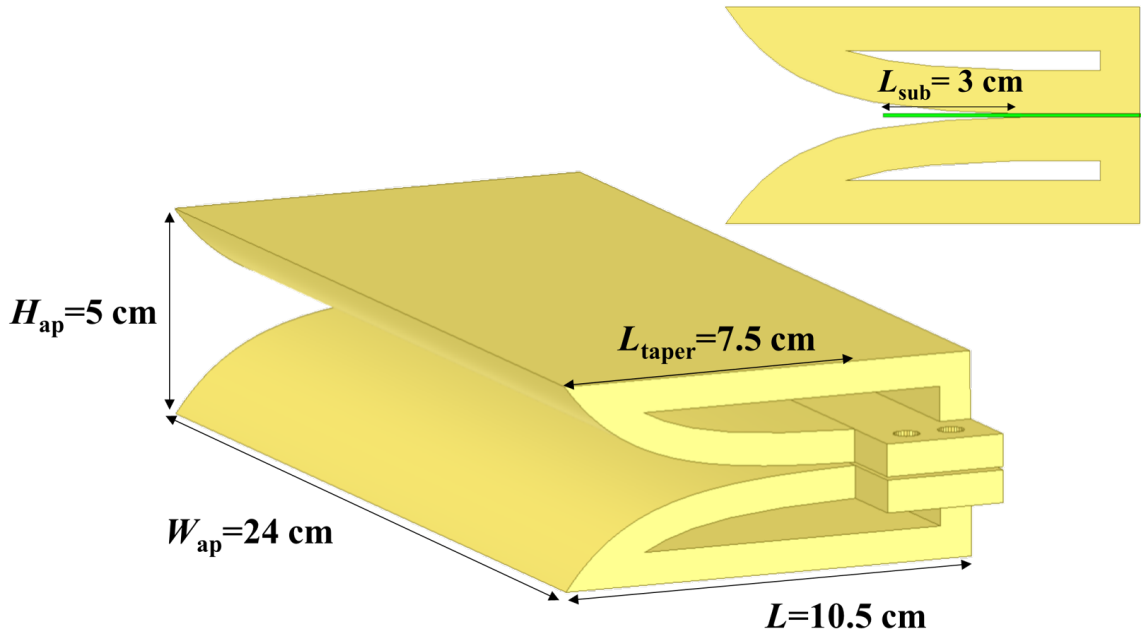

Figure 4.8: A rendering of the 3D printed aperture antenna and its dimensions. A depiction of the piece of substrate, with length L_{sub}, that is extended into the antenna's aperture for impedance matching is shown in the top right.

4.4.1 Impedance Match and Isolation

In this section, the following nomenclature for the ports is adopted. The ports are numbered from left to right such that port 1 corresponds to $n = 4$ and port 9 corresponds to $n = -4$. The performance of the input ports were measured using a Keysight E8361A PNA Network Analyzer. To characterize the return loss for each port S_{ii}, $i \in \{1, 2, ..., 9\}$, was measured from 8 to 12 GHz while terminating all other ports with broadband $50\ \Omega$ loads.

The results for all of the ports are shown in Fig. 4.13 for the positive refraction beamformer. A return loss greater than 10 dB was measured over a bandwidth of 1.5 GHz. Next, the port-to-port isolation was characterized from 8 to 12 GHz by connecting all possible pairs of ports one at a time and measuring S_{ij}, $i, j \in \{1, 2, ..., 9\}$, while the remaining ports were terminated in $50\ \Omega$ loads. By inspecting S_{ii} and S_{ij} for all of the ports, a frequency shift is observed in the beamformers performance. The frequency that maximizes the minimum return loss and isolation for all of the ports is 10.2 GHz. This indicates that the beamformer's operating frequency has shifted to 10.2 GHz. The values for the return loss and isolation at this frequency are reported in Table. 4.1 and Table. 4.3, respectively. Where a good impedance match and high isolation are observed for all of the antenna's input ports.

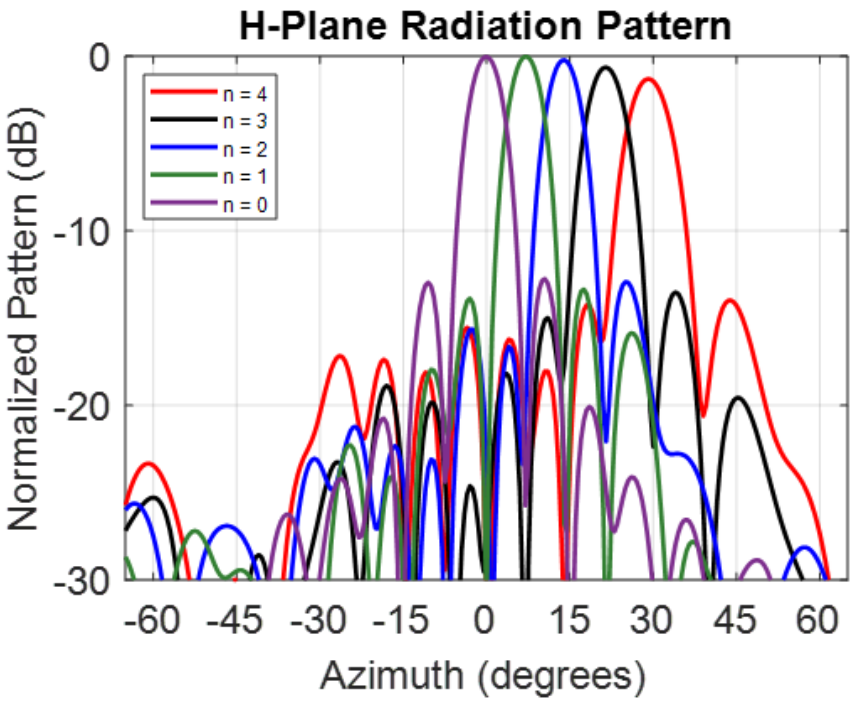

Figure 4.9: Full-wave simulation results of the co-polarized H-plane radiation patterns from the 3D printed aperture antenna. The plots are produced by exciting the simulated antenna (Ansys HFSS) with the output voltages from the full-wave simulation (Keysight Momentum) of the positive refraction metastructured beamformer. For clarity only the positive scan angles are shown. The negative scan angles are identical due to symmetry.

Port	Simulated (10 GHz)	Measured (10.2 GHz)
1	25.9 dB	18.1 dB
2	27.0 dB	26.6 dB
3	20.7 dB	18.9 dB
4	19.1 dB	19.4 dB
5	25.5 dB	19.8 dB
6	19.1 dB	19.3 dB
7	20.7 dB	19.5 dB
8	27.0 dB	27.1 dB
9	25.9 dB	20.9 dB

Table 4.1: Input Return Loss (Positive Refraction Beamformer)

The results for all of the ports are shown in Fig. 4.14 for the negative refraction beamformer. A return loss greater than 10 dB was measured over a bandwidth of 0.5 GHz. The degradation in the impedance match is due to the fact that lower quality SMA connectors were used for this design rather than a fundamental issue with the negative refraction design. Next, the port-to-port isolation was characterized from 8 to 12 GHz by connecting

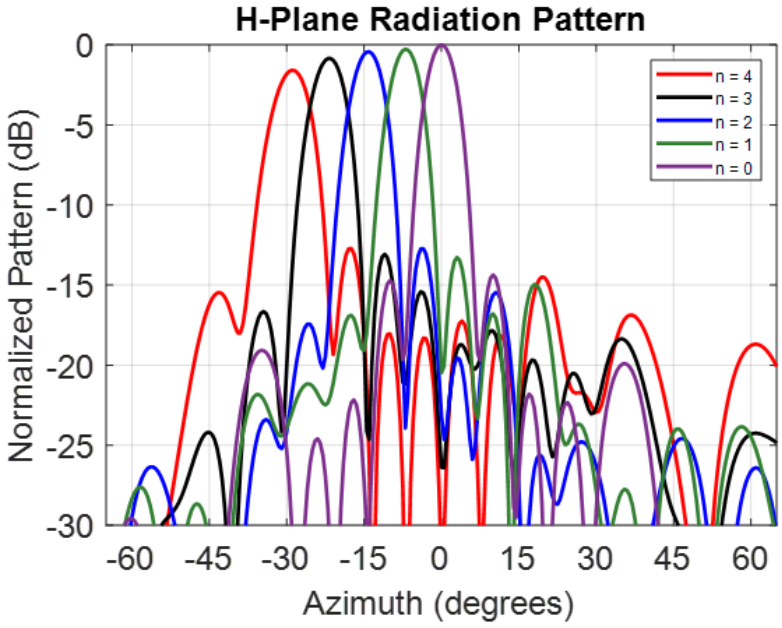

Figure 4.10: Full-wave simulation results of the co-polarized H-plane radiation patterns from the 3D printed aperture antenna. The plots are produced by exciting the simulated antenna (Ansys HFSS) with the output voltages from the full-wave simulation (Keysight Momentum) of the negative refraction metastructured beamformer. For clarity only the positive scan angles are shown. The negative scan angles are identical due to symmetry.

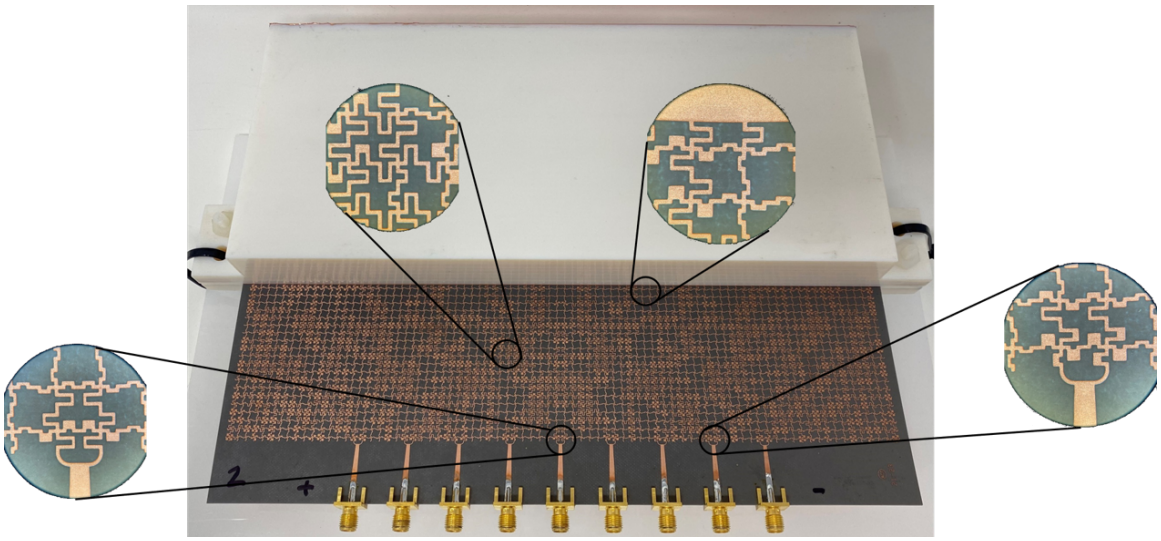

Figure 4.11: A picture of the patterned metastructured beamformer connected to the 3-D printed aperture antenna.

all possible pairs of ports one at a time and measuring S_{ij}, $i, j \in \{1, 2, ..., 9\}$, while the remaining ports were terminated in 50 Ω loads. By inspecting S_{ii} and S_{ij} for all of the ports, a frequency shift is observed in the beamformers performance. The frequency that

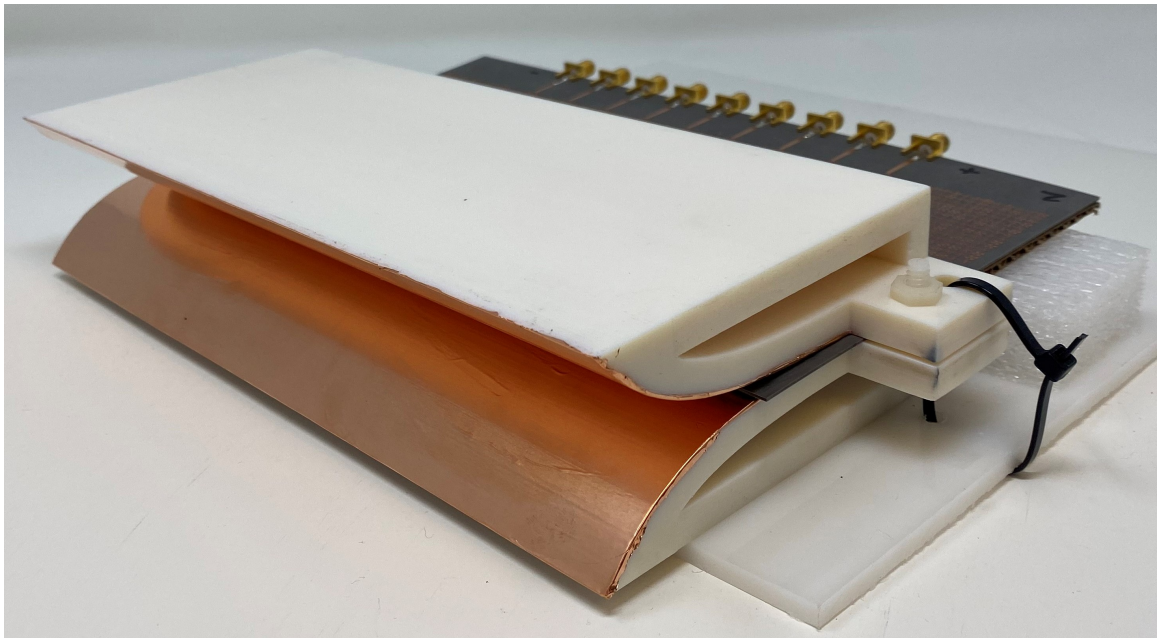

Figure 4.12: A picture of the 3D printed tapered aperture antenna. The aperture of the 3D printed part has been coated with copper tape to make it conductive.

Port	Simulated (10 GHz)	Measured (10.24 GHz)
1	24.0 dB	11.7 dB
2	34.7 dB	12.3 dB
3	23.2 dB	12.3 dB
4	24.0 dB	14.0 dB
5	27.2 dB	16.3 dB
6	24.0 dB	14.5 dB
7	23.2 dB	11.9 dB
8	34.7 dB	13.0 dB
9	24.0 dB	11.6 dB

Table 4.2: Input Return Loss (Negative Refraction Beamformer)

maximizes the minimum return loss and isolation for all of the ports is 10.24 GHz. This indicates that the beamformer's operating frequency has shifted to 10.24 GHz. The values for the return loss and isolation at this frequency are reported in Table. 4.2 and Table. 4.3, respectively. Where a good impedance match and high isolation are observed for all of the antenna's input ports.

4.4.2 Radiation Patterns

The antenna's far-field radiation patterns were measured with both beamformers in an anechoic chamber using a HP-83592A signal generator and an HP-8592L spectrum ana-

i \j	2	3	4	5	6	7	8	9
1	26.5	28.5	28.7	38.1	33.9	33.8	31.2	25.2
2	-	24.3	27.5	28.3	32.6	44.9	25.5	33.2
3	-	-	22.9	30.8	33.7	21.7	39.7	36.3
4	-	-	-	27.3	19.2	38.4	31.3	33.2
5	-	-	-	-	28.1	35.1	29.0	45.9
6	-	-	-	-	-	23.3	26.9	30.0
7	-	-	-	-	-	-	23.8	28.5
8	-	-	-	-	-	-	-	31.2

Table 4.3: Input Isolation for positive refraction beamformer (i and j refer to the port indices. All values are in dB.)

i \j	2	3	4	5	6	7	8	9
1	24.9	28.5	40.9	25.8	35.4	21.6	24.2	23.2
2	-	27.6	31.8	26.7	26.6	43.0	21.3	23.4
3	-	-	27.9	31.3	24.6	25.8	36.9	22.1
4	-	-	-	30.0	23.7	26.0	24.9	40.1
5	-	-	-	-	37.3	31.6	26.6	24.9
6	-	-	-	-	-	28.4	31.1	36.5
7	-	-	-	-	-	-	27.3	29.1
8	-	-	-	-	-	-	-	24.8

Table 4.4: Input Isolation for negative refraction beamformer (i and j refer to the port indices. All values are in dB.)

lyzer. Measured results for the radiation patterns are shown for $f = 10.2$ GHz for the positive refraction beamformer and $f = 10.24$ GHz for the negative refraction beamformer rather than $f = 10$ GHz. It should be noted that the beamformer was not optimized for bandwidth; and the sidelobe performance is narrowband. As noted in Section IV. A, the measurement frequency was determined by selecting the frequency that maximized the minimum return loss and isolation of all of the input ports. The co-polarized (co-pol) and cross-polarized (x-pol) H-Plane radiation patterns were measured for all nine beams.

The results for the co-polarized measurement are shown in Fig. 4.15a for the positive refraction design (plots of the individual radiation patterns can be found in Appendix D). Good agreement is shown with the simulated patterns in terms of the main beam and first sidelobes. The largest discrepancy is in the outer sidelobes for the beams at $\theta_B = \pm 30^\circ$ which are approximately 3 dB greater than the simulated value. The elevated sidelobes are most likely due to amplitude errors resulting from loss and manufacturing errors in the beamformer, and warping in the antenna that degrades the contact between the antenna and the parallel-plate waveguide on the PCB. The cross-polarized measurements are

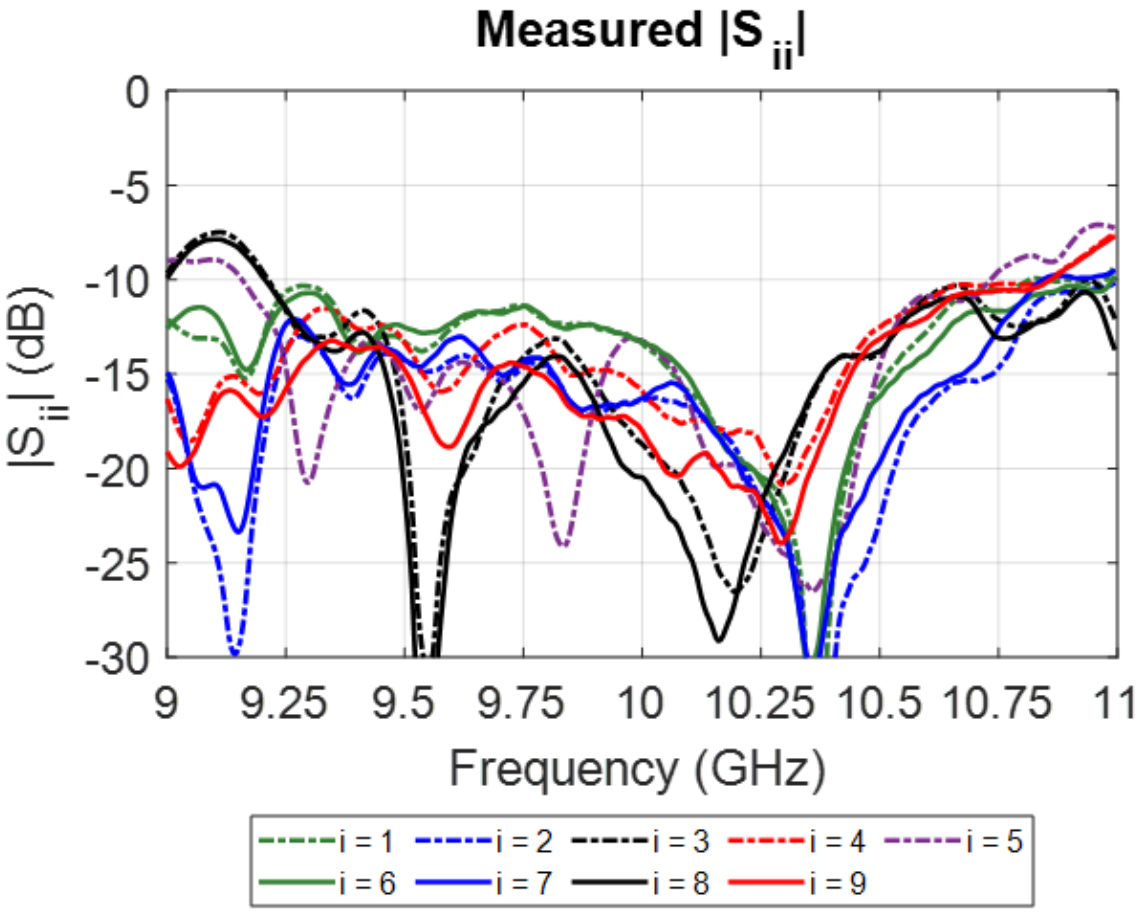

Figure 4.13: Plots of the measured reflection coefficient magnitudes ($|S_{ii}|$) for the positive refraction beamformer the multi-beam antenna's input ports from 9 to 11 GHz.

shown in Fig. 4.15b, verifying that the cross-polarized radiation is low. Additionally, the co-polarized and cross-polarized E-plane radiation patterns are measured for the $n = 0$ (broadside) beam. The radiation pattern for these measurements are shown in Fig. 4.16a and Fig. 4.16b. The co-polarized E-plane radiation pattern shows good agreement with the simulated result between $-25°$ and $15°$. The discrepancies between the measured and simulated radiation patterns outside of this range of angles is most likely a result of warping in the surface of the manufactured antenna's aperture.

The results for the co-polarized measurement are shown in Fig. 4.17a for the negative refraction design (plots of the individual radiation patterns can be found in Appendix D). Good agreement is shown with the simulated patterns in terms of the main beam and first sidelobes. The largest discrepancy is for the beams at $\theta_B = \pm 30°$ where higher sidelobes occur at the angle $\theta = \mp 33°$ for the main. The elevated sidelobes are most likely due to amplitude errors resulting from manufacturing errors and loss in the beamformer, and

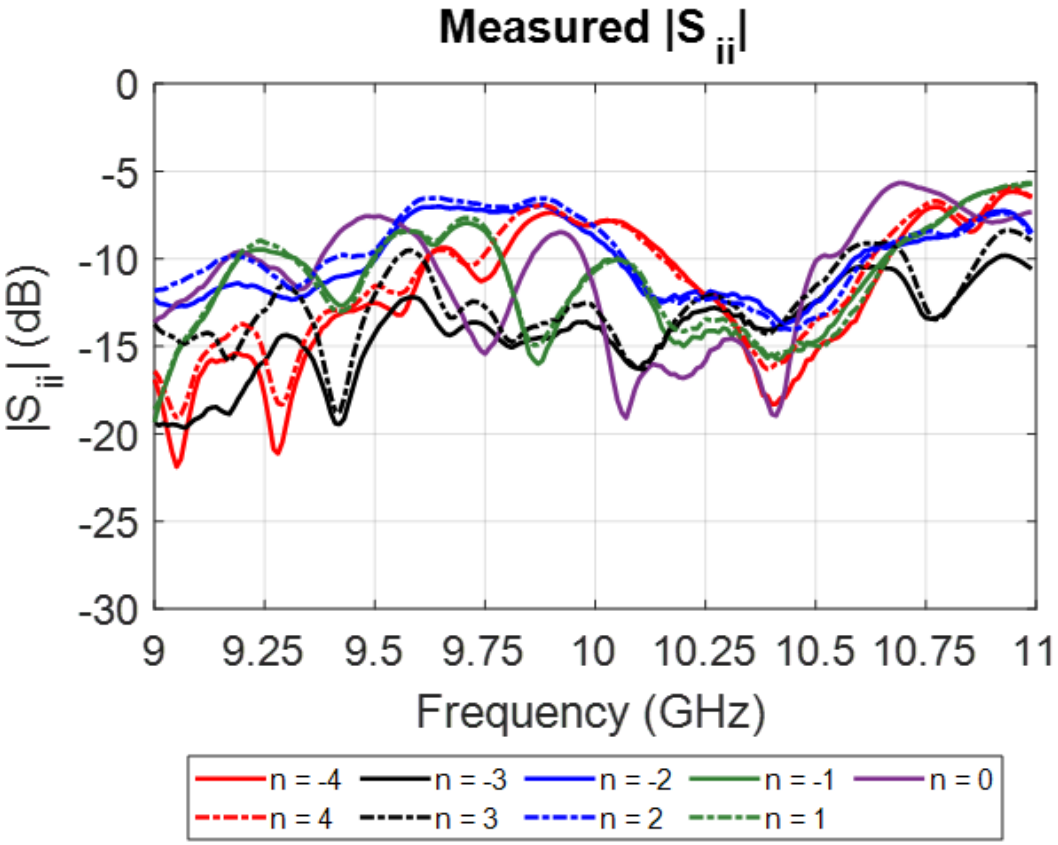

Figure 4.14: Plots of the measured reflection coefficient magnitudes ($|S_{ii}|$) for the negative refraction beamformer the multi-beam antenna's input ports from 9 to 11 GHz.

warping in the antenna that degrades the contact between the antenna and the parallel-plate waveguide on the PCB. The cross-polarized measurements are shown in Fig. 4.17b, verifying that the cross-polarized radiation is low. Additionally, the co-polarized and cross-polarized E-plane radiation patterns are measured for the $n = 0$ (broadside) beam. The radiation pattern for these measurements are shown in Fig. 4.18a and Fig. 4.16b. The co-polarized E-plane radiation pattern shows good agreement with the simulated result between $-25°$ and $15°$. The discrepancies between the measured and simulated radiation patterns outside of this range of angles is most likely a result of warping in the surface of the manufactured antenna's aperture.

Using the 3-dB beamwidths of the E and H-plane radiation patterns for the broadside beam, the maximum directivity of the measured antenna is approximated using formulas from [82] and [83]. These values are compared to approximations of the simulated an-

	Simulated	(+) Measured	(-) Measured
[82]	22 dB	22 dB	21.5 dB
[83]	18.4 dB	18.2 dB	17.1 dB
Actual	20.6 dB	-	-

Table 4.5: Approximate Directivity for the Broadside Excitation (The (+) indicates the positive refraction design and the (-) indicates the negative refraction design.)

n	(+) Gain	(-) Gain
-4	16.1 dB	15.4 dB
-3	16.8 dB	16.2 dB
-2	17.5 dB	17.0 dB
-1	17.9 dB	16.8 dB
0	17.9 dB	17.3 dB
1	17.6 dB	16.9 dB
2	17.6 dB	17.3 dB
3	17.1 dB	16.6 dB
4	15.8 dB	15.3 dB

Table 4.6: Measured Gain (The (+) indicates the positive refraction design and the (-) indicates the negative refraction design.)

tenna's directivity using the 3-dB beamwidths of its E and H-planes. As seen in Table 4.5 the measured values are in close agreement with those from the simulation for the positive refraction case whereas, there is more of a discrepancy for the negative refraction case. This discrepancy is due to the distortion in the measured E-plane radiation pattern for the negative refraction beamformer. This indicates that the actual directivity of the manufactured antenna fed by the positive refraction beamformer should be close to the simulated directivity of $D_0 = 20.6$ dB. This allows for the efficiency of the antenna to be characterized by comparing the measured gain to simulated gain. The gain for each scan angle was measured using a standard gain horn and the gain-transfer method, [57]. The measured gain for all nine beams are shown in Table 4.6. Comparing these values to the simulated directivity indicates that there is approximately 2.7 dB of loss in the positive refraction beamformer. Since the measured and simulated approximation for the directivity of the antenna fed by the negative refraction beamformer do not agree as well the loss cannot be characterized in the same manner. However, an estimate of the loss can be obtained by comparing the results to the those obtained with the positive refraction beamformer. Since the directivity is reduced by approximately 0.5 dB and the gain is reduced by 0.6 dB for the $n = 0$ excitation when using the negative refraction beamformer, the loss is around $2.7 - 2.8$ dB for the negative refraction beamformer.

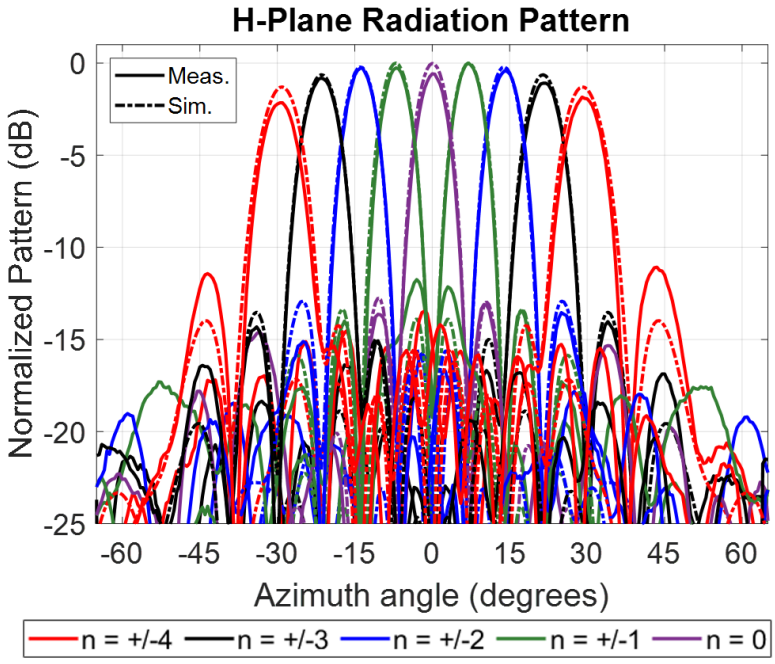

(a)

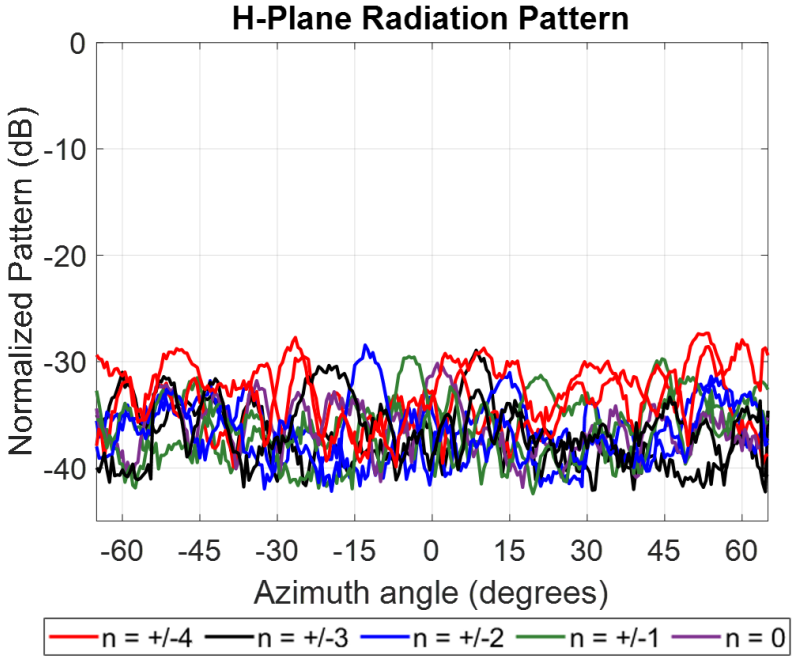

(b)

Figure 4.15: (a) A comparison of the measured and simulated normalized co-polarized H-plane radiation pattern from the positive refraction for all nine inputs. The measured radiation patterns are the solid lines and the simulated radiation patterns are the dot-dashed lines. (b) The measured cross-polarized H-plane radiation pattern for all nine inputs, normalized by the maximum of the co-polarized radiation pattern for the same input.

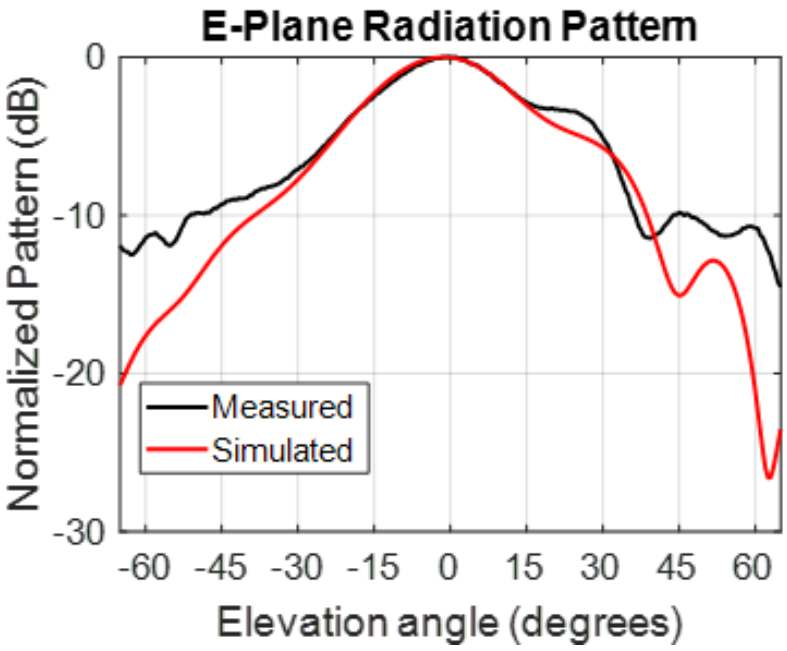

(a)

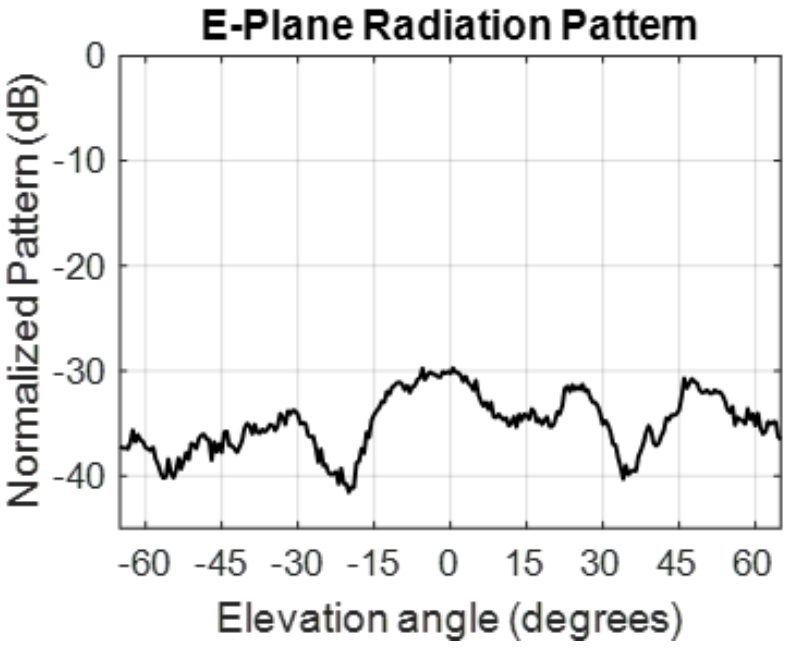

(b)

Figure 4.16: (a) A comparison of the measured and simulated normalized co-polarized E-plane radiation pattern from the positive refraction for the broadside beam ($n = 0$). (b) The measured cross-polarized E-plane radiation pattern from the positive refraction for the broadside beam, normalized by the maximum of the co-polarized radiation pattern for the same input.

To characterize beamformers bandwidth the co-polarized H-plane radiation pattern, for the $n = 0$ and $n = -4$ ports, was measured at 0.1 GHz steps above and below the center frequency for each of the beamformers. Only the $n = 0$ and $n = -4$ ports are measured because the performance of the other beams lies in between these two. The results of these measurements are shown in Fig. 4.19a-4.19d. In these figures some of the measured frequencies are excluded for clarity. The bandwidth of the positive refraction beamformer is determined using Fig. 4.19a and 4.19b. Here, it is observed that the reduction in gain for both ports is less than 3-dB from $10.1 - 10.5$ GHz, and the bandwidth is limited by the $n = 0$ input where a reduction in gain of approximately 4.25 dB is observed at 10 GHz and 10.6 GHz. Therefore, the positive refraction beamformer has a bandwidth of approximately 4%. The bandwidth of the negative refraction beamformer is determined using Fig. 4.19c and 4.19d. Here, it is observed that the reduction in gain for both inputs is less than 3-dB from $10.04 - 10.34$ GHz, and the bandwidth is limited by the $n = -4$ input where a reduction in gain of approximately 3 dB is observed at 10.04 GHz and 4.5 dB at 10.44 GHz. Therefore, the negative refraction beamformer has a bandwidth of approximately 3%.

4.5 Summary

A multi-beam antenna system using metastructured beamformers integrated with a 3D printed aperture antenna were reported. A previously reported computational inverse design procedure for MIMO metastructures was used to design the beamformer. The design procedure uses a fast, forward solver that leverages circuit theory to circumvent the use full-wave simulations, and the adjoint variable method to calculate gradients. This approach significantly reduces the computational cost of designing MIMO metastructures that are electrically-large and aperiodic, like antenna beamformers.

To validate the design procedure, the metastructured beamformer was patterned on a microwave substrate and integrated with a 3D printed aperture antenna. The measured performance of the antenna system was shown to be in good agreement with the simulated results, after accounting for a frequency shift in the manufactured beamformer. The work demonstrates that the design procedure is able to design devices that can be realized in practice. Including devices that perform extreme field transformations like negative refraction.

The reported beamformers demonstrate MIMO metastructures capability to maintain planar interfaces, control the amplitude and phase of all aperture fields and reduce the size of beamformers. Future work will tackle the beamformer's narrow bandwidth and mitigate amplitude and phase errors present in the aperture fields. Potential methods for improving

the bandwidth are the inclusion of multiple frequencies in the cost function and introducing lossy terminations to mitigate reflections. Accuracy of the aperture fields could potentially be improved by using better models of the unit cells. This could be achieved by modeling the unit cells more accurately using multi-modal admittance matrices to capture higher-order coupling between the unit cells.

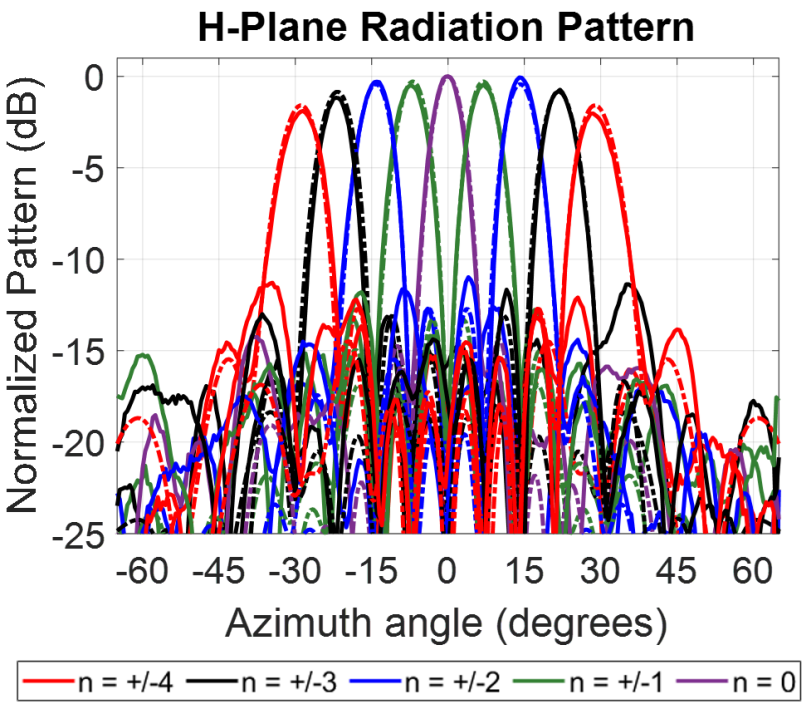

(a)

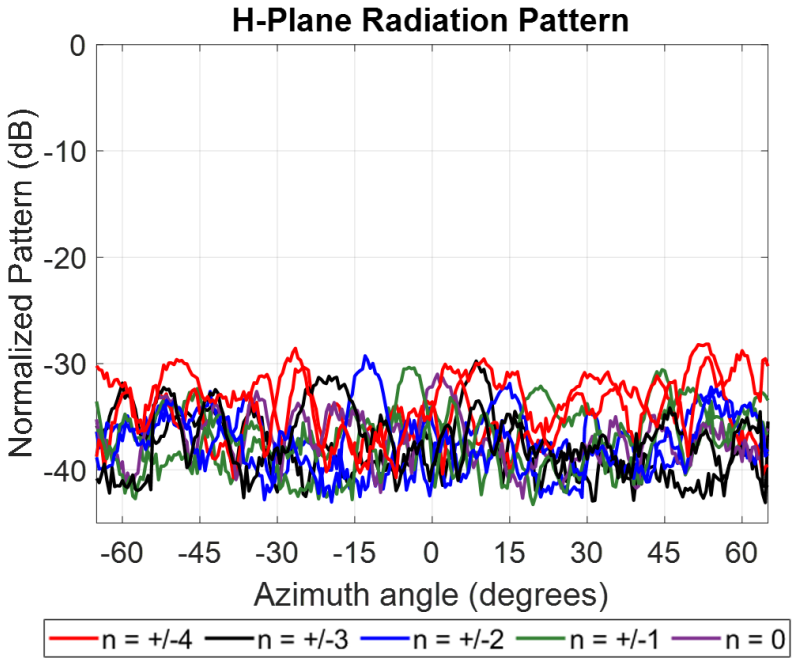

(b)

Figure 4.17: (a) A comparison of the measured and simulated normalized co-polarized H-plane radiation pattern from the negative refraction for all nine inputs. The measured radiation patterns are the solid lines and the simulated radiation patterns are the dot-dashed lines. (b) The measured cross-polarized H-plane radiation pattern for all nine inputs, normalized by the maximum of the co-polarized radiation pattern for the same input.

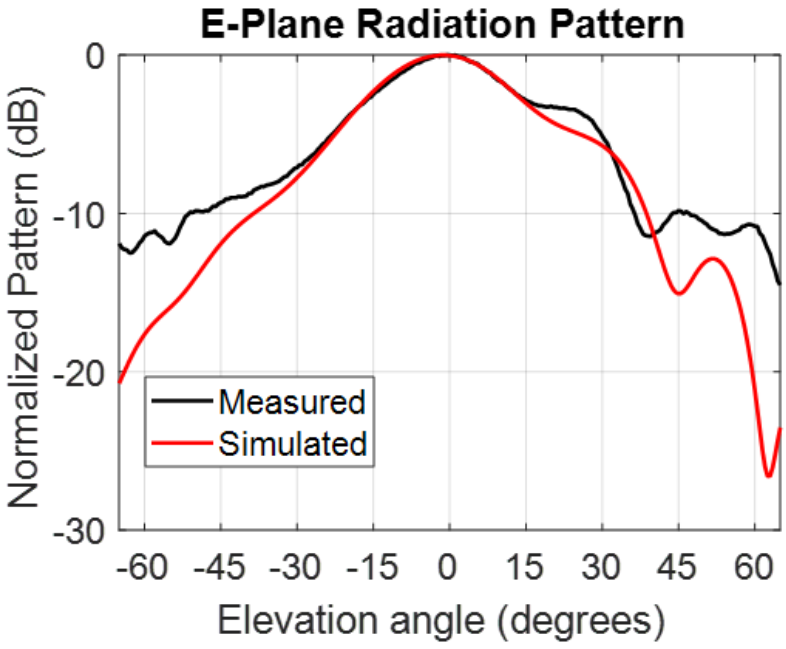

(a)

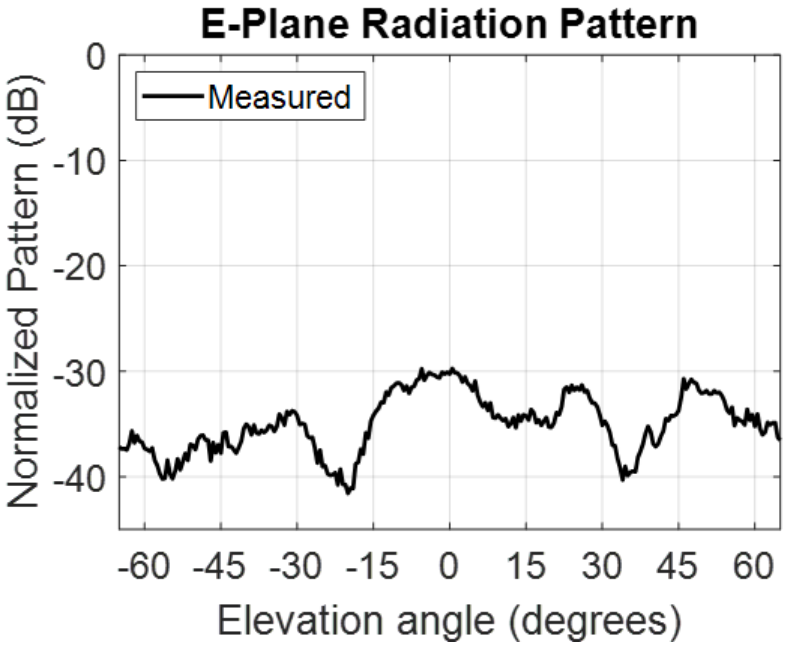

(b)

Figure 4.18: (a) A comparison of the measured and simulated normalized co-polarized E-plane radiation pattern from the negative refraction beamformer for the broadside beam ($n = 0$). (b) The measured cross-polarized E-plane radiation pattern from the negative refraction for the broadside beam, normalized by the maximum of the co-polarized radiation pattern for the same input.

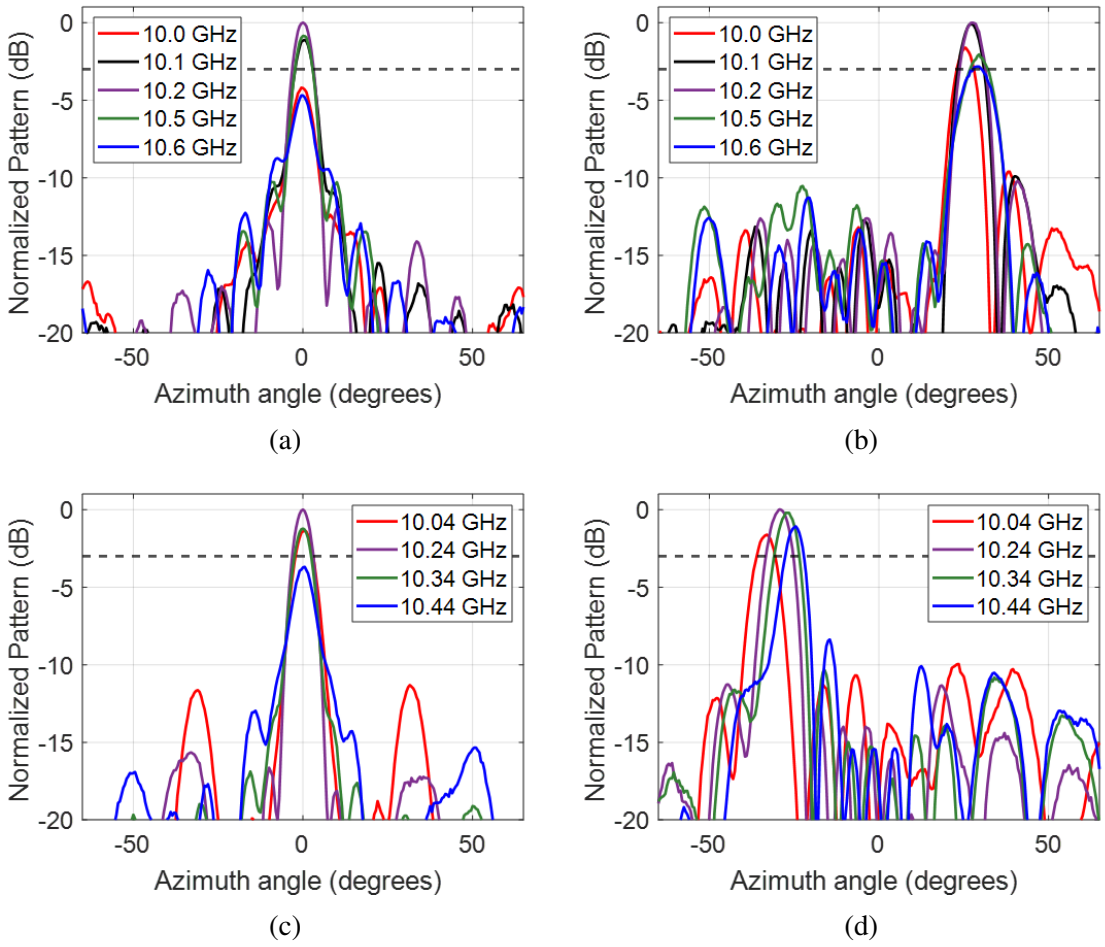

Figure 4.19: Plots of the measured co-polarized H-plane radiation patterns of the multi-beam antenna fed by the two beamformers: positive refraction design (a) n = 0 (b) n = -4, negative refraction design (c) n = 0 (d) n = -4. The dashed black line indicates a decrease of 3 dB in the gain relative to the center frequency of the beamformer. From (a) and (b) it is seen that the positive refraction beamformer has a fractional bandwidth of approximately 4% and (c) and (d) indicate that the negative refraction beamformer has a fractional bandwidth of approximately 3%.

CHAPTER 5

Conclusion

5.1 Summary of Contributions

Since the early days of metamaterials research, researchers have used microwave circuit concepts to develop models that provide physical insight and enable the design of metamaterial devices such as leaky-wave antennas [32, 84] and beamformers [11, 74]. This thesis focused on recent advances in the use of microwave circuit concepts for modeling and designing metamaterials and metastructures. The first part of this thesis, Chapter 2, used these concepts to develop a model for wave propagation in 2D omega bianisotropic media. Then in the second part, Chapters 3 and 4, they were leveraged to develop a fast forward problem solver to enable a computational inverse design procedure for MIMO metastructures.

In Chapter 2, a circuit-based unit cell for modeling 2-D omega bianisotropic materials was introduced. In previous work, circuit-based methods for modeling arbitrary electric and magnetic material responses had been provided. However, circuit-based models for 2-D wave propagation in materials with magneto-electric responses were not available. Here, a circuit-based unit cell composed of four constitutive microwave networks connected in a cross-junction was proposed to model 2-D wave propagation in an omega bianisotropic medium. It was then shown that when all four of the constituent networks are different the unit cell becomes spatially dispersive. To limit this effect the condition that the constituent networks along the two principal axes should be the same was imposed on the unit cells. Therefore, if the constituent networks are symmetric the unit cell would also symmetric precluding the possibility of an omega bianisotropic response. Therefore, to model omega type magneto-electric responses the constituent networks must themselves contain asymmetries. A lumped element propagation model was then provided where the constituent networks were composed of π-networks. The propagation model was verified by synthesizing a omega bianisotropic medium and simulating its isofrequency contours in Keysight ADS. Finally, a design example was provided to demonstrate that 2-D omega bianisotropic

media have the potential to realize devices with amplitude and phase control. An example of an electrically-thin impedance matched slab that provides a desired phase delay and translates the normal power density profile of a Gaussian beam was designed and verified in Keysight ADS.

In Chapter 3, a computational inverse design procedure was introduced for the design of guided-wave metastructures. Two significant difficulties are encountered when designing metastructures with optimization-based approaches are: (1) the large-scale optimization problem posed by metastructures (2) the computational cost of the solution to the forward problem. The first problem is a result of the large number of degrees of freedom found in metastructures, typically greater than 10^3 design variables, which presents a large-scale optimization problem that can be difficult to solve. The second results from the fact that metastructures present a multi-scale simulation problem because, the metastructures are themselves wavelength scale devices but are composed of unit cells with deeply subwavelength features. Both of these issues significantly increase the computational effort, often making inverse design impractical when the devices are electrically-large. The large-scale optimization problem was addressed in this work by adopting the adjoint variable method to calculate derivatives. The multi-scale simulation problem was addressed by using a circuit-network solver to model the wavelength scale devices behavior and reduced-order models to capture the effects of the subwavelength features in the unit cells. In this way, computationally expensive full-wave solutions to the device responses could be avoided during the optimization routine while maintaining good accuracy. The validity of this modeling approach was then established by designing a metastructured beamformer and an analog signal processing network whose performance were verified through full-wave simulations in Keysight Momentum.

There are two main advantages of this inverse design approach: (1) its computational efficiency and (2) it models the exact patterned unit cells. The first advantage was already discussed above however, the second has not been addressed yet. There are several distinct advantages of modeling the exact structure over using effective medium theory and full-wave solvers to design MIMO metastructures. Even when the full-wave solvers produce linear systems of similar size and structure to the circuit network solver (finite element or finite-difference frequency-domain). One advantage is that the unit cells do not require the existence of a medium equivalence, as in the case of the asymmetric unit cell discussed in Chapter 2. In fact, the unit cells do not even need to be homogenizable. Therefore, there are no restrictions on the size or types of inclusions that can be modeled. Another advantage is that by modeling the patterned unit cells the design procedure produces the layout of the patterned structure. This avoids the need for an additional patterning step,

which often requires additional full-wave optimization to account for spatial dispersion that is neglected in the design procedure. Whereas, this design method accounts for any spatial dispersion in device and can produce a device with good performance without any full-wave optimization.

In Chapter 4, it was experimentally verified that the inverse design procedure, introduced in Chapter 3, could be used to realize practical devices. This chapter outlined the design of a multi-beam antenna system composed of a metastructured beamformer and a tapered aperture antenna. The tapered aperture antenna was additively manufactured using a commercially available 3D printer and the aperture was metalized using copper tape. To verify the design procedure the antenna was fed by two different metastructured beamformers: one that exhibited positive refraction and another that exhibited negative refraction. The positive refraction example takes advantage of the natural phase delays that are produced along the output of the beamformer by the different inputs. Whereas the negative refraction version reverses the natural phase delays, demonstrating the extreme field transformations that metastructures can provide in compact regions. The two beamformers were designed using the inverse design procedure, with no additional full-wave optimization, and patterned on a Rogers/RT Duroid 5880 substrate. The multi-beam antenna system was then characterized using measurements of its input impedance match, isolation, and far-field radiation patterns. This work demonstrated that the inverse design procedure is capable of accurately modeling spatially varying metastructures, and can be used to realize practical devices with arbitrary control over multiple field transformations.

5.2 Future Work

The first part of this thesis introduced a circuit-based method for modeling TE wave propagation in a 2-D omega bianisotropic medium. A model composed of lumped element π-networks was used, which could potentially be used in low-frequency applications to realize effective media with omega bianisotropic responses. However, different physical structures with 2-D omega responses are necessary to realize practical microwave devices that possess 2-D omega bianisotropy. Potentially, practical structures with these material responses could be realized as printed-circuit structures, additively manufactured structures composed of omega-particles, [24], or a media composed of loaded loops and dipoles similar to [85].

Here, polarization conserving media were considered however, the circuit network model could include more general material responses by extending Kron's work, [86], to include material with bianisotropic responses. This could be accomplished by developing

a dual network for TM propagation in an analogous manner to this work. By coupling the network presented in this work to the dual network, polarization conversion could be achieved allowing for the design of devices with phase, amplitude and polarization control. Another limitation of this model is that it can only model propagation in a medium where its principal axes are aligned with axes of the periodic circuit network, i.e. diagonal permeability tensors. However, this precludes the ability to redirect the power flow of normally incident waves. This requires off-diagonal elements in the material's permeability tensor. To allow for the design of devices that can redirect the power of normally incident waves, the unit cell would need to be modified to include off-diagonal elements in the permeability tensor. This could potentially be achieved by using a model similar to those presented in [21] to realize full-tensor circuit-based omega bianisotropic metamaterials.

The second part of this thesis introduced an inverse design procedure to realize guided wave metastructured devices. The design procedure used port-fed circuit models to represent the unit cells of the device. Which, allowed for accurate solutions to the device response without using full-wave simulations during the optimization routine. However, the results from the full-wave solver and circuit network solver did not match exactly. Indicating that the accuracy of the circuit network solver could potentially be improved if the error sources were isolated and modeled. One possible error source is that the current model only considers unit cells supporting a single guided mode at each port face. This carries with it the underlying assumption that there is only one accessible mode at its ports. This assumption is valid if two conditions are met: (1) there is only one propagating mode supported by the waveguide and (2) any discontinuities in the waveguide are far enough away from the port faces such that the amplitude of any evanescent modes that are excited are sufficiently decayed. If both of these conditions are not met then the model's accuracy degrades and the solutions can become unreliable.

Since metastructures unit cells are deeply subwavelength it is rare that the port faces will be sufficiently far away from discontinuities (inclusions) such that no evanescent modes are accessible at the port faces. In fact, these conditions were not strictly met in the designs presented in this work, which is likely the cause of the discrepancy between the device's response calculated using the circuit network solver and the full-wave solver. Therefore, the accuracy of the solver could be improved by considering multiple modes at the port faces to account for higher-order wave coupling between the unit cells, [69]. This would result in a slower forward problem solver, as the size of the matrices grows proportionate to the square of the number of modes included. Therefore, there is a trade-off between accuracy and computational efficiency that needs be accounted for when developing the circuit network solver for a given design problem.

Recently, there has been significant interest in analog and hybrid beamforming methods that are suitable for millimeter, terahertz and optical systems [87–89]. In chapter 4, the advantages of metastructured beamformers were discussed and some of these advantages were demonstrated in the beamformers designed in this thesis. However, the designed beamformers were relatively narrowband with a fractional bandwidth of 4% for the positive refraction beamformer and 3% for the negative refraction beamformer. In order to design beamformers that can be used in communication and radar systems the bandwidth of these devices needs to be improved. Therefore, methods for modifying the inverse design procedure to allow for broadband devices to be designed could be investigated. One possible method would to be to characterize the unit cells at multiple frequencies and to form a cost function at several frequencies as in [90].

If metastructured beamformers are designed to be broadband, as in [11], they could be well suited for use in millimeter, terahertz and optical systems where phased arrays and digital beamforming techniques are more complicated and expensive to realize. If the design procedure presented in this work can be modified to allow for the design of wideband devices it could potentially be used to realize metastructured beamformers for these systems. However, there are several other challenges that would need to be overcome such as the development of low-loss cells that provide enough variation and methods to accurately model them. Low-loss unit cells with a large amount of variation could potentially be realized using all-metal unit cells at millimeter-wave frequencies and could be modeled using multiple modes similar to [69]. On the other hand, all-dielectric unit cells are most likely needed for optical devices which, could prove more challenging to model and design with enough variation in the response to realize compact beamformers. One possible method could be to use multiple modes to model unit cells composed of high-index anisotropic inclusions embedded in dielectric waveguides similar to, [91].

APPENDIX A

Three-Sheet Metasurfaces: Bandwidth and Quality Factor

In practice, bi-isotropic metasurfaces typically rely on resonant structures to produce the strong field interactions required to perform desired field transformations. However, the use of resonances places inherent limitations on the bandwidth. In this section, the relationship between matching networks and bi-isotropic metasurfaces is considered, and the quality factor of a metasurface realized using three impedance sheets is defined. We demonstrate that the quality factor can be used as a metric to predict the metasurface bandwidth and identify unit cells that degrade the performance of inhomogeneous metasurfaces.

To understand the relationship between impedance matching networks and bi-isotropic metasurfaces, we consider the following example. Suppose there is a planar interface between air and alumina ($\varepsilon_r = 9.4$), as in Fig. A.1, and the goal is to maximize the power transferred across the interface. Since the intrinsic wave impedances of the media are real, this amounts to minimizing the amplitude of the reflected wave. To do this, the input impedance of the metasurface must be equal to the wave impedance of the incident wave, Z_{in}. Since the two media have different wave impedances the metasurface must transform the wave impedance of the transmitted wave, Z_L, to that of the incident wave, Z_{in}. In this scenario, the metasurface acts as an impedance matching layer. Here, the impedance matching layer is analogous to an impedance matching network from circuit theory like an L or T-network, shown in Fig. A.2. From circuit theory, it is known that a complex load impedance can be matched to complex source impedance using either an L-network, T- or π-network. The L-network contains two degrees of freedom allowing for the real and imaginary components of the input impedance to be matched. For an L-network, the solution is unique (all degrees of freedom are used) and no other characteristics of the impedance match, such as it's bandwidth or the transmission phase, can be controlled. Adding a third degree of freedom to the L-network produces a T- or π-network. This additional degree of freedom can be used to control the bandwidth or the transmission phase. Bi-isotropic

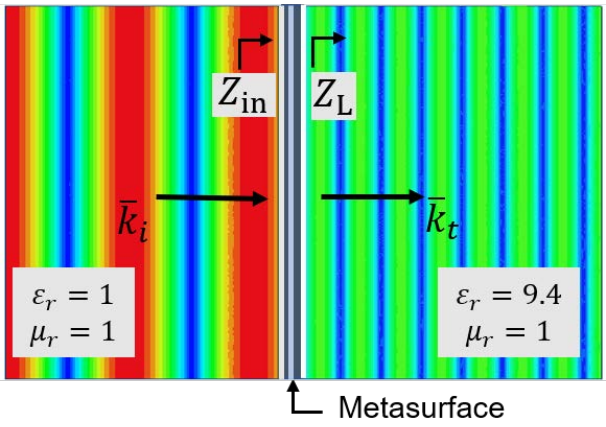

Figure A.1: A metasurface at the interface between air and alumina half-spaces. The metasurface is used to impedance match a normally incident plane wave travelling from the region of air into the alumina.

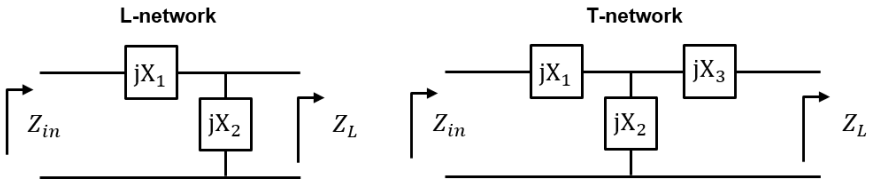

Figure A.2: L and T circuit network topologies used for impedance matching in circuit theory.

metasurfaces are like T-matching networks for fields. They have three degrees of freedom that allow impedance matching with phase or bandwidth control [59]. To illustrate this idea, we consider a metasurface that impedance matches a normally incident plane wave on an air-alumina ($\varepsilon_r = 9.4$) interface over a maximum bandwidth, as shown in Fig. A.1.

To design the impedance matching metasurface, recall that a bi-isotropic metasurface can be viewed as a two-port network that controls one scattering amplitude and two scattering phases, [92]. Therefore, designing a lossless, reflectionless, bi-isotropic metasurface is equivalent to designing a lossless two-port impedance matrix (Z-matrix) that impedance matches a load impedance $Z_L = |Z_L|e^{j\phi_L}$ to a source impedance $Z_i = |Z_{in}|e^{j\phi_{in}}$ with an arbitrary transmission phase ϕ_{21} [40]. To determine the Z-matrix that provides the desired functionality, consider a general lossless two-port Z-matrix,

$$\begin{pmatrix} V_1 \\ V_2 \end{pmatrix} = j \begin{pmatrix} X_{11} & X_{12} \\ X_{21} & X_{22} \end{pmatrix} \begin{pmatrix} I_1 \\ I_2 \end{pmatrix} \tag{A.1}$$

Imposing the impedance boundary conditions and enforcing power conservation on (A.1) produces the following system of equations,

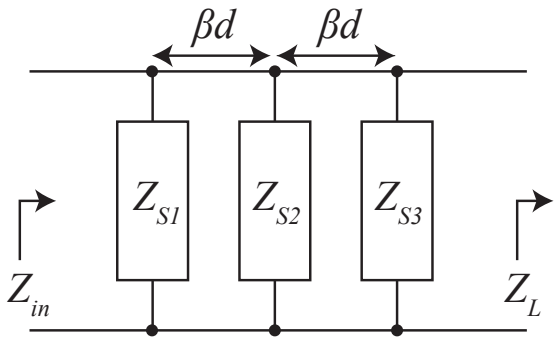

Figure A.3: Bi-isotropic metasurface realized using three impedance sheets separated by dielectric spacers with thickness d.

$$\begin{pmatrix} 1 \\ r_v e^{j\phi_{21}} \end{pmatrix} = j \begin{pmatrix} X_{11} & X_{12} \\ X_{21} & X_{22} \end{pmatrix} \begin{pmatrix} 1 \\ -r_v e^{j\phi_{21}} \end{pmatrix} \tag{A.2}$$

where $r_v^2 = \frac{Z_L}{Z_{in}} \left| \frac{\cos\phi_{in}}{\cos\phi_L} \right|$ and $\phi_{21} = \angle V_2 - \angle V_1$. Splitting (A.2) into its real and imaginary components allows for the elements of the Z-matrix to be solved for in terms of Z_L, Z_{in} and ϕ_{21},

$$\begin{pmatrix} X_{11} & X_{12} \\ X_{21} & X_{22} \end{pmatrix} = \begin{pmatrix} |Z_{in}|\cos(\phi_{21}-\phi_L) & |Z_{in}|r_v\cos(\phi_L) \\ |Z_{in}|r_v\cos(\phi_L) & |Z_L|\cos(\phi_{21}+\phi_{in}) \end{pmatrix} \csc(\phi_{21}+\phi_{in}-\phi_L) \tag{A.3}$$

From (A.3), it is clear that the required two-port network is reciprocal since $X_{12} = X_{21}$, and has three degrees of freedom. As in [39], three cascaded sheet impedances, shown in Fig. A.3, can be used to realize a metasurface with a Z-matrix given by (A.3).

Expressing Fig. A.3 in terms of it's Z-matrix, and solving for the necessary impedance sheets, results in the following expressions for the sheets in terms of the elements of (A.3),

$$Z_{s1} = -j\frac{Z_0\sin(\beta d)}{\cos(\beta d) + (\frac{X_{12}+X_{22}}{\det Z})Z_0\sin(\beta d)} \tag{A.4}$$

$$Z_{s2} = -j\frac{Z_0^2\sin^2(\beta d)X_{12}}{\det Z + X_{12}Z_0\sin(2\beta d)} \tag{A.5}$$

$$Z_{s3} = -j\frac{Z_0\sin(\beta d)}{\cos(\beta d) + (\frac{X_{12}+X_{11}}{\det Z})Z_0\sin(\beta d)}, \tag{A.6}$$

where $\det Z$ is the determinant of the Z-matrix and β and Z_0 are the wavenumber and wave impedance of the dielectric spacers, respectively. Once the input and load impedances, spacer thickness, and the transmission phase is specified, (A.3) can be used to determine

the necessary impedance sheets to implement the metasurface.

To maximize the bandwidth of the impedance match, a method is needed for comparing the metasurface bandwidth for different transmission phases. Here, an expression of the metasurface quality factor as a function of the transmission phase is derived for this purpose. The quality factor of the three sheet metasurface is defined as,

$$Q = \omega_0 \frac{2W_e}{P_d}, \tag{A.7}$$

where ω_0 is the angular resonant frequency, W_e is the average electric energy stored in the network at ω_0, and P_d is the power dissipated in the network. To calculate the quality factor using (A.7), the impedance sheets (A.4)-(A.6) are expressed in terms of lumped capacitances and inductances. The dielectric spacers in the metasurface are assumed to be electrically thin, so they can be modelled as lumped π-networks. Therefore, if the dielectric spacers are electrically thin and the source and load impedances are purely real, then the quality factor of the metasurface can be expressed as

$$Q = \frac{\omega_0}{2}\left(Z_{in}(C_{s1} + \frac{\beta d}{4\omega_0 Z_0}) + R_{int}(C_{s2} + \frac{\beta d}{2\omega_0 Z_0}) + Z_L(C_{s3} + \frac{\beta d}{4\omega_0 Z_0}) \right), \tag{A.8}$$

where, $R_{int} = \frac{Z_{in}+Z_L+\sqrt{Z_{in}Z_L}\cos\phi_{21}}{\sin^2\phi_{21}} \frac{(Z_0 \sin\beta d)^2}{Z_{in}Z_L}$, and C_{si} is the capacitance of the ith impedance sheet (if the sheet is inductive then $C_{si} = 0$). If the load impedances are not purely real, the imaginary part of the load can be absorbed into either Z_{s1} or Z_{s3}, and (A.8) can still be used. The quality factor, Q, of the metasurface will be used to approximate the fractional bandwidth, $FBW = BW/f_0$, where BW is the 3 dB bandwidth of each unit cell. However, due to the presence of multiple resonances this approximation is only valid when the resonances are well separated in frequency.

The quality factor expression (A.8) can be used to maximize the bandwidth of an impedance matching bi-isotropic metasurface. For a normally incident plane wave, the relevant impedance is $Z_{in} = 377\ \Omega$. Let's assume that $Z_L = 123\ \Omega$, and the spacers are free-space with a thickness $d = \lambda_0/20$. Using (A.8) to calculate the quality factor and the fractional bandwidth versus transmission phase, produces Fig. A.4. Fig A.4 (b) shows that the maximum bandwidth occurs at a transmission phase of $\phi_{21} = -68.5°$. Fig A.4 (a) plots (A.8) and predicts that this transmission phase maximizes the bandwidth, as shown in Fig. A.4 (c). The metasurface with this transmission phase is composed of the following impedance sheets: $Z_{s1} = 1/(j\omega C_{s1}) = -j468.9\ \Omega$, $Z_{s2} = 1/(j\omega C_{s2}) = -j641.9\ \Omega$, and $Z_{s3} = j\omega L_{s3} = j38.5\ \text{k}\Omega$. The metasurface performance is simulated in Ansys

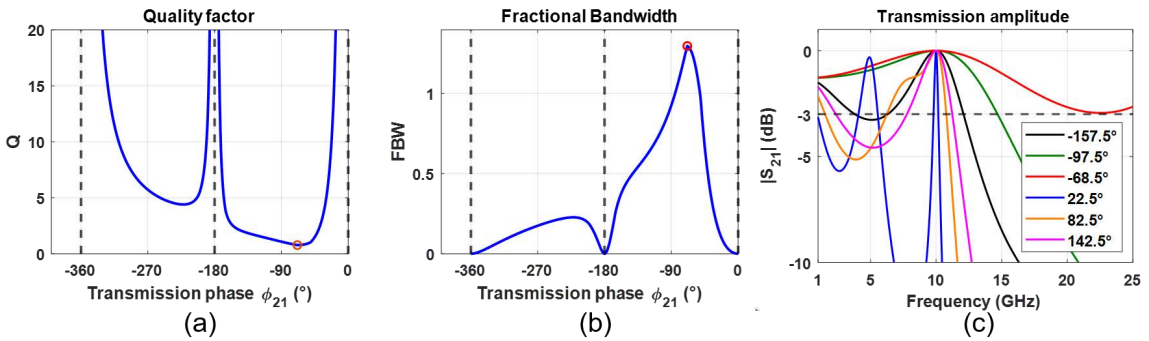

Figure A.4: The quality factor, fractional bandwidth, and the magnitude of the frequency response for metasurfaces that provide impedance matching with six different transmission phases. (a) The quality factor is minimized when the transmission phase is $-68.5°$ (red circle). (b) The fractional bandwidth is maximized at $-68.5°$ (red circle). (c) Plots of the transmission amplitude over frequency for several transmission phases and the maximum bandwidth is observed when the transmission phase is $-68.5°$ as predicted by the quality factor.

HFSS using dispersive impedance sheets that correspond to the following lumped elements: $C_{s1} = 33.9$ fF, $C_{s2} = 24.8$ fF, and $L_{s3} = 612.7$ nH. The transmission magnitudes from this simulation are shown in Fig. A.5, where they are compared to a quarter-wave transformer and the bare interface without any impedance matching. The metasurface has a size and bandwidth comparable to a quarter-wave transformer. However, it doesn't require the realization of a medium with the dielectric constant $\varepsilon_r = \sqrt{9.4}$, which can be heavy and challenging to manufacture.

In addition to bandwidth information, the quality factor also provides information that can guide the design of inhomogeneous metasurfaces where local periodicity is assumed. Obtaining good performance from a metasurface designed assuming local periodicity requires that neighboring unit cells produce fields that are approximately the same i.e. the fields vary smoothly along the surface without large discontinuities in amplitude or phase. In this work, it has been found that the quality factor and its first derivative with respect to transmission phase can help the designer select unit cells that satisfy the assumption of local periodicity.

The quality factor, given by (A.8), is divergent at transmission phases near $\phi_{21} = 0°, -180°$, and $-360°$, indicating that the unit cells required to achieve these transmission phases possess large quality factors. Large quality factors are associated with strong resonances which are sensitive to perturbations in the surrounding environment and are lossy when realized in practice. Therefore, these unit cells should be avoided. Additionally, areas where (A.8) is not smooth (i.e. points where the first derivative is discontinuous or unde-

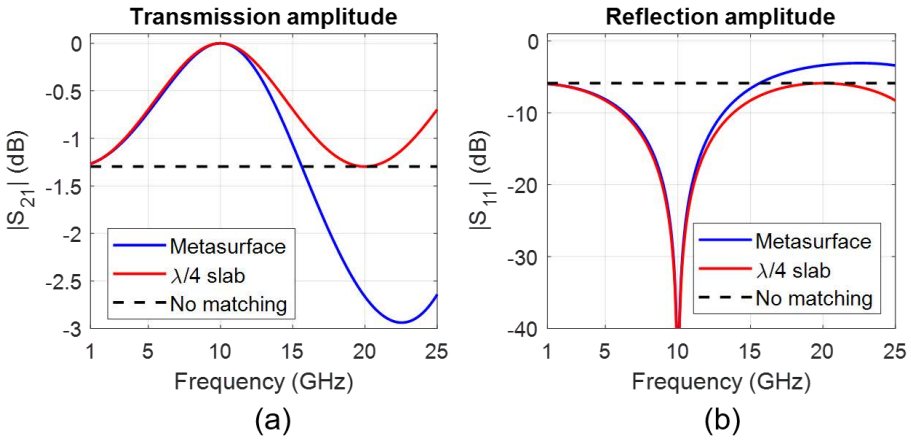

Figure A.5: Plots of the transmission and reflection magnitudes for the interface with the metasurface ($\phi_{21} = -68.5°$), a quarter-wave transformer, and with no impedance matching (bare interface). The simulations of the metasurface were performed in Ansys HFSS. The metasurface has a bandwidth that is comparable to a quarter-wave transformer.

fined) indicate transmission phases where the reactance of at least one of the impedance sheets changes sign. These points should also be avoided because they identify transmission phases where the required reactance values display asymptotic behavior. This introduces rapid variations in the values of the impedance sheets and fields in the metasurface that invalidate the assumption of local periodicity.

To see how this information can be used, consider a metasurface embedded in free-space that refracts a normally incident plane wave to $70°$ at a frequency of $f_0 = 10$ GHz. This requires a gradient metasurface: an inhomogeneous metasurface that imposes a linear phase gradient on an impinging wave-front to produce reflection or refraction into a desired direction [93]. Refraction requires the metasurface to alter the transverse wavenumber of an incident plane wave ($k_i = k\sin(\theta_i)$) to produce the desired refracted wavenumber ($k_t = k\sin(\theta_t)$), where k is the wavenumber in the surrounding medium. Therefore, the metasurface must impart transverse momentum equal to $\Delta k = k_t - k_i$. Practically, this is realized by discretizing the metasurface into N sub-wavelength unit cells of size $D = \frac{2\pi}{N\max(k_i,k_t)}$, each possessing a transmission phase ϕ_j such that $\Delta\phi = \phi_{j+1} - \phi_j = -\Delta k D$. Each unit cell must be reflectionless to maximize the transmitted power into the refracted wave. This means impedance matching and phase control are required, so (A.4)-(A.6) can be used to design the unit cells of the metasurface.

For this example, the metasurface will have 10 unit cells per transverse wavelength (in free-space) and the spacers will be assumed to be free-space with a thickness $d = \lambda_0/25$. As a first pass at the design, the metasurface is designed to impose a linear phase gradient with the unit cell transmission phases shown in Table A.1. The required sheet impedances,

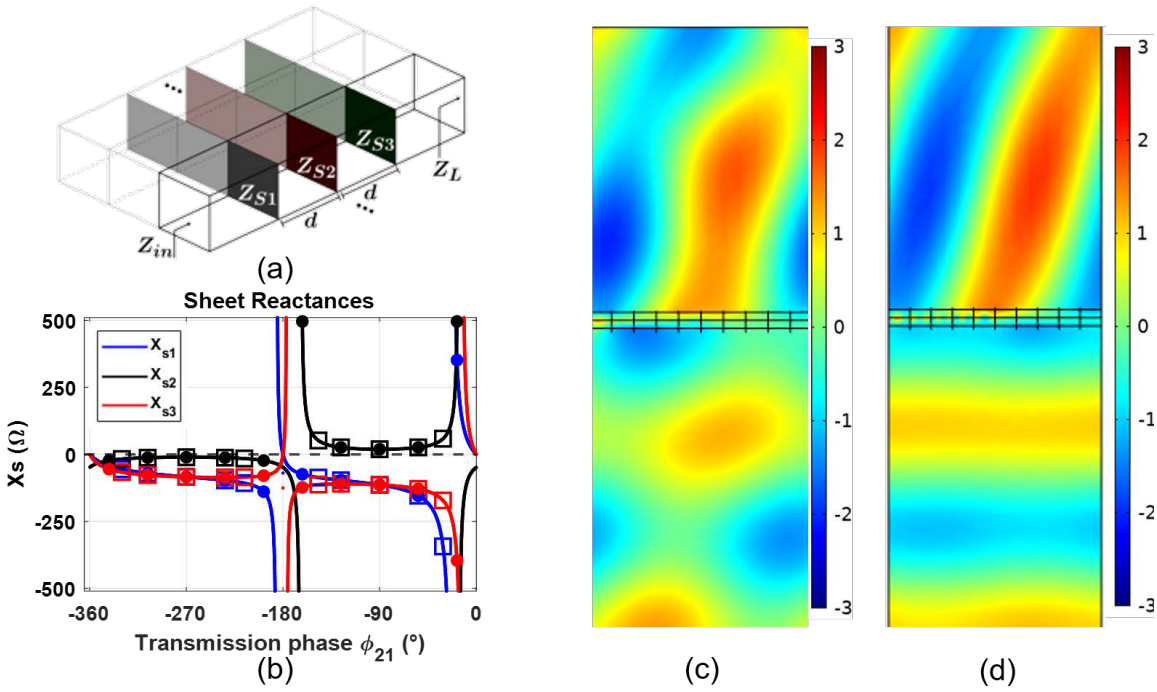

Figure A.6: (a) Depiction of an inhomogeneous, bi-isotropic metasurface implemented as a three sheet cascade in free-space. (b) Plots of the sheet reactances for different transmission phases. The solid circles indicate the values used for the linear phase gradient and the empty squares indicate the sheet values used for the perturbed phase gradient. (c) Full-wave simulation results for the real part of the electric field using the metasurface with a linear phase gradient. (d) Full-wave simulation results for the real part of the electric field using the metasurface with a perturbed phase gradient.

shown in Fig. A.6 (b), are solved for using (A.4)-(A.6) and one period (10 unit cells) of the metasurface is simulated in COMSOL using periodic boundary conditions. The results are shown in Fig. A.6 (c).

The metasurface designed using this phase gradient exhibits significant reflections and the transmitted wave is not purely refracted. A slight perturbation of the linear phase gradient can be used to improve the performance. The appropriate perturbed phase gradient can found using the quality factor and its first derivative with respect to transmission phase. To find problematic transmission phases in the original design, plots of the quality factor and its first derivative are shown in Fig. A.8. By inspecting the plots, four unit cells with problematic transmission phases are identified: 1, 5, 6, and 10. Unit cells 1, 5, and 6 are problematic because they are near points where (A.8) is not smooth, and unit cell 10 is problematic due to its large quality factor. To improve the performance of the metasurface, the problematic transmission phases are adjusted as shown in Table A.1. These phase shifts reduce the maximum unit cell quality factor by approximately 10 and force the reactance

Unit cell	ϕ_{21} **(original)**	ϕ_{21} **(perturbed)**
1	$-18°$	$-31°$
2	$-54°$	$-54°$
3	$-90°$	$-90°$
4	$-126°$	$-126°$
5	$-162°$	$-147°$
6	$-198°$	$-216°$
7	$-234°$	$-234°$
8	$-270°$	$-270°$
9	$-306°$	$-306°$
10	$-342°$	$-330°$

Table A.1: Unit cell transmission phases (ϕ_{21}) used in the design of the gradient metasurface for plane wave refraction. The original phase gradient corresponds to the linear phase gradient. The perturbed phase gradient corresponds to the adjusted phases used to improve the performance of the metasurface.

of the impedance sheet's to change sign only once at $\phi_{21} = -180°$.

The metasurface is redesigned with the modified transmission phases and the required sheet impedances are shown in Fig. A.6 (b). Ten unit cells of the metasurface are again simulated in COMSOL using periodic boundary conditions, and the results are shown in Fig. A.6 (d). We see that the redesigned metasurface performs significantly better than the analytical design. This indicates that avoiding transmission phases which require a large quality factor or exist near non-smooth or asymptotic regions of $Q(\phi_{21})$ can improve the performance of gradient metasurfaces designed using the local periodicity assumption.

Violations of local periodicity (like those discussed above) can present challenges when realizing inhomogeneous metasurfaces where local periodicity has been assumed. Issues arising from these violations have been handled implicitly in the literature in a variety of ways. Such as in [64], where the phase gradient was altered to improve the metasurface's performance by reducing transmission losses. On the other hand, [40,60,61] made the sheet spacers extremely thin $d < \lambda/40$. This generally increases the quality factor of the unit cells but, it has the benefit of shifting the transmission phases where all three impedance sheets transition from capactive to inductive to occur at the same point. This means that shrinking the spacings makes it easier to select transmission phases that avoid regions where (A.8) is not smooth. As a result, extremely thin spacings can improve the design performance at the expense increasing manufacturing difficulties and producing higher quality factors: lower bandwidths. Alternatively, PEC [63] or PMC [94] baffles have been used to eliminate inter-cell coupling to validate the assumption of local periodicity. However, in practice the use of PEC baffles presents a manufacturing challenge and PMC baffles cannot be realized.

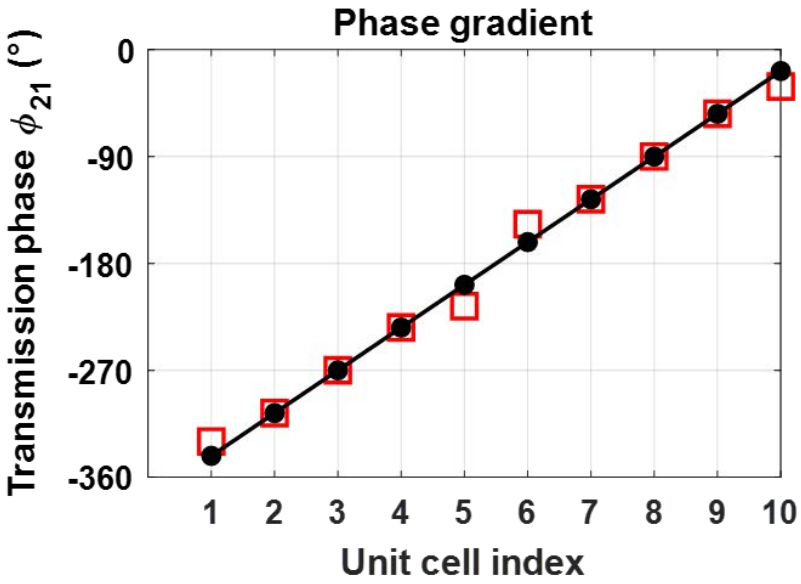

Figure A.7: Comparison of the transmission phases used for the original and perturbed phase gradients. The solid black circles indicate the transmission phases used for the linear phase gradient. The empty red squares indicate the transmission phases used for the perturbed phase gradient

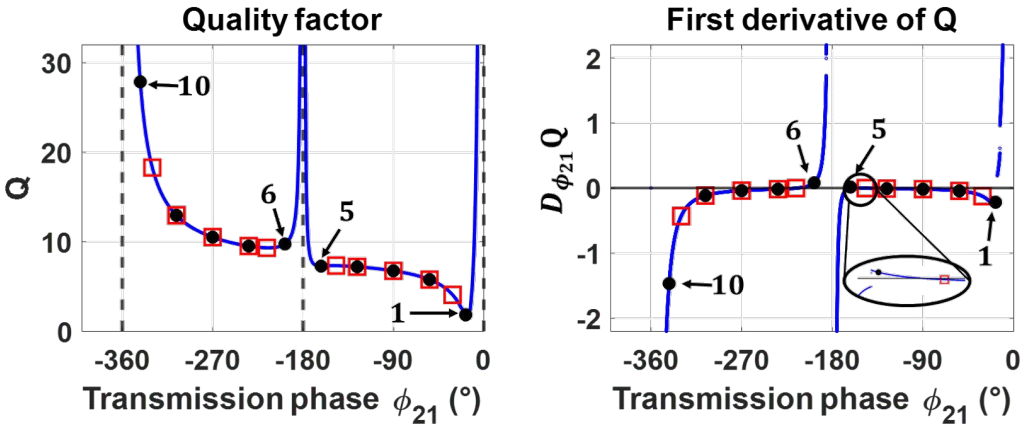

Figure A.8: (a) The quality factor of the metasurface unit cells versus transmission phase. (b) The first derivative of the quality factor with respect to transmission phase. The solid black circles indicate values corresponding to the linear phase gradient and the hollow red squares indicate the adjusted values used for the perturbed phase gradient.

These examples indicate a design trade-off between manufacturability and performance when realizing inhomogeneous metasurfaces. Using the quality factor as shown in this section provides an alternative way to improve design performance. It can be used to systematically identify problematic unit cells and adjust them where possible to allow for the trade-off between performance and manufacturability to be balanced. An alternative to this approach is to avoid the assumption of local periodicity and model interactions between unique unit cells using homogenization and integral equations as reported in, [95].

APPENDIX B

Derivation of the Mask Matrix

The matrix $\overline{\overline{G}}$ is used as a mask in the cost function,

$$g(\mathbf{p}) = \frac{1}{2}\sum_{k=1}^{K}(\mathbf{v}^k(\mathbf{p}) - \mathbf{v}^k_{\text{out}})^H \overline{\overline{G}}(\mathbf{v}^k(\mathbf{p}) - \mathbf{v}^k_{\text{out}}), \tag{B.1}$$

to select the nodal voltages that are relevant to the design goals. It is necessary because the vector $\mathbf{v}^k(\mathbf{p})$ that is solved for by the the circuit network solver,

$$\overline{\overline{Q}}_k(\mathbf{p})\mathbf{v}^k(\mathbf{p}) = \mathbf{s}, \tag{B.2}$$

returns the value of all $2MN + M + N$ nodal voltage in the network, indicated by the red circles in Fig. B.1. However, the majority of these voltages are not pertinent to design goals. Therefore to form a cost function over the pertinent voltages a transformation is required to project into the subspace of nodal voltages that are relevant,

$$\widetilde{\mathbf{v}}^k(\mathbf{p}) = \overline{\overline{T}}\mathbf{v}^k(\mathbf{p}) \tag{B.3}$$

For the designs considered in this thesis the relevant voltages were located on the periphery of the network shown as the blue lines in Fig. B.1. Therefore, the necessary transformation is from a $2MN + M + N$ dimensional space to a $2(M + N)$ dimensional subspace that can be represented by a $2(M + N) \times (2MN + M + N)$ matrix. For clarity, consider an example with $M = 3$ and $N = 1$ then the matrix is 8×10 and would have the following

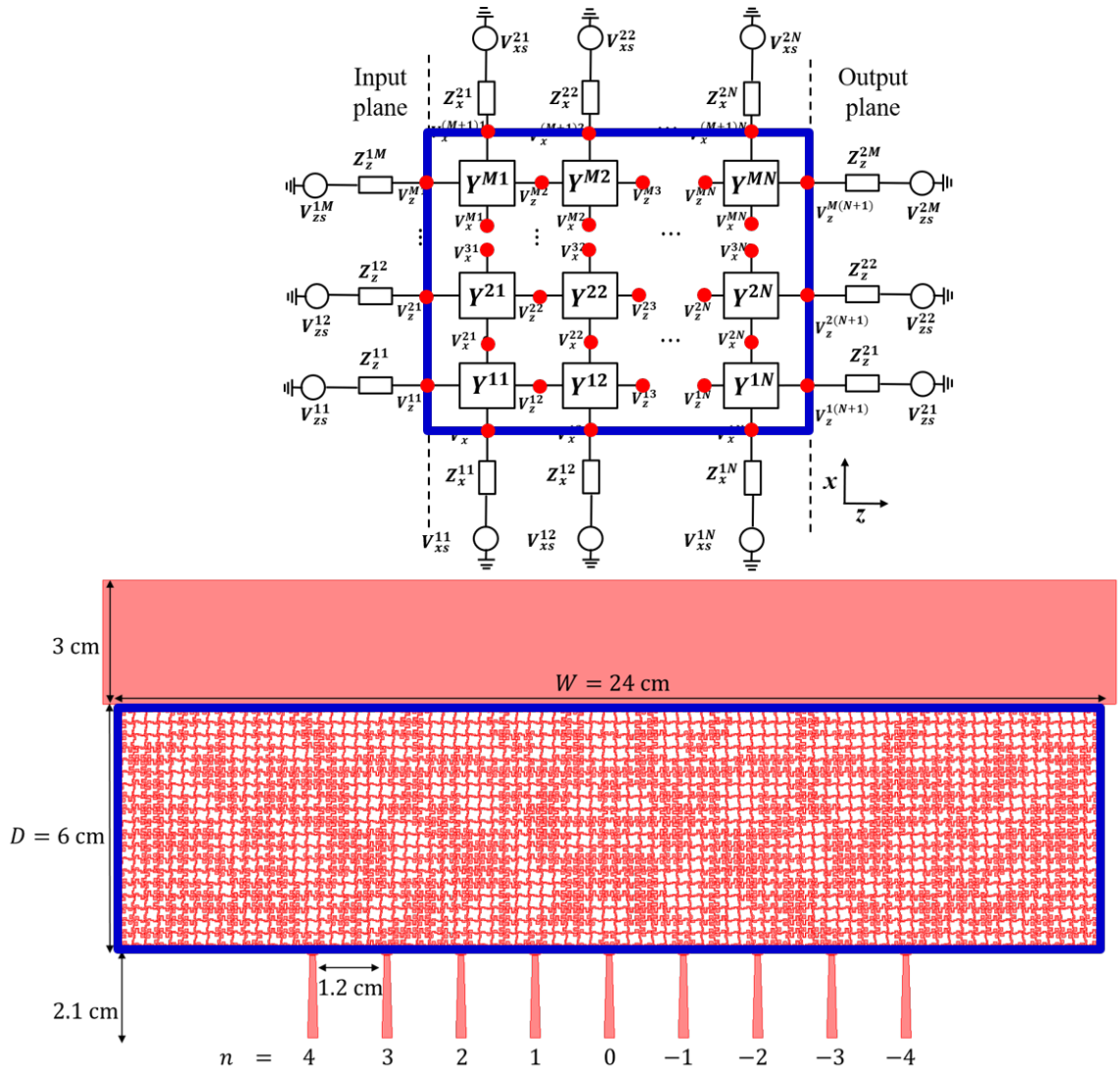

Figure B.1: Top: Schematic drawing of the voltages solved for by the circuit network solver (red circles) and the voltages selected by the $\overline{\overline{G}}$ matrix (blue line). Bottom: Blue line indicates location of the voltages on the metastructured beamformer example.

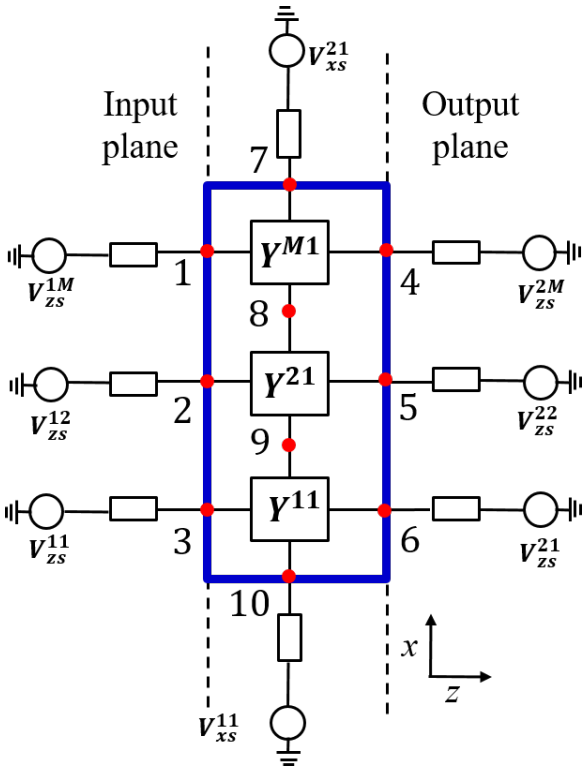

Figure B.2: Schematic of the circuit network used in the example in the appendix. The numbered red circles represent node voltages that are solved for by the circuit network solver and the blue line intersects the selected voltages.

form,

$$\overline{\overline{T}} = \begin{pmatrix} a & 0 & 0 & 0 & 0 & 0 & 0 & 0 & 0 & 0 \\ 0 & b & 0 & 0 & 0 & 0 & 0 & 0 & 0 & 0 \\ 0 & 0 & c & 0 & 0 & 0 & 0 & 0 & 0 & 0 \\ 0 & 0 & 0 & d & 0 & 0 & 0 & 0 & 0 & 0 \\ 0 & 0 & 0 & 0 & e & 0 & 0 & 0 & 0 & 0 \\ 0 & 0 & 0 & 0 & 0 & f & 0 & 0 & 0 & 0 \\ 0 & 0 & 0 & 0 & 0 & 0 & g & 0 & 0 & 0 \\ 0 & 0 & 0 & 0 & 0 & 0 & 0 & 0 & 0 & h \end{pmatrix} \tag{B.4}$$

where rows correspond to the number of the node number as shown in Fig. B.2, and the letters $a - f$ represent non-negative numbers whose value depends on the importance of each nodal voltage.

The cost function can then be formed over $\widetilde{\mathbf{v}}^k(\mathbf{p})$ as follows,

$$g(\mathbf{p}) = \frac{1}{2}\sum_{k=1}^{K}(\widetilde{\mathbf{v}}^k(\mathbf{p}) - \widetilde{\mathbf{v}}^k_{\text{out}})^H(\widetilde{\mathbf{v}}^k(\mathbf{p}) - \widetilde{\mathbf{v}}^k_{\text{out}}). \tag{B.5}$$

Then by defining,

$$\widetilde{\mathbf{v}}^k_{\text{out}} = \overline{\overline{T}}\mathbf{v}^k_{\text{out}}, \tag{B.6}$$

and substituting (B.3) and (B.6) into (B.5),

$$g(\mathbf{p}) = \frac{1}{2}\sum_{k=1}^{K}(\mathbf{v}^k(\mathbf{p}) - \mathbf{v}^k_{\text{out}})^H\overline{\overline{T}}^T\overline{\overline{T}}(\mathbf{v}^k(\mathbf{p}) - \mathbf{v}^k_{\text{out}}), \tag{B.7}$$

the original cost function (B.1) can be recovered by defining $\overline{\overline{G}} = \overline{\overline{T}}^T\overline{\overline{T}}$.

APPENDIX C

Derivation of the Adjoint Problem

This appendix provides a detailed derivation of the adjoint problem used to calculate the derivative of the cost function used in Chapter 3,

$$g(\mathbf{p}) = \sum_{k=1}^{K} g_k(\mathbf{p}) = \frac{1}{2}\sum_{k=1}^{K}(\mathbf{v}^k(\mathbf{p}) - \mathbf{v}^k_{\text{out}})^H \overline{\overline{G}}(\mathbf{v}^k(\mathbf{p}) - \mathbf{v}^k_{\text{out}}). \tag{C.1}$$

In (C.1), $\mathbf{p} = (p_1, p_2, ..., p_P)^T$ represents the P variables of the function and $\overline{\overline{G}}$ is Hermitian. The adjoint problem associated with (C.1) is formed by taking its derivative with respect to the i^{th} variable,

$$\frac{\partial g(\mathbf{p})}{\partial p_i} = \sum_{k=1}^{K} \frac{\partial g_k(\mathbf{p})}{\partial p_i} \tag{C.2}$$

and the term $\frac{\partial g_k(\mathbf{p})}{\partial p_i}$ is given by,

$$\frac{\partial g_k(\mathbf{p})}{\partial p_i} = (\frac{\partial \mathbf{v}^k(\mathbf{p})}{\partial p_i})^H \overline{\overline{G}}(\mathbf{v}^k(\mathbf{p}) - \mathbf{v}^k_{\text{out}}) + (\mathbf{v}^k(\mathbf{p}) - \mathbf{v}^k_{\text{out}})^H \overline{\overline{G}} \frac{\partial \mathbf{v}^k(\mathbf{p})}{\partial p_i} \tag{C.3}$$

$$= \big((\mathbf{v}^k(\mathbf{p}) - \mathbf{v}^k_{\text{out}})^H \overline{\overline{G}}^H \frac{\partial \mathbf{v}^k(\mathbf{p})}{\partial p_i}\big)^H + (\mathbf{v}^k(\mathbf{p}) - \mathbf{v}^k_{\text{out}})^H \overline{\overline{G}} \frac{\partial \mathbf{v}^k(\mathbf{p})}{\partial p_i}. \tag{C.4}$$

Noting that $\overline{\overline{G}}$ is Hermitian and both terms are scalars (C.4) is equal to,

$$\frac{\partial g_k(\mathbf{p})}{\partial p_i} = \big((\mathbf{v}^k(\mathbf{p}) - \mathbf{v}^k_{\text{out}})^H \overline{\overline{G}} \frac{\partial \mathbf{v}^k(\mathbf{p})}{\partial p_i}\big)^* + (\mathbf{v}^k(\mathbf{p}) - \mathbf{v}^k_{\text{out}})^H \overline{\overline{G}} \frac{\partial \mathbf{v}^k(\mathbf{p})}{\partial p_i} \tag{C.5}$$

$$\frac{\partial g_k(\mathbf{p})}{\partial p_i} = 2\Re\big\{(\mathbf{v}^k(\mathbf{p}) - \mathbf{v}^k_{\text{out}})^H \overline{\overline{G}} \frac{\partial \mathbf{v}^k(\mathbf{p})}{\partial p_i}\big\}. \tag{C.6}$$

The only term left to calculate is $\frac{\partial \mathbf{v}^k(\mathbf{p})}{\partial p_i}$ which is given by the solution to,

$$\overline{\overline{Q}}_k(\mathbf{p})\mathbf{v}^k(\mathbf{p}) = \mathbf{s}. \tag{C.7}$$

Taking the implicit derivative of the above equation and solving for $\frac{\partial \mathbf{v}^k(\mathbf{p})}{\partial p_i}$ yields,

$$\frac{\partial \mathbf{v}^k(\mathbf{p})}{\partial p_i} = -\overline{\overline{Q}}_k(\mathbf{p})^{-1} \frac{\partial \overline{\overline{Q}}_k(\mathbf{p})}{\partial p_i} \mathbf{v}^k(\mathbf{p}). \tag{C.8}$$

Then by combining (C.6) and (C.8) for all p_i, suppressing the dependence on the variables $\mathbf{p}$, the gradient can be expressed as,

$$\nabla_{\mathbf{p}}(g_k(\mathbf{p})) = (\frac{\partial g_k}{\partial p_1}, \frac{\partial g_k}{\partial p_2}, ..., \frac{\partial g_k}{\partial p_P}) = -\Re\{(\mathbf{v}^k - \mathbf{v}^k_{\text{out}})^H \overline{\overline{G}} \ \overline{\overline{Q}}_k^{-1} \overline{\overline{V}}^k_{\mathbf{p}}\} \tag{C.9}$$

where $\overline{\overline{V}}^k_{\mathbf{p}}$ is the following matrix,

$$\overline{\overline{V}}^k_{\mathbf{p}} = (\frac{\partial \overline{\overline{Q}}_k}{\partial p_1}\mathbf{v}^k | \frac{\partial \overline{\overline{Q}}_k}{\partial p_2}\mathbf{v}^k | \frac{\partial \overline{\overline{Q}}_k}{\partial p_3}\mathbf{v}^k | \dots | \frac{\partial \overline{\overline{Q}}_k}{\partial p_P}\mathbf{v}^k) \tag{C.10}$$

This matrix can be solved for analytically if differentiable expressions for the admittance matrix (Y-matrix) elements in $\overline{\overline{Q}}_k$ are available. Otherwise, it can be approximated using finite-differences. The efficiency of calculating the gradient can be improved by observing that the product on the RHS of (C.9), excluding $\overline{\overline{V}}^k_{\mathbf{p}}$, forms a vector, $\boldsymbol{\lambda}_k^H$, that can be solved for independently,

$$\boldsymbol{\lambda}_k^H = (\mathbf{v}^k - \mathbf{v}^k_{\text{out}})^H \overline{\overline{G}} \ \overline{\overline{Q}}_k^{-1} \tag{C.11}$$

Right multiplying both sides by $\overline{\overline{Q}}_k$ and taking the Hermitian transpose yields the adjoint problem associated with the k^{th} cost function in (C.1),

$$\overline{\overline{Q}}_k^H \boldsymbol{\lambda_k} = \overline{\overline{G}}(\mathbf{v}^k - \mathbf{v}^k_{\text{out}}). \tag{C.12}$$

Using (C.12), the adjoint variable λ_k can be calculated at the same cost as solving the forward problem (C.7). Using (C.11) in (C.9) yields the following expression for the gradient of the k^{th} cost function,

$$\nabla_{\mathbf{p}}(g_k(\mathbf{p})) = -\Re\{\boldsymbol{\lambda}_k^H \overline{\overline{V}}^k_{\mathbf{p}}\} \tag{C.13}$$

The expression (C.9) provides a means of obtaining the gradient of the k^{th} cost function at the computational expense of effectively two forward problem solutions. To form the full gradient of (C.1) the gradient for each input-output pair, (C.13), is summed over k,

$$\nabla_{\mathbf{p}}(g(\mathbf{p})) = -\sum_{k=1}^{K} \Re\{\boldsymbol{\lambda}_k^H \overline{\overline{V}}^k_{\mathbf{p}}\}. \tag{C.14}$$

APPENDIX D

Additional Simulation and Measurement Results for the Metastructured Beamformer

In this appendix additional plots for the performance of the positive and negative refraction beamformers are provided. Plots of the normalized radiation patterns for each of the excitations are shown for the beamformer exhibiting positive refractive behavior in Fig. D.1a-D.1i and for the beamformer exhibiting negative refractive behavior in Fig. D.2a-D.2i. These plots demonstrate that each of the beams are well formed with good agreement in the main beam and first sidelobe for each beam.

Additionally, plots of the realized gain are shown for the beamformer exhibiting positive refractive behavior in Fig. D.3a and for the beamformer exhibiting negative refractive behavior in Fig. D.3b. The plots in Fig. D.3a show that the beams are well formed but there is roughly 2.7 dB of loss in each of the beams when compared to the simulated results for the positive refraction beamformer. The plots in Fig. D.3b show that the beams are well formed but the gain is down by about 3.3 dB in each beam compared to the simulated results for the negative refraction beamformer. However, the loss is difficult to determine due to the fact that the measured and simulated directivities do not agree as well as they did for the positive refraction case.

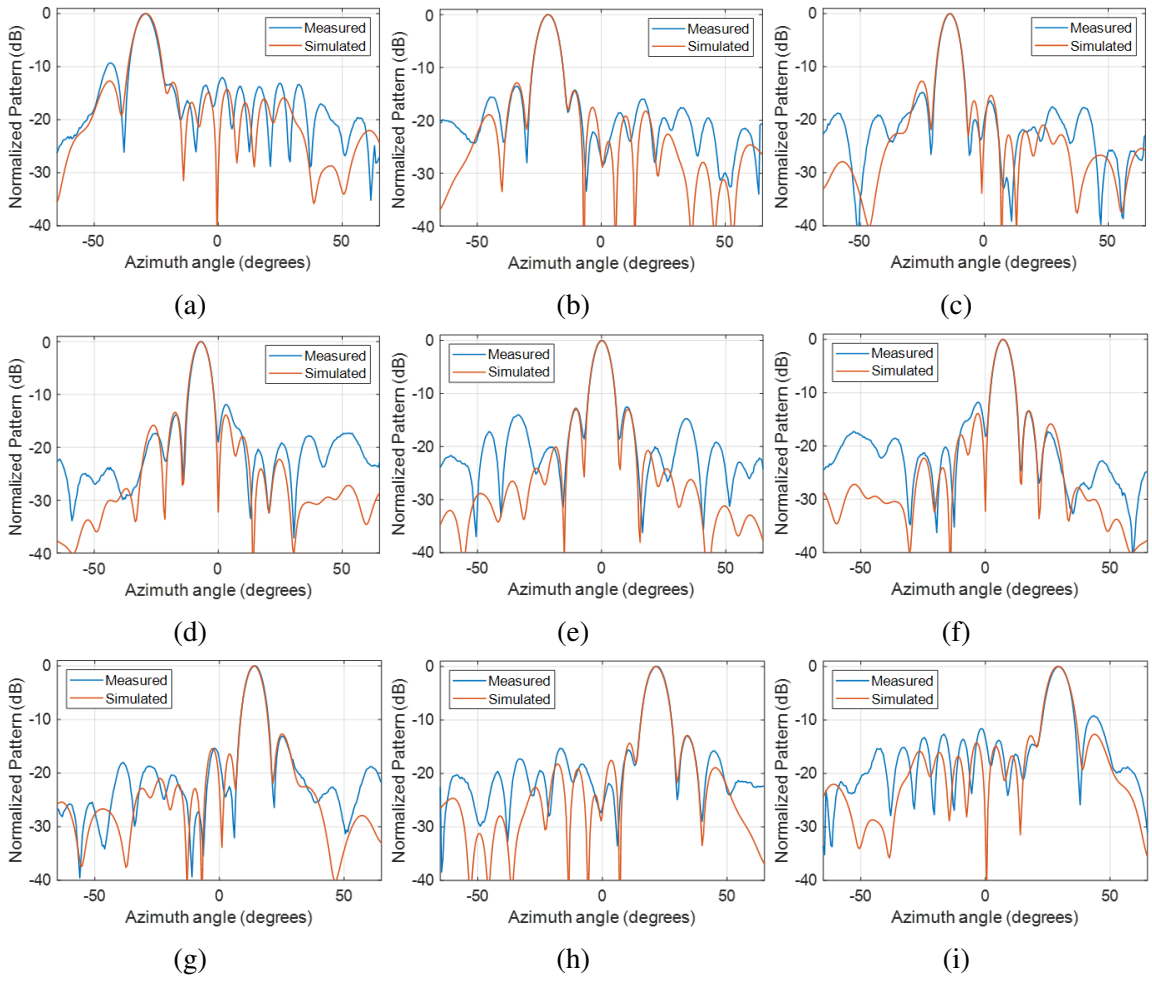

Figure D.1: A comparison of the measured and simulated normalized co-polarized H-plane radiation pattern for the positive refraction beamformer: (a) n = -4 (b) = -3 (c) n = -2 (d) n = -1 (e) n = 0 (f) n = 1 (g) = 2 (h) n = 3 (i) n = 4.

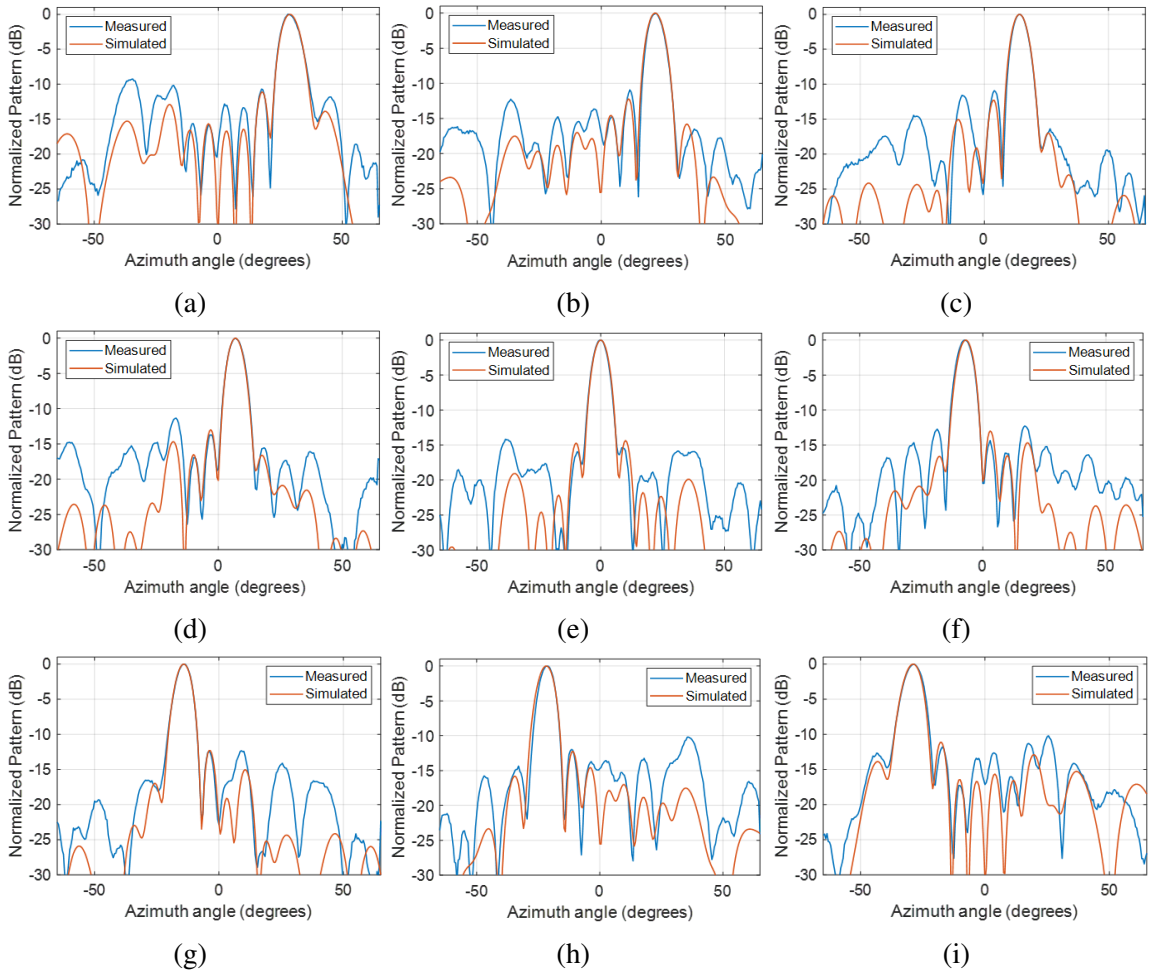

Figure D.2: A comparison of the measured and simulated normalized co-polarized H-plane radiation pattern for the negative refraction beamformer: (a) n = -4 (b) = -3 (c) n = -2 (d) n = -1 (e) n = 0 (f) n = 1 (g) = 2 (h) n = 3 (i) n = 4.

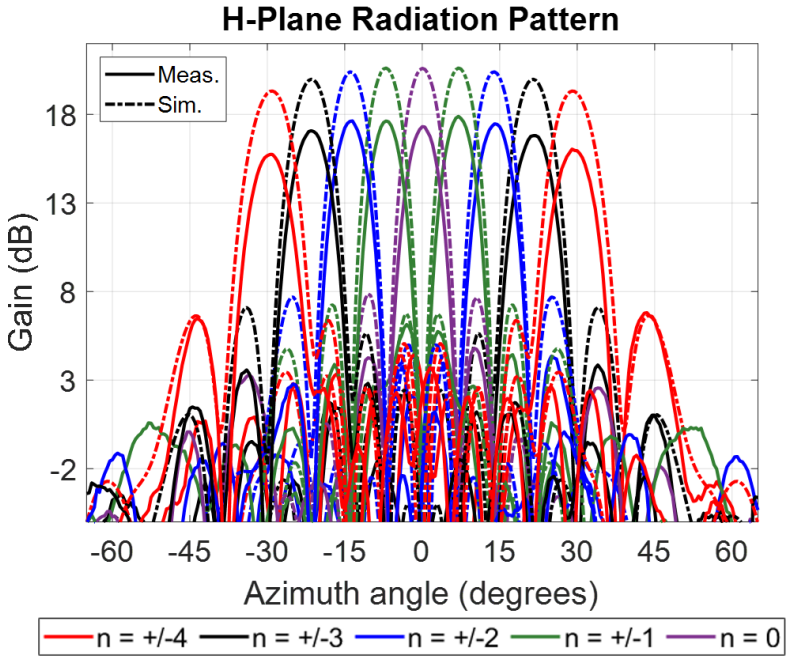

(a)

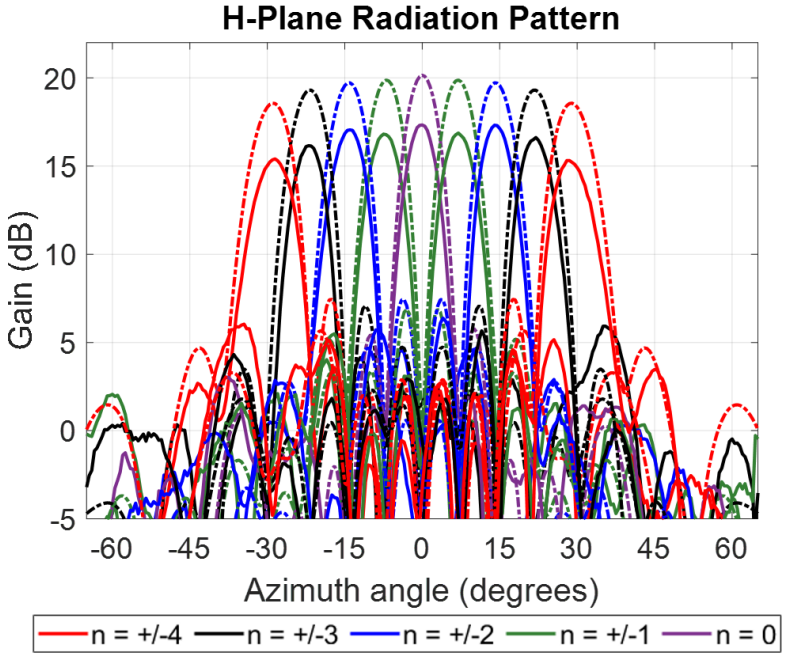

(b)

Figure D.3: (a) Plot of the simulated and measured realized gain for the positive refraction beamformer. (b) Plot of the simulated and measured gain for the negative refraction beamformer.

BIBLIOGRAPHY

[1] J. B. Pendry, "Negative refraction makes a perfect lens," *Phys. Rev. Lett.*, vol. 85, pp. 3966–3969, Oct 2000. [Online]. Available: https://link.aps.org/doi/10.1103/PhysRevLett.85.3966

[2] A. Grbic and G. V. Eleftheriades, "Experimental verification of backward-wave radiation from a negative refractive index metamaterial," *J. Appl. Phys.*, vol. 92, no. 10, pp. 5930–5935, 2002. [Online]. Available: https://doi.org/10.1063/1.1513194

[3] A. Grbic, L. Jiang, and R. Merlin, "Near-field plates: Subdiffraction focusing with patterned surfaces," *Science*, vol. 320, no. 5875, pp. 511–513, 2008. [Online]. Available: https://www.science.org/doi/abs/10.1126/science.1154753

[4] J. Hunt, T. Driscoll, A. Mrozack, G. Lipworth, M. Reynolds, D. Brady, and D. R. Smith, "Metamaterial apertures for computational imaging," *Science*, vol. 339, no. 6117, pp. 310–313, 2013. [Online]. Available: https://science.sciencemag.org/content/339/6117/310

[5] A. Grbic and G. V. Eleftheriades, "Overcoming the diffraction limit with a planar left-handed transmission-line lens," *Phys. Rev. Lett.*, vol. 92, p. 117403, Mar 2004. [Online]. Available: https://link.aps.org/doi/10.1103/PhysRevLett.92.117403

[6] A. Epstein and G. V. Eleftheriades, "Arbitrary power-conserving field transformations with passive lossless omega-type bianisotropic metasurfaces," *IEEE Trans. Antennas Propag.*, vol. 64, no. 9, pp. 3880–3895, 2016.

[7] J. P. S. Wong, A. Epstein, and G. V. Eleftheriades, "Reflectionless wide-angle refracting metasurfaces," *IEEE Antennas Wireless Propag. Lett.*, vol. 15, pp. 1293–1296, 2016.

[8] S. Tretyakov, *Analytical modeling in applied electromagnetics*. Artech House, 2003.

[9] J. B. Pendry, D. Schurig, and D. R. Smith, "Controlling electromagnetic fields," *Science*, vol. 312, no. 5781, pp. 1780–1782, 2006.

[10] U. Leonhardt, "Optical conformal mapping," *Science*, vol. 312, no. 5781, pp. 1777–1780, 2006.

[11] B. B. Tierney, N. I. Limberopoulos, R. L. Ewing, and A. Grbic, "A planar, broadband, metamaterial-based, transmission-line beamformer," *IEEE Trans. Antennas Propag.*, vol. 66, no. 9, pp. 4844–4853, 2018.

[12] J. Budhu and Y. Rahmat-Samii, "A novel and systematic approach to inhomogeneous dielectric lens design based on curved ray geometrical optics and particle swarm optimization," *IEEE Transactions on Antennas and Propagation*, vol. 67, no. 6, pp. 3657–3669, 2019.

[13] M. Mansouree, H. Kwon, E. Arbabi, A. McClung, A. Faraon, and A. Arbabi, "Multifunctional 2.5 d metastructures enabled by adjoint optimization," *Optica*, vol. 7, no. 1, pp. 77–84, 2020.

[14] C. M. Lalau-Keraly, S. Bhargava, O. D. Miller, and E. Yablonovitch, "Adjoint shape optimization applied to electromagnetic design," *Opt. Express*, vol. 21, no. 18, pp. 21 693–21 701, Sep 2013. [Online]. Available: http://www.opticsexpress.org/abstract.cfm?URI=oe-21-18-21693

[15] N. Mohammadi Estakhri, B. Edwards, and N. Engheta, "Inverse-designed metastructures that solve equations," *Science*, vol. 363, no. 6433, pp. 1333–1338, 2019. [Online]. Available: https://science.sciencemag.org/content/363/6433/1333

[16] J. R. Sanford, "Design of a miniature reactive beam forming network," in *2019 IEEE Antennas and Propag. Soc. Int. Symp. (APSURSI)*, 2019, pp. 1357–1358.

[17] M. Chen, J. Jiang, and J. A. Fan, "Design space reparameterization enforces hard geometric constraints in inverse-designed nanophotonic devices," *ACS Photonics*, vol. 7, no. 11, pp. 3141–3151, 2020. [Online]. Available: https://doi.org/10.1021/acsphotonics.0c01202

[18] S. D. Campbell, D. Sell, R. P. Jenkins, E. B. Whiting, J. A. Fan, and D. H. Werner, "Review of numerical optimization techniques for meta-device design," *Opt. Mater. Express*, vol. 9, no. 4, pp. 1842–1863, Apr 2019. [Online]. Available: http://www.osapublishing.org/ome/abstract.cfm?URI=ome-9-4-1842

[19] G. V. Eleftheriades and K. G. Balmain, *Negative Refraction Metamaterials: Fundamental Principles and Applications*, 1st ed. John Wiley & Sons, Inc., 2005.

[20] O. F. Siddiqui, "The forward transmission matrix (ftm) method for s-parameter analysis of microwave circuits and their metamaterial counterparts," *Prog. Electromagn. Res. B*, vol. 66, pp. 123–141, 2016.

[21] G. Gok and A. Grbic, "Tensor transmission-line metamaterials," *IEEE Trans. Antennas Propag.*, vol. 58, no. 5, pp. 1559–1566, 2010.

[22] M. Zedler and G. V. Eleftheriades, "Anisotropic transmission-line metamaterials for 2-d transformation optics applications," *Proc. IEEE*, vol. 99, no. 10, pp. 1634–1645, 2011.

[23] J. Vehmas, S. Hrabar, and S. Tretyakov, "Omega transmission lines with applications to effective medium models of metamaterials," *J. Appl. Phys.*, vol. 115, no. 13, p. 134905, 2014. [Online]. Available: https://doi.org/10.1063/1.4869655

[24] A. Serdyukov, I. Semchenko, S. Tretyakov, and A. Sihvola, *Electromagnetics of Bi-anisotropic Materials Theory and Applications*, 1st ed. Gordon and Breach Science Publishers, 2001.

[25] A. Alù, "First-principles homogenization theory for periodic metamaterials," *Phys. Rev. B*, vol. 84, p. 075153, Aug 2011. [Online]. Available: https://link.aps.org/doi/10.1103/PhysRevB.84.075153

[26] R. Marqués, F. Medina, and R. Rafii-El-Idrissi, "Role of bianisotropy in negative permeability and left-handed metamaterials," *Phys. Rev. B*, vol. 65, p. 144440, Apr 2002. [Online]. Available: https://link.aps.org/doi/10.1103/PhysRevB.65.144440

[27] A. Shaltout, V. Shalaev, and A. Kildishev, "Homogenization of bi-anisotropic metasurfaces," *Opt. Express*, vol. 21, no. 19, pp. 21 941–21 950, Sep 2013. [Online]. Available: http://www.osapublishing.org/oe/abstract.cfm?URI=oe-21-19-21941

[28] D. M. Pozar, *Microwave Engineering*, 4th ed. John Wiley & Sons, Inc., 2011.

[29] G. A. Campbell, "Xxx. on loaded lines in telephonic transmission," *London, Edinburgh, Dublin Philos. Mag. J. Sci.*, vol. 5, no. 27, pp. 313–330, 1903.

[30] P. Johns and R. Beurle, "Numerical solution of 2-dimensional scattering problems using a transmission-line matrix," *Proc. Inst. Electr. Eng*, vol. 118, pp. 1203–1208(5), September 1971. [Online]. Available: https://digital-library.theiet.org/content/journals/10.1049/piee.1971.0217

[31] C. Caloz and T. Itoh, "Application of the transmission line theory of left-handed (lh) materials to the realization of a microstrip "lh line"," in *2002 IEEE Antennas and Propag. Soc. Int. Symp. (APSURSI)*, vol. 2, 2002, pp. 412–415 vol.2.

[32] A. Grbic and G. Eleftheriades, "A backward-wave antenna based on negative refractive index l-c networks," in *2002 IEEE Antennas and Propag. Soc. Int. Symp. (APSURSI)*, vol. 4, 2002, pp. 340–343 vol.4.

[33] V. Veselago, "The electrodynamics of substances with simultaneously negative values of epsilon and mu," *Sov Phys Uspekhi*, vol. 10, pp. 509–514, January 1968.

[34] G. Eleftheriades, A. Iyer, and P. Kremer, "Planar negative refractive index media using periodically l-c loaded transmission lines," *IEEE Trans. Microw. Theory Tech.*, vol. 50, no. 12, pp. 2702–2712, 2002.

[35] A. Grbic and G. Eleftheriades, "Periodic analysis of a 2-d negative refractive index transmission line structure," *IEEE Trans. Antennas Propag.*, vol. 51, no. 10, pp. 2604–2611, 2003.

[36] K. Balmain, A. Luttgen, and P. Kremer, "Power flow for resonance cone phenomena in planar anisotropic metamaterials," *IEEE Trans. Antennas Propag.*, vol. 51, no. 10, pp. 2612–2618, 2003.

[37] D.-H. Kwon and C. D. Emiroglu, "Non-orthogonal grids in two-dimensional transmission-line metamaterials," *IEEE Trans. Antennas Propag.*, vol. 60, no. 9, pp. 4210–4218, 2012.

[38] D.-H. Kwon and D. H. Werner, "Polarization splitter and polarization rotator designs based on transformation optics," *Opt. Express*, vol. 16, no. 23, pp. 18 731–18 738, Nov 2008. [Online]. Available: http://www.opticsexpress.org/abstract.cfm?URI=oe-16-23-18731

[39] C. Pfeiffer and A. Grbic, "Bianisotropic metasurfaces for optimal polarization control: Analysis and synthesis," *Phys. Rev. Applied*, vol. 2, p. 044011, Oct 2014. [Online]. Available: https://link.aps.org/doi/10.1103/PhysRevApplied.2.044011

[40] J. P. S. Wong, A. Epstein, and G. V. Eleftheriades, "Reflectionless wide-angle refracting metasurfaces," *IEEE Antennas Wireless Propag. Lett.*, vol. 15, pp. 1293–1296, 2016.

[41] C. Pfeiffer and A. Grbic, "Metamaterial huygens' surfaces: Tailoring wave fronts with reflectionless sheets," *Phys. Rev. Lett.*, vol. 110, p. 197401, May 2013. [Online]. Available: https://link.aps.org/doi/10.1103/PhysRevLett.110.197401

[42] P. R. West, J. L. Stewart, A. V. Kildishev, V. M. Shalaev, V. V. Shkunov, F. Strohkendl, Y. A. Zakharenkov, R. K. Dodds, and R. Byren, "All-dielectric subwavelength metasurface focusing lens," *Opt. Express*, vol. 22, no. 21, pp. 26 212–26 221, Oct 2014. [Online]. Available: http://www.opticsexpress.org/abstract.cfm?URI=oe-22-21-26212

[43] M. Khorasaninejad, W. T. Chen, R. C. Devlin, J. Oh, A. Y. Zhu, and F. Capasso, "Metalenses at visible wavelengths: Diffraction-limited focusing and subwavelength resolution imaging," *Science*, vol. 352, no. 6290, pp. 1190–1194, 2016. [Online]. Available: https://science.sciencemag.org/content/352/6290/1190

[44] Y. Zhou, I. I. Kravchenko, H. Wang, J. R. Nolen, G. Gu, and J. Valentine, "Multilayer noninteracting dielectric metasurfaces for multiwavelength metaoptics," *Nano Letters*, vol. 18, no. 12, pp. 7529–7537, 2018, pMID: 30394751. [Online]. Available: https://doi.org/10.1021/acs.nanolett.8b03017

[45] D. González-Ovejero, G. Minatti, G. Chattopadhyay, and S. Maci, "Multibeam by metasurface antennas," *IEEE Trans. Antennas Propag.*, vol. 65, no. 6, pp. 2923–2930, 2017.

[46] O. e. Quevedo-Teruel, "Roadmap on metasurfaces," *J. Opt.*, vol. 21, no. 7, p. 073002, 2019. [Online]. Available: https://doi.org/10.1088/2040-8986/ab161d

[47] O. Quevedo-Teruel, H. Chen, A. Díaz-Rubio, G. Gok, A. Grbic, G. Minatti, E. Martini, S. Maci, G. V. Eleftheriades, M. Chen, N. I. Zheludev, N. Papasimakis, S. Choudhury, Z. A. Kudyshev, S. Saha, H. Reddy, A. Boltasseva, V. M. Shalaev, A. V. Kildishev, D. Sievenpiper, C. Caloz, A. Alù, Q. He, L. Zhou, G. Valerio, E. Rajo-Iglesias, Z. Sipus, F. Mesa, R. Rodríguez-Berral, F. Medina, V. Asadchy, S. Tretyakov, and C. Craeye, "Roadmap on metasurfaces," *Journal of Optics*, vol. 21, no. 7, p. 073002, jul 2019. [Online]. Available: https://doi.org/10.1088/2040-8986/ab161d

[48] A. S. Backer, "Computational inverse design for cascaded systems of metasurface optics," *Opt. Express*, vol. 27, no. 21, pp. 30 308–30 331, Oct 2019. [Online]. Available: http://www.opticsexpress.org/abstract.cfm?URI=oe-27-21-30308

[49] Z. Wu, Y. Ra'di, and A. Grbic, "Tunable metasurfaces: A polarization rotator design," *Phys. Rev. X*, vol. 9, p. 011036, Feb 2019. [Online]. Available: https://link.aps.org/doi/10.1103/PhysRevX.9.011036

[50] M. Boyarsky, T. Sleasman, M. F. Imani, J. N. Gollub, and D. R. Smith, "Electronically steered metasurface antenna," *Scientific Reports*, vol. 11, no. 1, p. 4693, Feb 2021. [Online]. Available: https://doi.org/10.1038/s41598-021-83377-9

[51] T. Sleasman, M. F. Imani, J. N. Gollub, and D. R. Smith, "Dynamic metamaterial aperture for microwave imaging," *Appl. Phys. Lett.*, vol. 107, p. 204104, Nov 2015. [Online]. Available: https://doi.org/10.1063/1.4935941

[52] B. B. Tierney and A. Grbic, "Designing anisotropic, inhomogeneous metamaterial devices through optimization," *IEEE Trans. Antennas Propag.*, vol. 67, no. 2, pp. 998–1009, 2019.

[53] L. Szymanski, G. Gok, and A. Grbic, "Inverse design of multi-input multi-output 2d metastructured devices," *IEEE Trans. Antennas Propag.*, pp. 1–1, 2021.

[54] R. Pestourie, C. Pérez-Arancibia, Z. Lin, W. Shin, F. Capasso, and S. G. Johnson, "Inverse design of large-area metasurfaces," *Opt. Express*, vol. 26, no. 26, pp. 33 732–33 747, Dec 2018. [Online]. Available: http://www.opticsexpress.org/abstract.cfm?URI=oe-26-26-33732

[55] A. Y. Piggott, J. Lu, K. G. Lagoudakis, J. Petykiewicz, T. M. Babinec, and J. Vučković, "Inverse design and demonstration of a compact and broadband on-chip wavelength demultiplexer," *Nature Photonics*, vol. 9, no. 6, pp. 374–377, Jun 2015. [Online]. Available: https://doi.org/10.1038/nphoton.2015.69

[56] M. Jensen and J. Wallace, "A review of antennas and propagation for mimo wireless communications," *IEEE Trans. Antennas Propag.*, vol. 52, no. 11, pp. 2810–2824, 2004.

[57] C. A. Balanis, *Antenna Theory: Analsysis and Design*, 3rd ed. John Wiley & Sons, Inc., 2005.

[58] V. S. Asadchy, M. Albooyeh, S. N. Tcvetkova, A. Díaz-Rubio, Y. Ra'di, and S. A. Tretyakov, "Perfect control of reflection and refraction using spatially dispersive metasurfaces," *Phys. Rev. B*, vol. 94, p. 075142, Aug 2016. [Online]. Available: https://link.aps.org/doi/10.1103/PhysRevB.94.075142

[59] A. H. Dorrah, M. Chen, and G. V. Eleftheriades, "Bianisotropic huygens' metasurface for wideband impedance matching between two dielectric media," *IEEE Trans. Antennas Propag.*, vol. 66, no. 9, pp. 4729–4742, 2018.

[60] B. O. Raeker and A. Grbic, "Compound metaoptics for amplitude and phase control of wave fronts," *Phys. Rev. Lett.*, vol. 122, p. 113901, Mar 2019. [Online]. Available: https://link.aps.org/doi/10.1103/PhysRevLett.122.113901

[61] A. H. Dorrah and G. V. Eleftheriades, "Bianisotropic huygens' metasurface pairs for nonlocal power-conserving wave transformations," *IEEE Antennas Wireless Propag. Lett.*, vol. 17, no. 10, pp. 1788–1792, 2018.

[62] S. N. Tcvetkova, D.-H. Kwon, A. Díaz-Rubio, and S. A. Tretyakov, "Near-perfect conversion of a propagating plane wave into a surface wave using metasurfaces," *Phys. Rev. B*, vol. 97, p. 115447, Mar 2018. [Online]. Available: https://link.aps.org/doi/10.1103/PhysRevB.97.115447

[63] V. Popov, A. Díaz-Rubio, V. Asadchy, S. Tcvetkova, F. Boust, S. Tretyakov, and S. N. Burokur, "Omega-bianisotropic metasurface for converting a propagating wave into a surface wave," *Phys. Rev. B*, vol. 100, p. 125103, Sep 2019. [Online]. Available: https://link.aps.org/doi/10.1103/PhysRevB.100.125103

[64] M. Chen, E. Abdo-Sánchez, A. Epstein, and G. V. Eleftheriades, "Theory, design, and experimental verification of a reflectionless bianisotropic huygens' metasurface for wide-angle refraction," *Phys. Rev. B*, vol. 97, p. 125433, Mar 2018. [Online]. Available: https://link.aps.org/doi/10.1103/PhysRevB.97.125433

[65] M. Albooyeh, D.-H. Kwon, F. Capolino, and S. A. Tretyakov, "Equivalent realizations of reciprocal metasurfaces: Role of tangential and normal polarization," *Phys. Rev. B*, vol. 95, p. 115435, Mar 2017. [Online]. Available: https://link.aps.org/doi/10.1103/PhysRevB.95.115435

[66] G. Gok and A. Grbic, "Tailoring the phase and power flow of electromagnetic fields," *Phys. Rev. Lett.*, vol. 111, p. 233904, Dec 2013. [Online]. Available: https://link.aps.org/doi/10.1103/PhysRevLett.111.233904

[67] D. R. Smith, W. J. Padilla, D. C. Vier, S. C. Nemat-Nasser, and S. Schultz, "Composite medium with simultaneously negative permeability and permittivity," *Phys. Rev. Lett.*, vol. 84, pp. 4184–4187, May 2000. [Online]. Available: https://link.aps.org/doi/10.1103/PhysRevLett.84.4184

[68] X. Lin, Y. Rivenson, N. T. Yardimci, M. Veli, Y. Luo, M. Jarrahi, and A. Ozcan, "All-optical machine learning using diffractive deep neural networks," *Science*, vol. 361, no. 6406, pp. 1004–1008, 2018.

[69] F. Mesa, G. Valerio, R. Rodriguez-Berral, and O. Quevedo-Teruel, "Simulation-assisted efficient computation of the dispersion diagram of periodic structures: A comprehensive overview with applications to filters, leaky-wave antennas and metasurfaces," *IEEE Antennas Propag. Mag.*, pp. 0–0, 2020.

[70] F. Alsolamy and A. Grbic, "Modal network formulation for the analysis and design of mode-converting metasurfaces in cylindrical waveguides," *IEEE Trans. Antennas Propag.*, vol. 69, no. 8, pp. 4598–4611, 2021.

[71] S. G. Johnson, "Notes on adjoint methods for 18.335," https://math.mit.edu/~stevenj/18.336/adjoint.pdf, 2006, [Online; accessed Dec. 16, 2020].

[72] W. Rotman and R. Turner, "Wide-angle microwave lens for line source applications," *IEEE Trans. Antennas Propag.*, vol. 11, no. 6, pp. 623–632, 1963.

[73] R. Luneburg, *The Mathematical Theory of Optics*, 1st ed. Brown University Press, 1944.

[74] G. Gok and A. Grbic, "A printed antenna beam former implemented using tensor transmission-line metamaterials," in *2014 IEEE Antennas and Propag. Soc. Int. Symp. (APSURSI)*, 2014, pp. 765–766.

[75] J. Butler, "Beam-forming matrix simplifies design of electronically scanned antennas," *Electronic Design*, vol. 9, pp. 170–173, 1961.

[76] Hansen, "Linear connected arrays [coupled dipole arrays]," *IEEE Antennas Wireless Propag. Lett.*, vol. 3, pp. 154–156, 2004.

[77] S. Stein, "On cross coupling in multiple-beam antennas," *IRE Trans. Antennas Propag.*, vol. 10, no. 5, pp. 548–557, 1962.

[78] R. Pestourie, Y. Mroueh, T. V. Nguyen, P. Das, and S. G. Johnson, "Active learning of deep surrogates for pdes: application to metasurface design," *npj Comp. Mat.*, vol. 6, no. 1, p. 164, Oct 2020. [Online]. Available: https://doi.org/10.1038/s41524-020-00431-2

[79] C. L. Holloway, E. F. Kuester, and A. Dienstfrey, "Characterizing metasurfaces/metafilms: The connection between surface susceptibilities and effective material properties," *IEEE Antennas Wireless Propag. Lett.*, vol. 10, pp. 1507–1511, 2011.

[80] M. Harker and P. O'Leary, "Discrete orthogonal polynomial toolbox: Dopbox version 1.8," https://www.mathworks.com/matlabcentral/fileexchange/41250-discrete-orthogonal-polynomial-toolbox-dopbox-version-1-8), MATLAB Central File Exchange, 2020, [Online; Retrieved December 21, 2020].

[81] C. Pfeiffer and A. Grbic, "A printed, broadband luneburg lens antenna," *IEEE Trans. Antennas Propag.*, vol. 58, no. 9, pp. 3055–3059, 2010.

[82] J. D. Kraus, *Antennas*, 2nd ed. McGraw-Hill Book, Co., 1988.

[83] C.-T. Tai and C. Pereira, "An approximate formula for calculating the directivity of an antenna," *IEEE Trans. Antennas Propag.*, vol. 24, no. 2, pp. 235–236, 1976.

[84] D. R. Jackson, C. Caloz, and T. Itoh, "Leaky-wave antennas," *Proc IEEE Inst*, vol. 100, no. 7, pp. 2194–2206, 2012.

[85] S. M. Rudolph and A. Grbic, "A broadband three-dimensionally isotropic negative-refractive-index medium," *IEEE Trans. Antennas Propag.*, vol. 60, no. 8, pp. 3661–3669, 2012.

[86] G. Kron, "Equivalent circuit of the field equations of maxwell-i," *Proc. IRE*, vol. 32, no. 5, pp. 289–299, 1944.

[87] S. Sun, T. S. Rappaport, R. W. Heath, A. Nix, and S. Rangan, "Mimo for millimeter-wave wireless communications: beamforming, spatial multiplexing, or both?" *IEEE Comm. Mag*, vol. 52, no. 12, pp. 110–121, 2014.

[88] J. Liang, W. Gao, H. Lees, and W. Withayachumnankul, "All-silicon terahertz planar horn antenna," *IEEE Antennas Wireless Propag. Lett.*, vol. 20, no. 11, pp. 2181–2185, 2021.

[89] H. Larocque, L. Ranzani, J. Leatham, J. Tate, A. Niechayev, T. Yengst, T. Komljenovic, C. Fodran, D. Smith, and M. Soltani, "Beam steering with ultracompact and low-power silicon resonator phase shifters," *Optics express*, vol. 27, no. 24, pp. 34 639–34 654, 2019.

[90] A. Oskooi, A. Mutapcic, S. Noda, J. D. Joannopoulos, S. P. Boyd, and S. G. Johnson, "Robust optimization of adiabatic tapers for coupling to slow-light photonic-crystal waveguides," *Opt. Express*, vol. 20, no. 19, pp. 21 558–21 575, Sep 2012. [Online]. Available: http://www.osapublishing.org/oe/abstract.cfm?URI=oe-20-19-21558

[91] J. M. Luque-González, A. Herrero-Bermello, A. Ortega-Moñux, Í. Molina-Fernández, A. V. Velasco, P. Cheben, J. H. Schmid, S. Wang, and R. Halir, "Tilted subwavelength gratings: controlling anisotropy in metamaterial nanophotonic waveguides," *Optics letters*, vol. 43, no. 19, pp. 4691–4694, 2018.

[92] L. Szymanski, B. O. Raeker, C.-W. Lin, and A. Grbic, "Fundamentals of lossless, reciprocal bianisotropic metasurface design," *Photonics*, vol. 8, no. 6, 2021. [Online]. Available: https://www.mdpi.com/2304-6732/8/6/197

[93] N. Yu, P. Genevet, M. A. Kats, F. Aieta, J.-P. Tetienne, F. Capasso, and Z. Gaburro, "Light propagation with phase discontinuities: Generalized laws of reflection and refraction," *Science*, vol. 334, no. 6054, pp. 333–337, 2011. [Online]. Available: https://www.science.org/doi/abs/10.1126/science.1210713

[94] G. Xu, G. V. Eleftheriades, and S. V. Hum, "Discrete-fourier-transform-based framework for analysis and synthesis of cylindrical Omega-bianisotropic metasurfaces," *Phys. Rev. Applied*, vol. 14, p. 064055, Dec 2020. [Online]. Available: https://link.aps.org/doi/10.1103/PhysRevApplied.14.064055

[95] J. Budhu and A. Grbic, "Perfectly reflecting metasurface reflectarrays: Mutual coupling modeling between unique elements through homogenization," *IEEE Trans. Antennas Propag.*, vol. 69, no. 1, pp. 122–134, 2021.